

THE UNIVERSITY OF CALGARY

Variability of Radio Sources in the Canadian Galactic Plane Survey

by

Stephanie Therese Wilder

A THESIS

**SUBMITTED TO THE FACULTY OF GRADUATE STUDIES
IN PARTIAL FULFILMENT OF THE REQUIREMENTS FOR THE
DEGREE OF MASTER OF SCIENCE**

DEPARTMENT OF PHYSICS AND ASTRONOMY

CALGARY, ALBERTA

November, 2000

© Stephanie Therese Wilder 2000



**National Library
of Canada**

**Acquisitions and
Bibliographic Services**

**395 Wellington Street
Ottawa ON K1A 0N4
Canada**

**Bibliothèque nationale
du Canada**

**Acquisitions et
services bibliographiques**

**395, rue Wellington
Ottawa ON K1A 0N4
Canada**

Your file Votre référence

Our file Notre référence

The author has granted a non-exclusive licence allowing the National Library of Canada to reproduce, loan, distribute or sell copies of this thesis in microform, paper or electronic formats.

The author retains ownership of the copyright in this thesis. Neither the thesis nor substantial extracts from it may be printed or otherwise reproduced without the author's permission.

L'auteur a accordé une licence non exclusive permettant à la Bibliothèque nationale du Canada de reproduire, prêter, distribuer ou vendre des copies de cette thèse sous la forme de microfiche/film, de reproduction sur papier ou sur format électronique.

L'auteur conserve la propriété du droit d'auteur qui protège cette thèse. Ni la thèse ni des extraits substantiels de celle-ci ne doivent être imprimés ou autrement reproduits sans son autorisation.

0-612-64989-X

Canada

Abstract

The Canadian Galactic Plane Survey (CGPS) is a large scale survey of a section of the Milky Way. It is more sensitive than past surveys by at least a factor of ten, thereby sampling a new population of faint radio sources in the galactic plane.

Measurements of the positions and intensities of compact sources in an 81 square degree subregion of the survey produced about 5000 sources with flux densities down to about 1mJy. A sensitive search for variability in the source was performed by combined analysis of the CGPS data in this subregion and the NRAO VLA Sky Survey. This search produced twenty-two variables, ten of which had flux density below 18mJy – a previous lower limit.

Spectral indices from the Cambridge 151MHz survey and the Westerbork WENSS 325MHz survey give an indication of the variable source's spectral nature. As well a comparison between the Palomar Sky Survey and the CGPS variables was used to search for optical counterparts.

Acknowledgements

Many thanks to my supervisor Russ Taylor for his expertise, and his guidance throughout the project. Also, thank you for believing in me and giving me the chance to try.

A very special thank you to my mother, Ute, for putting up with me over the last few years. Helping me through the hard parts, and laughing with me through the better ones. You made this thesis possible.

Thank you to Lloyd Higgs for his work on the DRAO software, both writing and editing. Also for being patient with me and my seemingly endless emails about twisted planes and least square fitting.

Thanks to my friends and fellow lab mates for making the daily return to Science B that much more enjoyable. A special thanks to Steve and Bill for their late night insights that helped the research along the way. Also thanks to Bill for showing interest in the project at the bitter end when my interest was waning.

Finally, a very special thank you to Gary, for so many things. For teaching me to program, for making me teach you E and M and for helping me keep my sanity, although more commonly, helping me lose it. Most importantly however, for just being Gary and sharing these past few years with me.

Dedication

To Joseph Kowalski (1910 - 1999)

Whose love and support spanned the generations. You are greatly missed but never forgotten.

Table of Contents

Approval Page	ii
Abstract	iii
Acknowledgements	iv
Dedication	v
Table of Contents	vi
1 Introduction	1
1.1 The Milky Way	1
1.2 The Canadian Galactic Plane Survey	2
1.3 Synchrotron Radiation	4
1.4 Bremsstrahlung Radiation	10
1.5 Extragalactic Sources	13
1.6 Galactic Sources	15
1.6.1 HII Regions	15
1.6.2 Planetary Nebulae	16
1.6.3 Stellar Winds	17
1.6.4 Symbiotic Stars	18
1.6.5 Novae	18
1.6.6 Flare Stars	19
1.6.7 Radio Emitting X-Ray Binaries	19
1.6.8 Supernova Remnants	19
1.6.9 Pulsars	21
1.7 Spectrum of galactic and extragalactic sources	22
1.8 Variability of Sources	23
1.9 Past Radio Variable Searches	25
2 Data	29
2.1 Observations	29
2.2 Basic Interferometry	31
2.2.1 The uv and lm-planes	34
2.3 Data Processing	36
2.3.1 Amplitude and Phase Calibration	36
2.3.2 Fourier Transformation and Mapping	37

2.3.3	CLEAN	38
2.3.4	Self Calibration	39
2.3.5	Short spacings and Mosaicing	40
3	Source Detection and Parameter Measurement	41
3.1	FINDSRC	41
3.1.1	Initial Parameters	44
3.2	Base-Level Fitting	49
3.3	FLUXFIT	50
3.3.1	Initial Parameters	51
3.3.2	Log file	56
3.4	Summary of previously detected fitting problems	57
3.5	GAUSSMAP	58
3.6	How GAUSSMAP image was created	59
3.6.1	Initial Parameters	59
3.7	Results of initial GAUSSMAP test	63
3.8	How Problems were fixed	67
3.8.1	Other Enhancements of FINDSRC and FLUXFIT	71
3.9	Revised FINDSRC and FLUXFIT run	73
3.10	My programs	79
3.11	The CGPS source catalogue	80
4	Variable Search and Spectral Index Measurements	84
4.1	The NVSS Survey	84
4.2	Removing Systematic Effects	85
4.3	Detection of Variability	89
4.3.1	Unmatched Sources	92
4.4	Spectral Index Determination	96
4.4.1	The Westerbork Northern Sky Survey	96
4.4.2	The Cambridge 151 MHz survey	96
4.4.3	CGPS spectral index determination	98
4.5	Polarisation	99
5	Results	101
5.1	The Variable Sources	101
5.2	Contour Plots of Variable Sources	104
5.3	Comparison to the GB Variable Survey	129
5.4	Palomar Sky Survey	129

6	Conclusions and Future Study	135
6.1	Conclusions	135
6.2	Future Study:	137

List of Tables

4.1	Comparison of CGPS and NVSS survey parameters	85
4.2	Binning of CGPS integrated flux density	86
5.1	Variable list from MVW mosaics	103
5.2	List of unmatched variable sources	105
5.3	Percentage of variability as a function of flux density	106
5.4	Comparison of CGPS variables with GB86 and GB87 catalogue . . .	130

List of Figures

1.1	Depiction of the CGPS 21cm mosaics	5
1.2	Depiction of the CGPS on a spiral galaxy	6
1.3	Synchrotron radiation emitted by a relativistic electron as it spirals around a magnetic field line.	7
1.4	Synchrotron radiation emitted in a narrow cone by an electron spi- ralling around a magnetic field line.	8
1.5	Spectrum for various values of spectral index α	13
2.1	Depiction of a two element interferometer	32
3.1	The Morlet wavelet function used by the filtering process	43
3.2	Original mosaic MV1 with sources removed, prior to Gaussians being added with GAUSSMAP	60
3.3	Depiction of unphysical situation, beam outside the range of the source	62
3.4	GAUSSMAP image with original programs	64
3.5	Work file from original GAUSSMAP test	65
3.6	Peak amplitude division vs FLUXFIT peak amplitude graph, old version	66
3.7	Graph of ratio (output major / input major) vs log of FLUXFIT amplitude, old version	68
3.8	Graph of ratio (output minor / input minor) vs log of FLUXFIT amplitude, old version	69
3.9	Residual of a near double sources when fitted automatically	72
3.10	Work file from new GAUSSMAP test	74
3.11	Peak amplitude ratio vs FLUXFIT peak amplitude graph, new version	76
3.12	Graph of ratio (output major / input major) vs log of FLUXFIT amplitude, new version	77
3.13	Graph of ratio (output minor / input minor) vs log of FLUXFIT amplitude, new version	78
3.14	Compilation of MV and MW mosaics	82
3.15	source removed MVW mosaic	83
4.1	The preliminary systematic error graph of Flux ratio vs CGPS inte- grated flux	87
4.2	Mean flux ratio vs mean flux in each bin.	88
4.3	Corrected integrated flux ratio graph vs CGPS integrated flux	90
4.4	Graph of fractional change in flux densities vs CGPS integrated flux using corrected NVSS integrated flux	91
4.5	Number of sources vs variable index graph	93

4.6	Graph of variable index vs CGPS integrated flux with $\pm 4\sigma$ lines indicated	94
4.7	Comparison of NVSS and CGPS artefacts.	97
4.8	The spectral index distribution	100
5.1	Comparison of the CGPS and NVSS contour plots for source 1	107
5.2	Comparison of the CGPS and NVSS contour plots for source 2	108
5.3	Comparison of the CGPS and NVSS contour plots for source 3	109
5.4	Comparison of the CGPS and NVSS contour plots for source 4	110
5.5	Comparison of the CGPS and NVSS contour plots for source 5	111
5.6	Comparison of the CGPS and NVSS contour plots for source 6	112
5.7	Comparison of the CGPS and NVSS contour plots for source 7	113
5.8	Comparison of the CGPS and NVSS contour plots for source 8	114
5.9	Comparison of the CGPS and NVSS contour plots for source 9	115
5.10	Comparison of the CGPS and NVSS contour plots for source 10	116
5.11	Comparison of the CGPS and NVSS contour plots for source 11	117
5.12	Comparison of the CGPS and NVSS contour plots for source 12	118
5.13	Comparison of the CGPS and NVSS contour plots for source 13	119
5.14	Comparison of the CGPS and NVSS contour plots for source 14	120
5.15	Comparison of the CGPS and NVSS contour plots for source 15	121
5.16	Comparison of the CGPS and NVSS contour plots for source 16	122
5.17	Comparison of the CGPS and NVSS contour plots for source 17	123
5.18	Comparison of the CGPS and NVSS contour plots for source 18	124
5.19	Comparison of the CGPS and NVSS contour plots for source 19	125
5.20	Comparison of the CGPS and NVSS contour plots for the unmatched source 1	126
5.21	Comparison of the CGPS and NVSS contour plots for the unmatched source 2	127
5.22	Comparison of the CGPS and NVSS contour plots for the unmatched source 3	128
5.23	Comparison of the Palomar Sky Survey and the CGPS variables	131
5.24	Comparison of the Palomar Sky Survey and the CGPS variables	132
5.25	Comparison of the Palomar Sky Survey and the CGPS variables	133
5.26	Comparison of the Palomar Sky Survey and the CGPS variables	134

Chapter 1

Introduction

The observational techniques of Radio Astronomy started as a result of Karl Jansky's work in the 1930's. Jansky was working for Bell Laboratories researching the production of radio wavelength static from thunderstorms. Through his research he discovered that some of this static originated outside the atmosphere. By 1935 he concluded that the signal was coming from the plane of the galaxy in the direction of the constellation Sagittarius – the direction of the centre of the galaxy (Carroll & Ostlie 1996). In the last 65 years radio astronomy has developed immensely. Research on exotic objects such as quasars, BL Lac objects and other Active Galactic Nuclei is now possible. A new understanding of extended emission is unfolding and the future promises a look back to before the first galaxies. Radio astronomy is a powerful tool for looking inside and outside the galaxy and for surveying the nature of the objects therein.

1.1 The Milky Way

The Milky Way is a spiral galaxy. It consists of spiral arms in a disk, a galactic bulge at the centre, and a halo which is almost completely dark matter. Historically the Milky Way was known by the band of diffuse starlight that stretched across the sky. The majority of what was seen, and is still seen today, are stars within our galaxy. What are these objects that have fascinated mankind for millennia?

Stellar objects are dominated by Hydrogen-burning main sequence stars; there are also younger stars, pre-main sequence stars, older stars, giants and super giants, and dying stars, planetary nebulae and supernovae. The death of a star results in a white dwarf, neutron star, or black hole, depending on the mass of the dying star. Of these objects, the majority are white dwarfs. Along with stars there exists planets, as well as extended objects such as HII regions, supernova remnants, and nebulae.

The interstellar medium (ISM) is also an important constituent of the galactic disk. For many years the true size of our galaxy was not known because of the extinction effects caused by dust in the ISM. Optically, light cannot penetrate the galactic disk. From the location of the sun, no bulge at the centre of the galaxy can be seen; the gas and dust within the galaxy hide it. As the wavelengths get longer however, more can be seen of our galaxy. At radio wavelengths there is no extinction from the dust so objects both inside and outside our galaxy can be seen. For this reason radio wavelengths are used to survey the population of objects in the galactic plane.

1.2 The Canadian Galactic Plane Survey

The Canadian Galactic Plane Survey (CGPS) is a survey of the radio emission from a 70° long segment of the northern Galactic Plane. It is not the first radio survey of the galactic plane; there have been others in the past, as this was one of the first uses of radio astronomy. These earlier surveys were responsible for finding the brightest objects in the radio sky, Cygnus A, Cassiopeia A and the Sagittarius complex.

The angular resolution, sensitivity and observing frequency are critical param-

eters for surveys of the galactic plane. Sensitivity is a measure of the weakest detectable source. It is a parameter of the telescope that is always maximised in a survey. Resolution is the ability of the telescope to separate close objects, or to pick out their finer details. Single-dish radio telescopes, with higher resolution, are limited to a small field of view. If a large survey is wanted, typically the resolution is reduced. An interferometer's resolution, on the other hand, is determined by the number of telescopes and the maximum spacing between them, thereby allowing large-scale surveys to be done with high resolution.

The observing frequency determines what kinds of sources can be seen. Sources in the galactic plane can be classified as either thermal (Bremsstrahlung) or non-thermal (synchrotron) radiators. Non-thermal sources have decreasing intensity with increasing frequency, therefore, the higher the frequency the weaker the source intensity. Non-thermal sources dominate the galaxy below about 1 GHz. If a survey is performed at a high frequency only the brightest non-thermal sources will be detected. Compact thermal objects, however, are the opposite; they are brighter at high frequencies. Since the CGPS was intended for observing both thermal and non-thermal objects, the frequencies of 1420 MHz and 408 MHz were chosen.

The CGPS observations were taken, by CGPS consortium members, with the interferometer at the Dominion Radio Astrophysical Observatory (DRAO) in Penticton, B.C. using 12 hour exposures for each of 12 configurations of the array. The whole project took 5 years. A map of the CGPS is given below with the four mosaics MV1, MV2, MW1, MW2 studied in this thesis shown on the extreme left (Figure 1.1). The CGPS survey is looking outwards from the position of our sun. The sun is located about 8.5 kpc from the centre of the galaxy ($1 \text{ kpc} = 3.086 \times 10^{19}$

m). Figure 1.2 below shows the region of the survey. The survey covers 70° of longitude between $l = 75$ to $l = 145^\circ$, with latitude between $b = -3.5$ to $b = 5.5^\circ$ at 1420 MHz and $b = -6.7^\circ$ to $b = 8.7^\circ$ at 408 MHz. This sky coverage is very large and the resolution is still 1 arcmin at 1420 MHz, similar to what can be resolved by the human eye.

1.3 Synchrotron Radiation

Synchrotron radiation is commonly referred to, in radio astronomy, as non-thermal radiation. Its mechanism was proposed by the Russian Astronomer J. Shklovsky in 1953. Synchrotron radiation is produced when relativistic electrons spiral along magnetic field lines in a helical pattern, according to the equation for magnetic force on a moving charge q :

$$\vec{F}_m = \frac{q}{c}(\vec{v} \times \vec{B}) \quad (1.1)$$

where c is the speed of light, \vec{v} is the velocity of the charged particle and \vec{B} is the magnetic field (in gauss). Due to the cross product the component of the electron's velocity perpendicular to the field lines produces the circular motion around the field line, while the component of velocity along the field line remains unaffected, thus producing the helical pattern. As the electron follows this curved path it accelerates and emits electromagnetic radiation. For relativistic velocities the radiation is concentrated in the direction of the electron's motion and is strongly linearly polarised, as is seen in figure 1.3 (Carroll & Ostlie 1996). The frequency of the emitted radiation depends on the strength of the magnetic field and the energy of the charged particle (Zeilik et al. 1992). This frequency can be calculated using the total energy

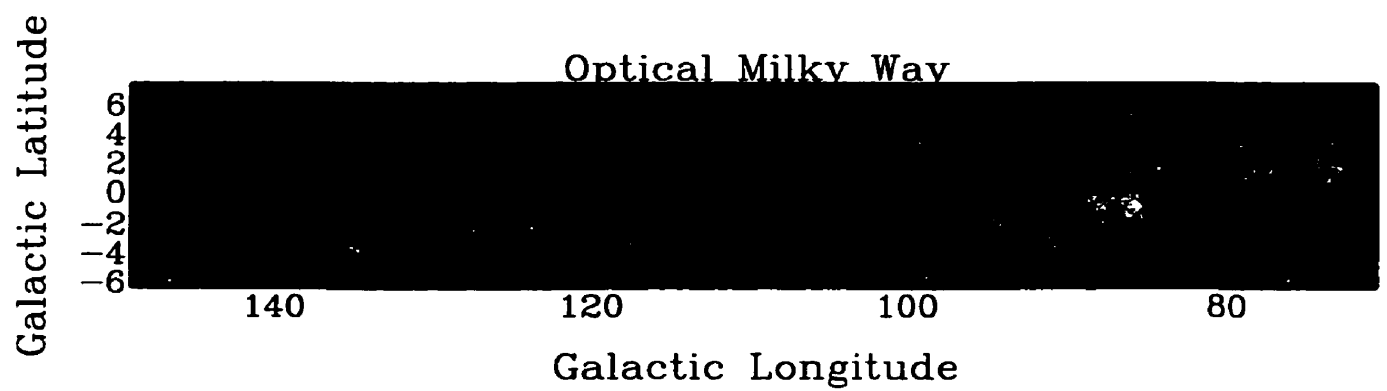


Figure 1.1: Depiction of the optical Milky way galaxy with the CGPS 21cm mosaics overlaid. The entire survey is covered by 36 mosaic images in two rows of 18. The four mosaics given at the extreme left contain the region analysed in this thesis.

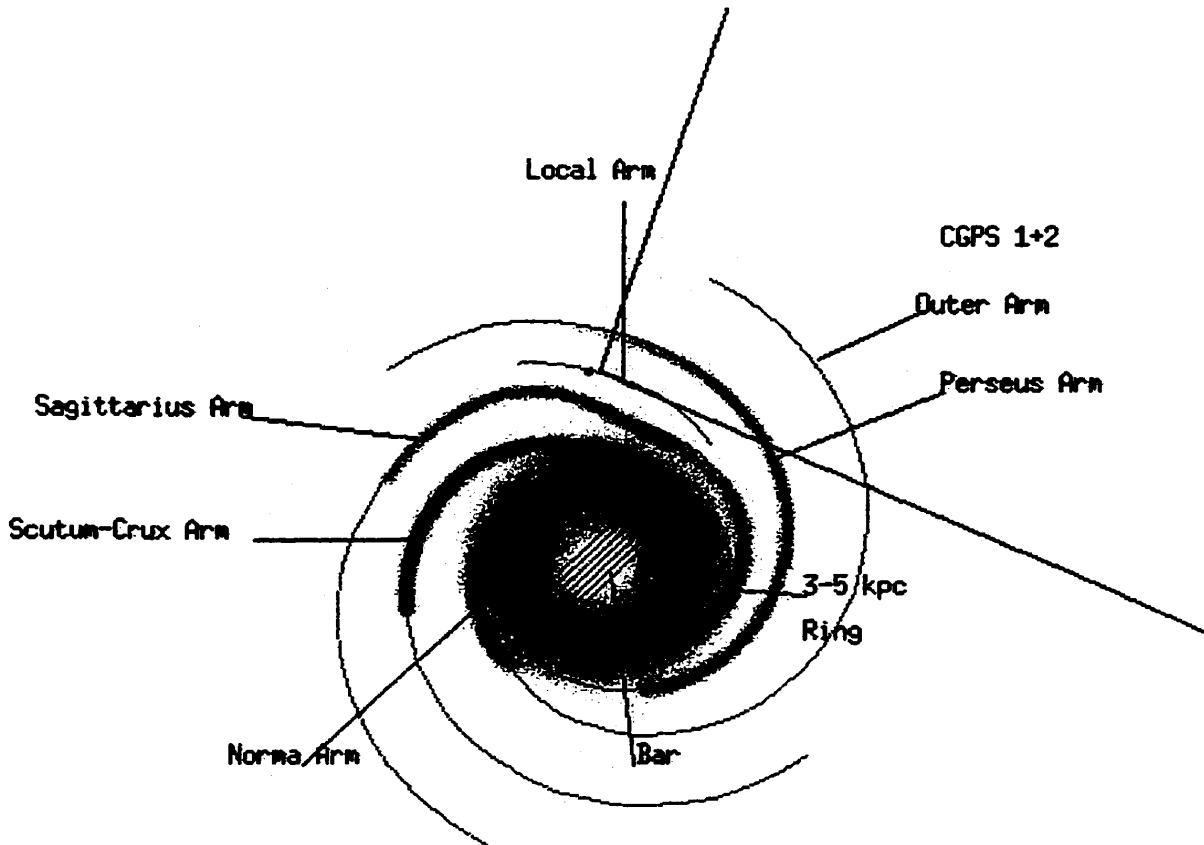


Figure 1.2: Depiction of the Milky way galaxy with the region covered by the CGPS

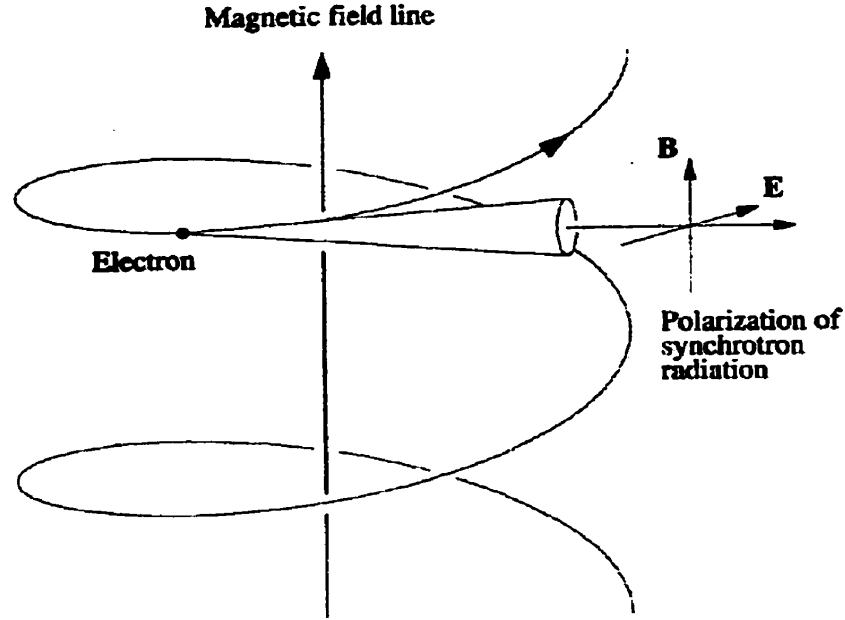


Figure 1.3: Synchrotron radiation emitted by a relativistic electron as it spirals around a magnetic field line. This figure is taken from Carroll and Ostlie pg. 615.

of the relativistic system:

$$E = \frac{mc^2}{(1 - \frac{v^2}{c^2})^{1/2}} = \gamma mc^2. \quad (1.2)$$

The electron spirals around the field line with a frequency of

$$\nu_o = \frac{eB_{\perp}}{2\pi\gamma mc}, \quad (1.3)$$

where e is the charge of the electron, $B_{\perp} = B \sin \theta$, and θ is the pitch angle of the electron with respect to the field. The observer on Earth will see the relativistic electron radiating into a narrow cone about its instantaneous velocity, shown in figure 1.4. The strongest emission from the electron is given off at the critical, or turnover, frequency (Salter & Brown 1988)

$$\nu_{crit} = \frac{3}{2} \gamma^2 \nu_o = \frac{3e}{4\pi m_o c B_{\perp} \gamma^2}. \quad (1.4)$$

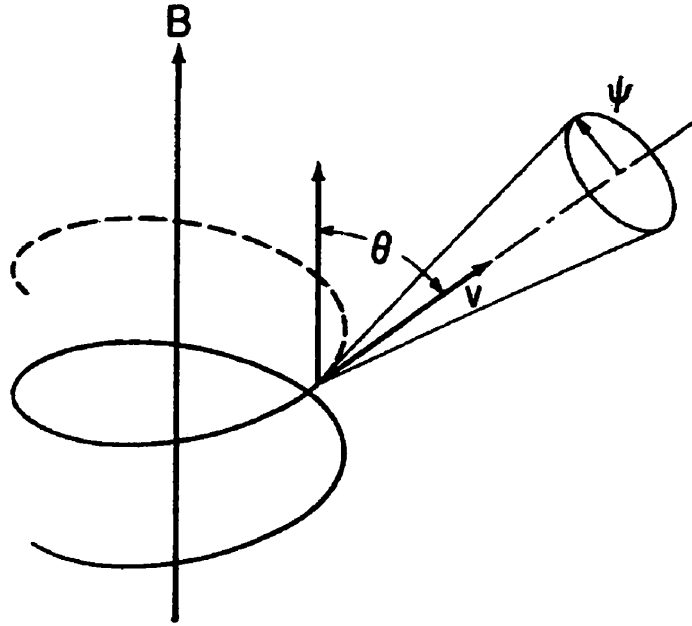


Figure 1.4: Synchrotron radiation emitted in a narrow cone by an electron spiralling around a magnetic field line. This figure was taken from Salter and Brown pg. 7.

The radiation received from a synchrotron source is from an ensemble of relativistic electrons each of which have different energies. To find the total power radiated and the flux density a power-law energy spectrum for the electrons is assumed, where the energy distribution is given by $N(E) \propto E^q$, where E is the electron energy, and q is the energy spectrum index. The total power radiated by an ensemble of electrons, with energy up to E is given by

$$P_{tot}(E) = \int_0^E P(\epsilon)N(\epsilon)d\epsilon, \quad (1.5)$$

where $P(\epsilon)$ is the power radiated by one electron. Since the power radiated by a single electron is proportional to its energy squared, the total radiated power can be written as

$$P_{tot}(E) \propto \int_0^E \epsilon^2 \epsilon^q d\epsilon = CE^{(3+q)}, \quad (1.6)$$

where C is a constant. The critical frequency (ν_{crit}) is also proportional to the energy

squared so the total power radiated in terms of frequency is given by

$$P_{tot}(\nu) \propto \nu^{(3+q)/2}. \quad (1.7)$$

Taking the derivative with respect to frequency gives the flux density (Butenhoff 1997)

$$\frac{dP_{tot}}{d\nu} \propto \nu^{(1+q)/2}. \quad (1.8)$$

There are two other important concepts of synchrotron radiation that also need to be considered. First the spectrum does not rise continuously without limit as the frequency decreases. Below some frequency the spectrum turns over (to a power law $+2.5$). This is a result of the plasma of spiralling electrons becoming opaque to their own emission – synchrotron self-absorption (Carroll & Ostlie 1996). This effect is similar to that of optically thick thermal radiation (explained below).

The other important effect of synchrotron radiation is the inverse Compton effect. This is a result of an ultra-relativistic electron, with Lorentz factor γ , encountering a photon and the collision resulting in the photon's frequency, ν , rising to roughly $\gamma^2\nu$. The exact change in frequency depends on the scattering geometry.

The inverse Compton process can be an important energy loss mechanism for synchrotron emitting electrons if the radiation density is high. The ratio of Compton losses to synchrotron losses is given by

$$\frac{L_C}{L_s} = \frac{U_{ph}}{U_B}, \quad (1.9)$$

where L_C is the emitted Compton luminosity, L_s is the emitted synchrotron luminosity, U_{ph} is the energy density of the photon field and U_B is the energy density of the magnetic field. This ratio is true for every electron and therefore must hold for

the entire ensemble. If we take the radiation field to be the synchrotron radiation of the source itself then the approximation

$$\frac{L_C}{L_s} \approx \left[\frac{T_b(\text{crit})}{10^{12} K} \right]^5 \left(\frac{\nu_{\text{crit}}}{10^{8.5} \text{ Hz}} \right) \quad (1.10)$$

shows that the Compton losses are relatively small for a source with a maximum brightness temperature of less than $10^{12} K$ (Shu 1991). At this brightness temperature the radio photons would be quickly shifted to the optical or beyond. More importantly however, the brightness temperature of $10^{12} K$ is in effect an upper limit on the brightness temperature of a synchrotron source. A source must be extremely energetic to produce a brightness temperature above this limit.

1.4 Bremsstrahlung Radiation

The other type of radiation seen in the galaxy is thermal, or Bremsstrahlung, radiation. Bremsstrahlung radiation results from a Coulomb interaction between an unbound electron and an ion. The electron passes by an ion which causes the electron to change direction, thereby accelerating. This acceleration results in the emission of a photon. The energy radiated in this way is small compared to the kinetic energy of the electron as it moves past the ion. For this type of radiation to occur in the radio range, the electron must encounter the ion from a far enough distance that the particles can be considered to continue along in almost the same direction. As the beginning and ending states of the electron are free states, this radiation mechanism is sometimes referred to as free - free radiation. Also, the energy states are not quantised and therefore the resulting radiation is continuous over the spectrum (Gordon 1988). Bremsstrahlung radiation is characterised by the mean energy of the

electrons and by the temperature of the gas – hence the term thermal emission.

To characterise the spectral behaviour of astronomical objects it is important to know some basics about the radiative transfer equation

$$\frac{dI_\nu}{ds} = -\kappa_\nu I_\nu + j_\nu, \quad (1.11)$$

where ds is the elemental path length, κ_ν is the absorption coefficient, and j_ν is the emission coefficient. The radiative transfer equation represents the change in brightness I_ν through a medium, where κ_ν and j_ν are properties of that medium. The above equation can be rewritten as

$$\frac{dI_\nu}{d\tau_\nu} = -I_\nu + S_\nu(T), \quad (1.12)$$

where $S_\nu(T)$ is the source function. For Bremsstrahlung radiation κ_ν and j_ν are such that the source function is equal to the Planck distribution function,

$$S_\nu(T) = B_\nu(T) = \frac{j_\nu}{\kappa_\nu}. \quad (1.13)$$

τ_ν is the optical depth and is given by the equation

$$\tau_\nu = \int_0^s \kappa_\nu ds, \quad (1.14)$$

and $d\tau_\nu = \kappa_\nu ds$. The optical depth represents what fraction of the radiation is lost in the medium. For an object to be optically thick its optical depth must be much greater than one, resulting in absorption of the radiation. An optically thin object has an optical depth of much less than one.

The radiative transfer equation can be solved for I_ν assuming that the received intensity is solely from the medium and that the source function is homogeneous and

isotropic. The resulting equation is:

$$I_\nu = \int_0^{\tau_\nu} B_\nu(T) e^{-\tau'_\nu} d\tau'_\nu = B_\nu(T)(1 - e^{-\tau_\nu}), \quad (1.15)$$

where T is the temperature, I_ν is the received intensity, and τ_ν is the optical depth of the medium. If the object is optically thick ($\tau_\nu \gg 1$) the above equation becomes

$$I_\nu = B_\nu(T). \quad (1.16)$$

In the radio range, where the Rayleigh-Jeans approximation to Planck's law can be used,

$$B_\nu(T) \approx \frac{2kT\nu^2}{c^2}. \quad (1.17)$$

So the object has a blackbody spectrum and the received radiation is proportional to the square of the frequency. If, on the other hand, the object is optically thin then

$$I_\nu \approx B_\nu(T)\tau_\nu, \quad (1.18)$$

and, since B_ν has a frequency squared dependence and τ_ν , for free-free absorption, has a $\nu^{-2.1}$ dependence (Salter & Brown 1988), the resulting radiation is nearly independent of frequency and the spectrum will appear flat. The connection between the optically-thick and optically-thin spectra is referred to as the spectral turnover.

The flux of a source is defined as

$$F_\nu = \int_{source} I_\nu d\Omega, \quad (1.19)$$

where Ω is the source solid angle, and is a power-law because if $I_\nu \propto \nu^\alpha$ then $F_\nu \propto \nu^\alpha$, where α is the spectral index and approximately equal to -0.1 for optically-thin thermal sources. In the optically-thick region the flux is still a power-law except

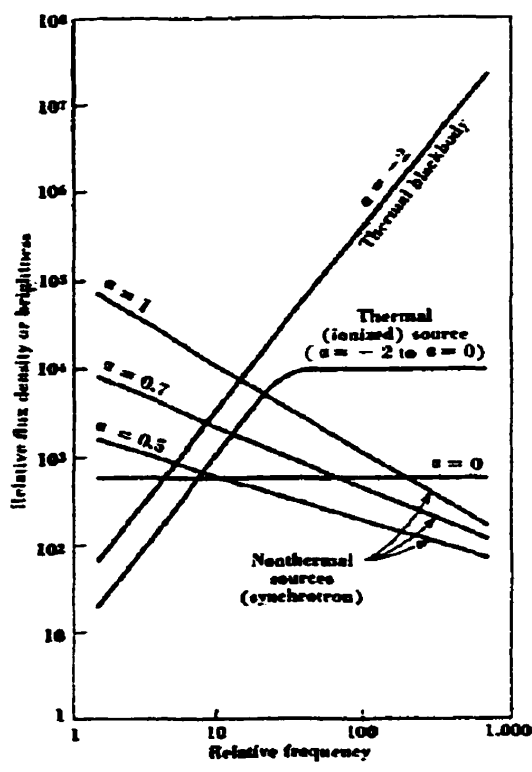


Figure 1.5: Spectrum for various values of spectral index α . This figure was taken from Kraus pg. 8-12, and it uses the inverse convention for spectral index. Negative α in this figure represents a thermal source and positive α represents a non-thermal source.

α is equal to two. Figure 1.5 shows the spectrum for samples of both thermal and non-thermal sources, as well as the spectral turnover between an optically thick and an optically thin thermal source.

1.5 Extragalactic Sources

Since the dust of the galactic plane is transparent to radio emission, the majority of compact sources found in the Canadian Galactic Plane Survey (CGPS) will be extragalactic sources. Previous surveys have detected upwards of 80% extragalactic

sources (Whiteoak 1993). These sources will be radio galaxies, quasars or other active galactic nuclei (AGN) as well as giant elliptical galaxies and Seyfert galaxies. A radio galaxy is commonly known as a galaxy that has bright radio emission, usually consisting of luminosities of $10^{48}W$ to $10^{53}W$. Radio galaxies emit by synchrotron radiation and have spectral indices of about -0.8.

Quasars are perhaps the most commonly known of the AGN. They are small galaxies with high redshifts and have extremely active centres, resulting from matter being accreted onto a supermassive blackhole. BL Lac objects are also AGN; theories have suggested that the mechanisms are the same and the difference between the objects comes from its orientation to the observer. Quasars have optical spectra that show intense broad emission lines suggesting the presence of highly ionised gas. Their radio spectra tend to be flat because the density of relativistic electrons is so great that the source becomes opaque to its own radiation. AGN are strong radio sources but in general only about 10% of the radiation is emitted at radio wavelengths, most of the power is radiated at submillimeter wavelengths (Kellermann & Owen 1988).

Seyfert galaxies are not strong radio emitters, so most known examples are in the nearby universe. They are usually spiral galaxies with an AGN. The core of a Seyfert galaxy will often show a low frequency spectral turnover as a result of free-free absorption by ionised gas in the emission line region (Kellermann & Owen 1988). Seyfert galaxies are classified into two types. Type 1 Seyfert galaxies have very broad optical emission lines that include the allowed lines H α , HeI and HeII, as well as some of the narrower forbidden lines such as [OIII]. Their broad allowed lines suggest a velocity between 1000 km/s and 5000 km/s, while the forbidden lines correspond to speeds of 500 km/s. Type 2 Seyfert galaxies only have narrow lines, both forbidden

and allowed. These lines indicate speeds of about 500 km/s. Seyfert galaxies also have a featureless continuum that comes from the central core. The majority of the luminosity from the type 1 Seyfert galaxy comes from this continuum, while the continuum observed from the type 2 is much less luminous (Carroll & Ostlie 1996).

1.6 Galactic Sources

Within the galaxy, compact radio sources emit both thermal and non-thermal radiation. The thermal sources consist of HII regions, planetary nebulae, and some types of radio emitting stars. Prominent non-thermal emitters are pulsars, supernova remnants, and radio emitting X-Ray binaries.

1.6.1 HII Regions

Of all the galactic radio emitting sources, HII regions are the most abundant. A survey of the southern galaxy at 843 MHz (Whiteoak 1993) found 360 sources, fifteen of which were HII regions, three were planetary nebulae, and two were stellar candidates. HII regions are the birthplace of massive O and B type stars. These stars ionise their surrounding clouds of neutral hydrogen by radiating chiefly at UV wavelengths. The radio emission from HII regions comes from the recombination of free electrons with hydrogen ions, or Bremsstrahlung radiation. There are several known types of HII regions.

The first type of HII region is the classical HII region. It was first identified using optical astronomy, and it is the largest of the three types. The effective temperature of the ionising star in any HII region is on the range of $3 \times 10^4 \text{ K} < T_* < 5 \times 10^4 \text{ K}$.

The typical electron density of a classical HII region is of the order of 10 cm^{-3} to 100 cm^{-3} and they have a mass ranging from 10^2 to 10^4 solar masses (Osterbrock 1989).

The second type of HII region is the Compact HII region. Compact HII regions have a diameter between 0.1 and 1.0 parsec ($1 \text{ pc} = 3.086 \times 10^{16} \text{ m}$). They are denser than the classical HII region, having an electron density of greater than 10^4 cm^{-3} (Habing & Israel 1979). They are believed to be surrounded by, or on the edge of, large masses of dust. This dust obscures the region at visible wavelengths, however, the radiation from the star heats the dust and the dust re-radiates in the far infrared. In most cases Compact HII regions are associated with OH and H_2O masers (Gordon 1988).

The final type of HII region is the Ultra Compact HII region. As its name suggests it is smaller than the Compact HII region, having a diameter of less than 0.15 pc. It is also more dense, with an electron density of greater than 10^5 cm^{-3} , and has very strong emission at $100 \mu\text{m}$. The CGPS expects to find Compact and Ultra Compact HII regions. Classical HII regions are larger and would not usually appear as compact sources. With the advancement of radio interferometry Classical HII regions have been seen to have structure on arcsecond scales (Gordon 1988).

1.6.2 Planetary Nebulae

Planetary Nebulae (PNe), despite their name have nothing to do with planets. The name results from the fact that some bright PNe “appeared as small, disk-like, greenish objects in small telescopes” (Osterbrock 1989). They are the thick shells of gas ejected from hot dying stars – a later stage of the low mass star’s evolution. The

central star, a white dwarf, is hotter than the ionising star of an HII region (about 5×10^4 K). The ionised envelope expands as it evolves, decreasing the density of the nebula. Because of the low luminosity of the white dwarf planetary nebulae are weak radio emitters. Their densities range between 10^2 to 10^4 cm^{-3} , and masses between 0.1 and 1.0 solar masses (Osterbrock 1989). Confusion between HII regions and PNe is possible on the basis of their emission alone. If the resolution of the observations allows for a description of morphology, further determination can occur.

1.6.3 Stellar Winds

Stars with strong stellar winds can emit both thermally and non-thermally. Winds from massive stars result in significant mass loss. UV radiation from the star ionises the wind, and the gas that is swept up emits thermally by Bremsstrahlung emission. This continuum emission has been observed in O and B type stars, with spectral index $\alpha \approx 0.7$, red giants, with spectral index $\alpha = 0.85$ and red supergiants with spectral index $\alpha \geq 1.0$. Wolf-Rayet stars are young hot stars with strong and wide spectral lines. They are almost always in binary systems and are non-thermal emitters (Zeilik et al. 1992). They do not fit the simple stellar wind theory of constant wind velocity. It has been suggested that they emit synchrotron radiation from relativistic electrons generated by turbulence or terminating shocks in the outer regions of the winds (Seaquest & Taylor 1990).

Another type of radio star is the VV Cephei Binary. This system consists of a red supergiant and an OB star. The OB star orbits inside the wind of the supergiant which is dense, cool and almost neutral. The orbiting star ionises a small region around itself, which is the major source of free-free emission (Hjellming 1988).

1.6.4 Symbiotic Stars

Symbiotic stars are thermal emitters. They are a binary system of stars consisting of a red giant and a hot compact object, usually a white dwarf. The system is surrounded by a nebula which is ionised by UV photons emitted by the white dwarf. The gas then re-radiates at a different frequency. These systems exhibit complex interactions between extended winds, outflows, and ionisation of subregions of the winds involved. They have a variety of steady radio emission, extended nebulosity, and have even shown moving jets. Their spectral index is between the range of 0.6 and 1.0 (Seaquest & Taylor 1990).

1.6.5 Novae

A nova occurs in a binary star system; one star loses mass to a smaller companion, again a white dwarf. Once the white dwarf has accreted enough matter a thermonuclear flash occurs and an explosion ejects a shell of ionised gas that emits thermally. Non-thermal emission has been seen in a small number of novae, this results from the interactions between the shell and the interstellar medium (Reynolds & Chevalier 1984). The classical nova, unlike the recurrent nova, only explodes once. The recurrent nova also occurs in a binary system, however, instead of two dwarf stars, this system contains a white dwarf and a red giant. Because of the red giant's stellar winds, the white dwarf can accrete more matter. The exchange of matter then causes an explosion, again by thermonuclear flash. This process occurs periodically as a result of the companion being a larger mass giant star with a stronger stellar wind (Hjellming 1988). The term Cataclysmic Variable is usually given to novae, as they eject matter suddenly and violently, changing their luminosity drastically.

1.6.6 Flare Stars

Flare stars are non-thermal radio stars. They radiate as a result of sudden outbursts from the stellar surface similar to a solar flare. The magnitude of these outbursts are more than what is seen in our sun, even at solar maximum (Kraus 1986). These sources are interesting because their mechanism for emission is not just synchrotron radiation. Flare stars are linearly polarised and have been observed as binary systems as well.

1.6.7 Radio Emitting X-Ray Binaries

The most luminous of all the radio stars is the radio emitting X-Ray binary. Cyg X1, a very strong candidate for a stellar mass black hole in orbit with an OB star, is a very bright source in X-Ray and it also emits in radio. X-Ray sources are very energetic; relativistic electrons expanding in cones have been seen from SS433, a pulsar-pulsar binary, and Cyg X3. Synchrotron radio emission is believed to come from the production of relativistic electron plasma regions behind strong shocks (Hjellming 1988).

1.6.8 Supernova Remnants

A Supernova Remnant (SNR) is an expanding cloud of gas from the outer layers of a star that was blown off during a supernova explosion. These sources are non-thermal emitters and are found close to the galactic plane. They can be distinguished from other non-thermal sources by their polarisation – usually greater than 5%. For these sources to be detected as compact sources in the CGPS they will have to be very young, as most known supernova remnants are large extended objects. The Kepler

SNR (1604 A.D.) is one of the smallest known and it has a mean diameter of 3 arcmin (Reynolds 1988).

There are three types of SNR. The first is the shell type which has bright emission from a ring like structure centred on the progenitor. Young shell type SNR have steeper spectra. Another type of SNR is the filled centre remnant. There is no visible shell structure and the emission comes from the central region, these are not very common, only about 10% of known SNRs. The final type of SNR is the composite type. It has characteristics of both types, bright central region and a visible shell. The spectrum is less steep than the shell type but not as flat as the filled centre. The spectral index of the supernova remnant varies. The shell type and composite type have a spectral index between -0.6 and -0.8, where as the Crab nebula has a spectral index of about -0.3 (Reynolds 1988).

The spectrum of the SNR and its polarisation suggest the mechanism for emission is synchrotron radiation from distributions of electrons, or positrons, radiating in a magnetic field. There are multiple theories as to the origin of the emission, consisting of the original supernova event, the pulsar inside the remnant, ambient cosmic rays, or the acceleration of particles at the shock wave or between the shocked ejecta and the shocked interstellar medium. The first suggestion receives little attention as the volume of the SNR is very large and energy would be lost in the expansion, resulting in a much shorter lifetime of the SNR than what is observed. The pulsar suggestion seems likely for the filled centre SNRs; however, it does not explain shell-type SNR. Therefore the most likely mechanism is that of the acceleration of particles at the shock wave or between the ejecta and the ISM. In this scenario particles would collide with randomly moving interstellar clouds and would be reflected by the presumably

higher magnetic field in the clouds (Reynolds 1988).

1.6.9 Pulsars

Pulsars are rotating neutron stars. A neutron star is an extremely high density ($\rho \approx 4 \times 10^{16} \text{ kg/m}^3$) star that is small in size. It is made of degenerate neutrons, and results from a supernova explosion. The pulse occurs because the pulsar's beaming axis is inclined with respect to the rotational axis. As the neutron star rotates the beam sweeps through an area of the sky, similar to the effect of a lighthouse. For this reason a pulsar can be seen only if the observer is in the preferred region of the emission. The emission from a pulsar is non-thermal, and tends to be weak ($S_{408} \approx 10.0 \text{ mJy}$, $S_{1420} \approx 1.5 \text{ mJy}$) (Butenhoff 1997). Some important characteristics are that pulsars are found close to the galactic plane, they have very steep spectra ($\alpha < -1.5$ usually on the order of -2), and some pulsars have a flattening or turnover in this spectrum at low frequencies ($\approx 100 \text{ MHz}$) (Izvekova et al. 1981). They also have a high degree of linear polarisation.

The low frequency turnover in the spectra is believed to be a result of synchrotron self-absorption or due to line-of-sight absorption from the ISM between the pulsar and the observer (Sieber 1973). This flattening occurs at low frequencies and therefore should not appear in the CGPS data set. It is important to note that millisecond pulsars do not exhibit this flattening of spectra (Erickson & Mahoney 1985), and they also have a steeper spectrum than normal pulsars (Johnston & Bailes 1991).

The rotational characteristics of a pulsar can explain other properties of the object. The rate of pulsation implies that their emitting region is no larger than 300 km, and the stability of the rotation suggests that they are of stellar mass.

The pulsar PSR1937+21 spins at 642 Hz and rotates as fast as a neutron star can before becoming unstable; the rotation speed is about one tenth that of the speed of light. Theory predicts that the periods of pulsars should lengthen as the stars decelerate due to energy loss. The slow decay of the rotation period is attributed to “the electromagnetic torque on the star that is generated by the rapid rotation of the off-axis dipole magnetic field” (Backer 1988).

1.7 Spectrum of galactic and extragalactic sources

Galactic sources are primarily thermal sources. HII regions, both compact and ultra compact, and planetary nebulae are all thermal emitters. Their spectra are classified according to a steep positive spectral index similar to a true blackbody. There may be a spectral turnover at higher frequencies due to a change in optical depth. Sources that are always optically thick have spectra like a blackbody radiator, while optically-thin sources have a high frequency turnover.

Non-thermal emitters have negative spectra. Pulsars have a mean spectral index of about -1.6, but can be lower than -2. Supernova remnants have spectral indices that vary according to the type of remnant. Shell remnants have spectral index of about -0.49, while for filled centre remnants $\alpha = -0.2$. The composite type results in a spectral index between these two numbers, typically $\alpha \approx -0.45$ (Butenhoff 1997). Another source quotes a spectral index between $\alpha = -0.6$ and $\alpha = -0.8$ for SNR (Reynolds 1988).

Extragalactic sources have spectral indices over a wide range. Some have flat spectra with $\alpha = -0.5$, while others can have steep spectra with $\alpha = -1.8$. There

are very few positive spectra objects, therefore positive spectra sources are mostly galactic. Due to the overlap of spectral indices, polarisation is essential in determining the exact nature of a non-thermal source (Kellermann & Owen 1988).

1.8 Variability of Sources

Many types of compact sources vary in brightness. Sources in our galaxy, such as X-Ray and γ -Ray binary star systems, novae, pulsars, and Wolf-Rayet stars, as well as compact sources outside our galaxy have shown variability. Beyond the Milky Way, variability occurs in very compact extragalactic radio sources such as AGN, and quasars. Compact extragalactic sources commonly vary on a timescale of a few months. Studies have shown that these variables represent about 5% of the total population of extragalactic sources (Gregory & Taylor 1986). Only very compact flat-spectrum sources vary at 1.4 GHz. No correlation between the degree of variability at 1.4 GHz and galactic latitude has been found. This suggests that the variability is intrinsic to the source and not a result of scintillation in the interstellar medium (Rys & Machalski 1990a). A very small fraction of compact extragalactic variable sources vary in flux on a timescale of a week. The most rapid variation in an extragalactic source is in the BL Lac objects. Variability can be described as an outburst that is strongest at high frequencies and reduced at lower frequencies. However, the variations that occur at frequencies less than 1 GHz appear to be unrelated to those that are observed above 1 GHz, and may be due to a different mechanism (Kellermann & Owen 1988).

In the early study of compact radio source variability, it was found that if sources

were considered in terms of conventional synchrotron models, rapid variations implied excessively high brightness temperatures. This problem results from the fact that if an object varies coherently on a timescale τ , then the dimensions of the radiating region must be less than $c\tau$, where c is the speed of light. Using the redshift-determined distance an upper limit on angular size can be determined. From the angular size, a brightness temperature can be calculated, and usually the value is often found to be greater than 10^{12} K, particularly for variability observed at frequencies less than 1 GHz or a timescale of much less than one year. This is not possible for an incoherent synchrotron source (see section 1.3). Variability of extragalactic sources on a timescale of a few hours to days is usually a result of scintillations in the ionised ISM.

Within the galaxy, intrinsic variability can occur on a much shorter timescale. This is because the source dimensions are much smaller and thus less time is required for the entire source volume to change intensity. Highly variable sources come from very energetic outbursts that produce relativistic particles resulting in synchrotron radiation. An example of this is the radio emitting X-Ray or γ -Ray binary star system, or magnetically active systems such as RSCVn stars. As these stars are synchrotron emitters, polarisation may also be present. Pulsar variation on a timescale of less than 1000 seconds should be intrinsic to the source, but pulsars have also been known to vary on a timescale of several months (Backer 1988).

A SNR that is less than 1000 years old may be expected to vary in flux by the small amount of 1/10th of a percent per year. It was predicted, by Shklovskii in 1960, that even the radio flux from Cas A was variable. The variability of Cas A showed a decrease in flux density at a rate of one percent per year. Observations of

this variability were quickly confirmed as Cas A is the brightest source in the radio sky at some frequencies, and is commonly used for calibration. It has now been shown that this decay rate is frequency dependent and that the spectrum flattens out with time, which is thought to be a result of turbulent shock acceleration of particles (Reynolds 1988). Most supernova remnants are not as bright as Cas A and detection of their variability is much more difficult.

Since the wavelengths of radio emission are not absorbed or scattered by interstellar or intergalactic medium, variable searches that probe the disk of the galaxy, will be sensitive to both galactic and extragalactic sources. Galactic objects such as supernova remnants can be useful tools in determining properties of the interstellar medium. The existence of pulsars allows the study of later stages of stellar evolution, and flare stars allow for earlier stellar evolution studies. All of these sources can be identified through radio source variability. Extragalactic sources give insight into cosmological studies by allowing the study of young active galaxies. Variable studies are perhaps most useful for their insight into the types of mechanisms involved in variability. For this reason it is important to study the frequency dependence of amplitude and the timescales of variability. Also, the statistics of variable occurrence and their distribution in the sky are invaluable to understanding our universe.

1.9 Past Radio Variable Searches

Radio searches for variable sources have been done in the past. Four of these searches are described here. A 408 MHz study was carried out between 1995 and 1996, looking for sources that vary on the order of one year (Riley & Green 1998). This study

considered sources at a galactic latitude of 15 degrees ($b = 15^\circ$). The observations were taken a year apart and source positions were matched within their uncertainties. Source variation was found using the fractional change in flux density. Any source with fractional flux density greater than 3σ (where σ is the square root of the variance of the fractional flux density) was considered a variable. The sample size was 322 sources, and five possible variables were found – four definite. This indicates an expectation of 1.2% variability at 15 degrees latitude and 408MHz frequency. Another study at 408 MHz and 58° revealed no variable sources.

A survey of strong sources at 1.4 GHz was performed on a 0.54 sr area of the sky using the Green Bank 92 m telescope between 1970 and 1975 (Rys & Machalski 1990b). Data was compared to the Condon and Broderick ‘Atlas’, observed in 1983, resulting in a long term variable search over a timescale of 8 to 13 years. This ‘Atlas’ contains over 3600 sources, with flux greater than 100 mJy, within this region of the sky. Over 500 of these sources had different peak flux densities from one epoch to the next. A source was considered to be variable if $|\frac{\Delta S}{\sigma_{\Delta S}}| \geq 3.29$, where S is the flux density, and a possible variable if the ratio was in the range of 2.58 to 3.29. It was found that there was no significant difference between variability at different galactic latitudes at 1.4 GHz, unlike the B 3 survey (Gregorini et al. 1986) at 408 MHz.

The Westerbork Survey covered about 140 square degrees of the galactic plane to resolution of about 1 arcmin, at 327 MHz (Taylor et al. 1996). The survey considered sources on a timescale of a few years whose peak intensity was greater than 5 times the RMS noise level. Sources also were required to have dimensions less than a few arc minutes to be considered compact. The fractional change in flux density was found with an associated uncertainty, and from that a variable index was determined.

The variable index was determined for each source using $V_I = \frac{\Delta}{\sigma_\Delta}$ where $\Delta = \frac{(S_1 - S_2)}{(S_1 + S_2)}$ and S is flux density. Variables were defined as objects that had a variable index of greater than 3.5 – only 19 were found out of 2148 sources, less than 1%.

An older survey covering over 200 square degrees of the galactic plane at 4.85 GHz was started in 1977 (Gregory & Taylor 1986). This survey searched for variables on the timescale of a few days to a few years. Short term variables are primarily galactic sources, whereas the long term variables are primarily extragalactic sources. This survey also used the variable index method for determining variables. However, this could leave out sources that vary for a small fraction of the time. So, another index was used to measure the largest deviation from the mean signal. The expected variables were found in the range of 3.0 to 3.5. Of the 1274 discrete radio sources, 32 variables and 27 possible variables were found, 2.5% variable sources and 2.1% possible variables.

From the above summary of some past variable searches, it can be seen that variability in radio sources is dependent on frequency. A source that varies at low frequencies does not necessarily vary at higher frequencies. Galactic latitude also plays a role in variability as noted by the 408 MHz survey. It is believed that the variability of an object depends strongly on the “intrinsic compactness of the source” (Rys & Machalski 1990b); therefore it also relates to the spectral index of the source.

The CGPS variable search is different than the above 1.4 GHz searches in that it is a survey considering all compact sources in an 81 square degree area of the galactic plane. The method of determining variables is similar to the 408 MHz and the Westerbork surveys. However, the CGPS is more sensitive by at least a factor of 10 in detecting radio sources, and therefore variables, than the previous most

sensitive surveys. Hence the CGPS samples a new population of faint radio sources in the plane of the galaxy.

Chapter 2

Data

The Canadian Galactic Plane Survey is a project undertaken by a large consortium of scientists. The data acquisition and processing was done by the consortium members at the Dominion Radio Astrophysical Observatory (DRAO) prior to the start of this thesis. The following chapter is an overview of what was done to produce the data used in this thesis.

2.1 Observations

The observations for the CGPS began in April 1995, using the DRAO synthesis telescope. It is a seven element east-west array with a maximum baseline of 604 m and a minimum baseline of 12.9 m. Each dish in the array is a 9 metre parabolic antenna with a 2.5 degree field of view at 21 cm. The CGPS data were collected using 12 hour observations of a field in each of 12 array configurations. The survey covers a 70° range in galactic longitude from $l = 70^\circ$ to $l = 145^\circ$ (from Cygnus to Perseus) and 9° in latitude centred on the galactic plane. The CGPS has an angular resolution of $1' \times 1' \text{cosec}(\delta)$ with sensitivity of 0.2 mJy/beam at 21cm and angular resolution $3.5' \times 3.5' \text{cosec}(\delta)$ with sensitivity 3 mJy/beam at 74 cm (δ is the declination). Covering the survey region are 190 observed fields in five rows centred on the galactic plane. At 21 cm these fields are clustered into 36 mosaics each of which are $5.1^\circ \times 5.1^\circ$ squares. At 74 cm there are only 6 mosaics, each $15^\circ \times 15^\circ$.

The telescope has a total bandwidth of 30 MHz at 21 cm, but in order to avoid bandwidth smearing effects over the field of view this is divided into four 7.5 MHz channels. At 74 cm a single channel of 4 MHz is used. Both right and left hand circular polarisation information is obtained at 21cm, allowing images of all four Stokes parameters to be made (Taylor 1999). Only left hand circularly polarised information is collected at 74 cm. The mosaic images have non-uniform noise distribution over the image as a result of primary beam attenuation as a function of radial distance from the centre of the field. Also, the dimensions of the beam vary slightly with position due to the declination dependence of the resolution. The information about noise and resolution as a function of position in a map is recorded in the corresponding weight maps and beam arrays respectively. These maps are then used in the production of the mosaic.

Observations taken using the Effelsberg single-dish 100m radio telescope at 21 cm are used to cover the “short-spacing” region less than 12.9 m. This survey covers the range between $95.5^\circ < l < 240^\circ$ and $-4^\circ < b < +4^\circ$. The sensitivity of the survey is 100 mK in brightness temperature ($\approx 50\text{mJy}$) with an angular resolution of 9.4 arcmin, Full Width at Half Maximum (FWHM). The observations were taken between 1982 and 1988, with some areas being re-observed between 1990 and 1994. The majority of observations were taken with a central frequency of 1408 or 1410 MHz, and a bandwidth of 20 MHz. Because of interference, this bandwidth was occasionally reduced to 10 MHz (Reich et al. 1997). The 74 cm short spacings information comes from the all sky survey using the Jodrell Banks, Effelsberg, and Parkes telescopes (Haslam 1983). The data for both the 21 cm and 74 cm short spacings are added to the DRAO data.

2.2 Basic Interferometry

The principle of radio interferometry is not unlike the principle of Young's double slit experiment. Each individual telescope in an interferometric array functions in the same way as a single dish, except the resolution of an interferometer is improved with longer baselines.

The following discussion illustrates the two element correlator interferometer depicted in Figure 2.1. As shown in the figure, the distance d is the baseline of the array, θ is the pointing angle, and L is the geometric delay. If this interferometer was observing a source, some distance S away, the radiation would arrive at telescope A, a short time before arriving at telescope B. The difference in the arrival times is called the geometric time delay. The signals received from the telescope are in phase if L is equal to an integral number of wavelengths ($L = n\lambda$). This superposition results in a maximum signal – constructive interference. Destructive interference occurs when the signal is out of phase, or when L is an integer of half wavelengths ($L = \frac{n\lambda}{2}$). Since the pointing angle θ is related to the baseline d , and the geometric delay L by $\sin \theta = \frac{L}{d}$. The position of the source can be accurately determined using the interference pattern (Carroll & Ostlie 1996).

The signals from the antennas pass through amplifiers which incorporate filters to select the required frequency band of width $\Delta\nu$ centred on frequency ν . The signals are then combined with a correlator which is a voltage multiplier followed by a time averaging circuit (Thompson 1999). If the signals received by the two different telescopes have a difference in phase, it is a result of both the geometric time delay τ_g , and the electrical phase delay between the two telescopes, τ_D . Both

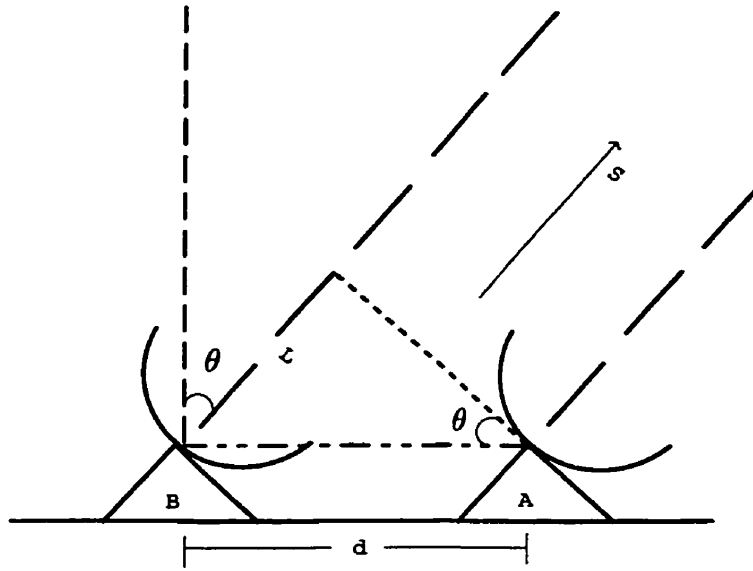


Figure 2.1: Depiction of a two element interferometer. Where d is the baseline, L is the geometric delay, s is the direction of the source, and θ is the pointing angle.

of these can be controlled, as described below.

For a monochromatic signal at angular frequency ω , the output of the two-element correlator interferometer averaged over time T is proportional to:

$$\Gamma(\tau) \propto \frac{E^2}{T} \int_0^T \cos \omega(t) \cos \omega(t + \tau) dt. \quad (2.1)$$

τ can be written as $\tau_g - \tau_D$, giving

$$\Gamma(\tau) \propto \frac{E^2}{T} \int_0^T \cos \omega t \cos \omega(t + \tau_g - \tau_D) dt. \quad (2.2)$$

Using the trigonometric identity $\cos(A + B) = \cos A \cos B - \sin A \sin B$ the above equation becomes:

$$\Gamma(\tau) \propto \frac{E^2}{T} \int_0^T \cos \omega t [\cos \omega t \cos \omega(\tau_g - \tau_D) - \sin \omega t \sin \omega(\tau_g - \tau_D)] dt \quad (2.3)$$

which reduces to

$$\Gamma(\tau) \propto \frac{E^2}{T} \left[\cos(\tau_g - \tau_D) \int_0^T \cos^2 \omega t dt - \sin \omega(\tau_g - \tau_D) \times \int_0^T \cos \omega t \sin \omega t dt \right]. \quad (2.4)$$

The last integral in the above expression is zero, and the first is evaluated to be $T/2$. This simplifies the equation to be

$$\Gamma(\tau) \propto \frac{E^2}{2} \cos[\omega(\tau_g - \tau_D)] \quad (2.5)$$

This relation shows that the output from the interferometer varies periodically. Since aperture synthesis (described below) is used to produce a complete image it is important to consider the effects of the rotation of the earth. As the earth rotates, the angle θ varies as the interferometer tracks the source. This effect changes the geometrical time delay τ_g , producing interference fringes as the relative phase of the incoming radiation between the two elements varies with time. The correlation output is constant if the fringes are stopped, that is if $\tau_g = \tau_D$. The interferometer is then steered electronically by adjusting the electronic time delay to be equal to the geometrical time delay. This direction is called the delay centre.

The above argument only deals with the time periodicities. The correlated output from a source at the pointing centre of the beam, $\theta = \theta_o$, will not exhibit fringes over time. However, a source at some distance $\Delta\theta$ from θ_o will have a geometric delay different from τ_g . Therefore, the electronic time delay previously used to offset the geometric time delay, will not offset the geometric time delay of the second source exactly the same way. Thus, the amplitude of the second source will be modified by a cosine factor depending on its distance $\Delta\theta$. Sources away from the delay centre have a "phase" offset perpendicular to $\Delta\theta$. The flux density in the θ_o direction can be given by:

$$S_\nu(\theta_o) = \int I_\nu(\theta) A(\theta - \theta_o) e^{i2\pi \left[\frac{d \sin \theta}{\lambda} - \frac{c\tau_D}{\lambda} \right]} d\theta, \quad (2.6)$$

which can also be written in terms of the dot product of the baseline and the source

direction vector, \vec{d}_λ and \hat{s} respectively.

$$S_\nu = \int I_\nu A e^{i2\pi(\vec{d}_\lambda \cdot \hat{s} - \frac{cT}{\lambda})} d\Omega \quad (2.7)$$

2.2.1 The uv and lm -planes

Aperture synthesis is the rotation of an object with respect to the interferometer's pattern, which is practically achieved at the DRAO using an east-west array and observing for a 12 hour time period. This allows the Earth's rotation to effectively synthesise an aperture with a diameter equal to the largest baseline.

The uv plane is the plane that is traced out by the baselines of the interferometer during aperture synthesis. This plane is always perpendicular to the line of sight. The (u, v, w) coordinate system is defined so that the direction to the source is in the \hat{k} direction, and w is the projection onto this axis. The u -coordinate is the projection of the baseline onto the \hat{i} axis, and the v -coordinate is the projection onto the \hat{j} axis. The \hat{i} axis lies along the east-west plane and the \hat{j} axis lies along the north-south plane.

The lm plane is the projection of the celestial sphere (of radius 1) onto a tangent plane with the tangent point being at the intersection of the \hat{k} axis and the celestial sphere. The celestial sphere has unit radius and is centred at the origin of the coordinate system. The (l, m, n) coordinate system is defined to be the directional cosines with respect to the uv -plane. The direction of a line in space is given by the three angles, called the direction angles of the line, which are made with the coordinate axes; the cosines of these angles are the directional cosines. the (u, v, w) and (l, m, n) coordinate systems are used to define a fundamental result of radio

astronomy, the existence of a Fourier Transform relationship between the visibilities and the sky brightness.

Equation 2.7 can be converted into (u, v, w) coordinates and (l, m, n) coordinates using

$$\frac{\nu \vec{d} \cdot \hat{s}}{c} = ul + vm + wn,$$

$$\frac{\nu \vec{d} \cdot \vec{s}_o}{c} = w,$$

and

$$d\Omega = \frac{dldm}{n} = \frac{dldm}{\sqrt{1-l^2-m^2}}, \quad (2.8)$$

resulting in

$$S_\nu(u, v, w) = \int_{-1}^1 \int_{-1}^1 A(l, m) I_\nu(l, m) e^{i2\pi[ul+vm+wn-\frac{c\tau_D}{\lambda}]} \frac{dldm}{\sqrt{1-l^2-m^2}} \quad (2.9)$$

The electronic delay is usually set so that $\frac{c\tau_D}{\lambda} = w$. The interferometer directly measures the visibility function; this function is derived from the flux density equation by integrating over frequency, so that

$$V(u, v, w) = \int_{-1}^1 \int_{-1}^1 A(l, m) I(l, m) e^{i2\pi[ul+vm+w\sqrt{1-l^2-m^2}-w]} \frac{dldm}{\sqrt{1-l^2-m^2}}. \quad (2.10)$$

This equation can be simplified with the help of two assumptions. The first is the small field approximation, where only the regions close to the phase centre are considered ($|l|$ and $|m| \ll 1$). The second approximation is that $A(l, m)$ goes to zero for large values of l or m . These approximations result in the final visibility equation,

$$V(u, v) = \int_{-\infty}^{\infty} \int_{-\infty}^{\infty} A(l, m) I(l, m) e^{i2\pi[ul+vm]} dldm. \quad (2.11)$$

This equation is the fundamental Fourier Transform relationship between visibility and sky brightness, where $A(l, m)I(l, m)$ is the sky brightness distribution modified by the antenna pattern. The inverse Fourier Transform is given by

$$A(l, m)I(l, m) = \int_{-\infty}^{\infty} \int_{-\infty}^{\infty} V(u, v)e^{i2\pi[ul+vm]}dudv, \quad (2.12)$$

(Thompson 1999).

2.3 Data Processing

The first step in the processing of data is the calibration. This is done in two parts.

2.3.1 Amplitude and Phase Calibration

The phase and amplitude calibration of the visibility data is done using the DRAO program phase 1 (PH1). This program calibrates the instruments and converts the measured voltages into flux densities. The calibration is done using a calibrator source in the sky that has some important properties. It should be an unresolved source (Unresolved sources have a constant amplitude and a phase of zero.) that does not vary over the timescale of the observations. It should have an accurately measured position. The source should be strong and have a known, simple spectrum. Finally the source should be isolated from nearby confusing sources. This calibrator is used to determine the antenna phase offset, as the phase of a point source at the delay centre should be zero.

The amplitude and phase is corrected for each baseline. For baseline between antennas i and j , the baseline-based complex gain $G_{ij}(t)$ is given by:

$$G_{ij}(t) = g_i(t)g_j^*(t) = a_i(t)a_j(t)e^{i(\phi_i(t)-\phi_j(t))}, \quad (2.13)$$

where $g_i(t)$ and $g_j(t)$ are the associated antenna-based complex gains, $a_i(t)$ is an antenna based amplitude correction, $\phi_i(t)$ is the antenna based phase correction, and $*$ is the complex conjugate. The observation of the calibrator source determines $G_{ij}(t)$ for each of the baselines. Observations of the calibrator source are taken before and after each 12-hour observation. Changes in atmospheric conditions between calibration observations can cause variations in that offset. The calibrator is also not in the same location of the sky as the source observations. This can cause small errors, as different atmospheric conditions may exist between the two pointing directions.

2.3.2 Fourier Transformation and Mapping

The second phase of the calibration is responsible for producing the raw (dirty) map by Fourier Transforming the visibility function. This process is performed using the DRAO program phase 2 (PH2), which uses the technique of Fast Fourier Transformation (FFT). This transformation requires, in principle, that the visibility function is specified everywhere. Observations only provide values of the visibility function for certain points on the uv plane. Therefore, a modified visibility function is constructed. This modified visibility function is the product of the observed visibility function and the sampling function; where the sampling function is equal to one whenever the visibility function is sampled, and zero whenever it is not. This makes the sampling function a series of δ -functions. The Fourier Transform of the sampling function will then be the synthesised beam (response to a point source). The Fourier Transform of the modified visibility function is the dirty map convolved with the synthesised beam. The dirty map is the true sky brightness multiplied by the primary

beam pattern of an individual element of the array (Briggs et al. 1999).

2.3.3 CLEAN

The CLEAN program is used to remove the artefacts caused by incomplete sampling of the Fourier plane. The beam is also CLEANed so as to produce a single point spread function or Gaussian shaped beam. This program uses both the Clark CLEAN algorithm, in a modified form, and the Steer algorithm. It starts with the Clark algorithm and CLEANs the map down to a level set by the user, then the algorithm switches to Steer and the program continues to CLEAN (Higgs 1994). The Hogbom CLEAN algorithm is the original algorithm and is as follows. The strength and position of the peak in the dirty beam are found. The dirty beam is multiplied by the peak strength and a damping factor (loop gain γ) and is then subtracted from the dirty image. A record of the positions and magnitudes of the point sources that were subtracted are recorded in a model. This process is repeated until all remaining peaks are below the user specified limit. The point source model is then convolved with an idealised CLEAN beam to form a CLEAN image. Finally the residuals of the dirty image are added to the CLEAN image. The number of iterations done using the CLEAN algorithm depends on the amount of real emission in the dirty image. Usually CLEAN is performed until all the brightness greater than the noise level is transferred to the CLEAN map. If low surface brightness extended emission is desired, then CLEAN will have to be performed deeper (Cornwell et al. 1999).

2.3.4 Self Calibration

The CLEAN map is not completely free of artefacts. There are still some residual errors from the calibration process that need to be removed. The aim of self calibration is to produce a model of the sky intensity distribution which, when corrected by the complex gain factor, reproduces the observed visibilities to within the noise level. The model is made using the CLEAN map. It is also important to exclude any features of the model that are due to the calibration errors trying to be removed. Otherwise, the errors are simply propagated. Self calibration, like CLEAN, is an iterative process. First, a constrained model of the source is made from the CLEAN map. Then the model is divided into the observed visibility, which in the absence of error would produce uniform amplitude and zero phase for each baseline. In presence of error the results deviate from this. New complex gains are then calculated and the correct visibility can be determined using the following equation

$$V_{ijcorr}(t) = \frac{V'_{ij}(t)}{g_i(t)g_j^*(t)}, \quad (2.14)$$

where $*$ is the complex conjugate. The corrected visibility can be used in a new model, again with constraints. This process is continued until the user is satisfied with the model. Self calibration has been found to be most successful for arrays with a large number of elements, as the ratio of visibility constraints to unknown gains for phases and amplitudes rises without bound as the number of elements increases (Cornwell & Fomalont 1999).

2.3.5 Short spacings and Mosaicing

Prior to mosaicing, the individual DRAO fields must be registered. This process compares the DRAO fields with the NRAO VLA sky survey (NVSS). The positions and fluxes of strong sources are matched between the two surveys, and a correction for each is applied to the individual DRAO fields. That is, if the positions of the sources in the field differ from those in the NVSS, then one correction is applied to the entire field. The same holds true for the fluxes. To this point the above processing has been done to each individual field of the DRAO data. The short spacings data collected at Effelsberg are then added. Once all of the above processing is complete, the data are ready for mosaicing. The mosaicing process adds together overlapping fields to produce the 5.1×5.1 degree images used in this thesis.

Chapter 3

Source Detection and Parameter Measurement

Analysing large quantities of compact sources found in a number of different fields required the use of automated source detection and fitting programs, provided by the DRAO. The programs were used in the past by Butenhoff (1997), in his work on the Galactic Plane Survey Pilot Project, and he showed that these programs were not completely effective.

In the present work, many tests were run on artificial data prior to the actual processing of the Survey data to determine the performance of the program. Presented below are the details of the automated source fitting programs, FINDSRC, FLUXFIT and the artificial source producing software GAUSSMAP. Also presented are results of the tests and the subsequent changes made to the software.

3.1 FINDSRC

FINDSRC is a program to locate compact and slightly extended sources in an image. To help identify “point sources” in the presence of more extended emission, the images are first convolved with a Morlet wavelet. Wavelet analysis is used to detect and locate features in an image. The wavelet transform is a set of filters using a mask with varying size. This leads to the decomposition of the image into a set of maps showing structures at given scales (Coupinot et al. 1992). FINDSRC uses the wavelet to filter out extended emission thereby enhancing the compact sources. The

Morlet wavelet function has the following form (Figure 3.1):

$$G(x, y) = (1 - \ln 16 \times f(X, Y)) \times e^{(-\ln 16 \times f(X, Y))} \quad (3.1)$$

where

$$f(X, Y) = X^2 + Y^2$$

and

$$X = (x \times \cos A + y \times \sin A) / B_{maj}$$

$$Y = (y \times \cos A - x \times \sin A) / B_{min}$$

Where B_{maj} , B_{min} , A are the beam major halfwidth, minor halfwidth and position angle of the major axis respectively. The width of the central peak of the function is thus scaled to match the dimensions of an unresolved source.

The output of FINDSRC is a box file, consisting of a box size and centre for each of the sources found. In the case of crowded fields, larger boxes are created and two or three sources are clustered into the larger boxes. Slightly extended sources can be found by means of an option to clump two or three point source components into one source. The source fitting program FLUXFIT then fits an extended source to that box. If the clumping option is not selected these sources will either be ignored due to their extended nature, or they will be represented as two or three components of a point source. For this reason slightly extended sources must be treated carefully. Double or triple sources are dealt with the same way, except they are recorded as components of a single source instead of individual sources.

FINDSRC can check these boxes for potential problems in base-level fitting. If there is a problem, these boxes are marked as deleted and will not be analysed by

Morlet Wavelet for MV1 Beam Parameters

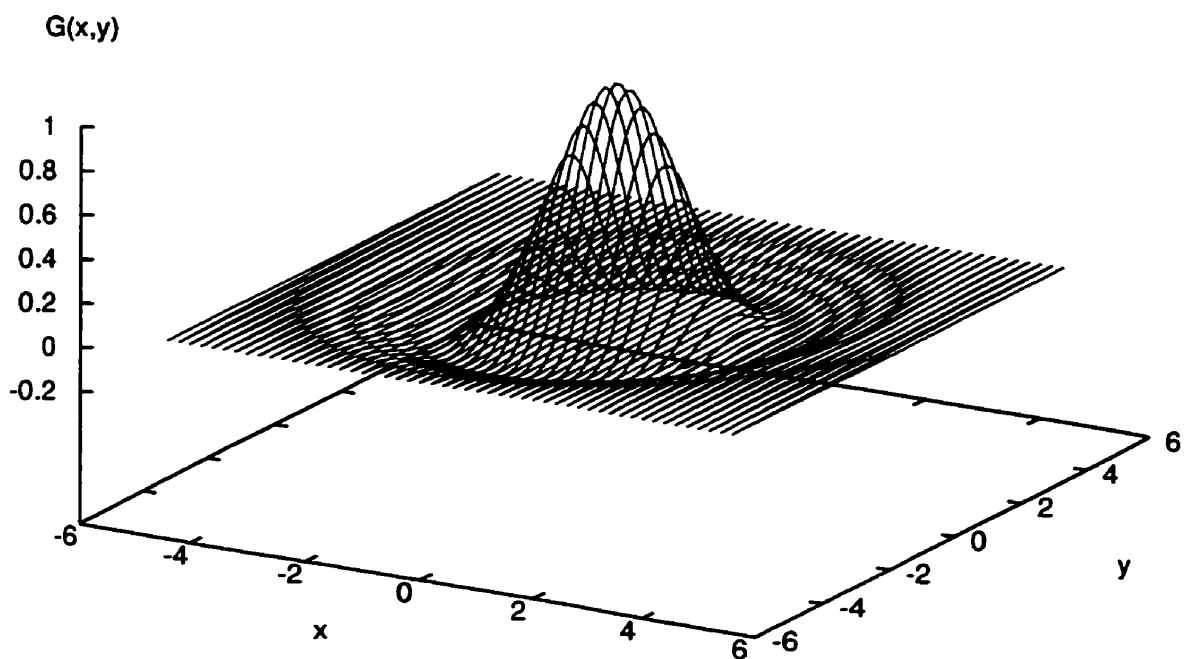


Figure 3.1: The Morlet wavelet function used by the filtering process

FLUXFIT. A new feature added, as a result of the GAUSSMAP tests and Chris Butenhoff's work on the pilot project, is that a mask file can be created. This mask file is used to mask out regions of extended emission or problem sources so that the maximum number of boxes are not filled with boxes that will be deleted. The mask file blocks out the problem regions so that they will not be looked at on further runs of FINDSRC (Higgs 1999a). The program FINDSRC has the following input parameters:

3.1.1 Initial Parameters

Are Negative sources to be found as well as positive ones: No

The mosaics from the Canadian Galactic Plane Survey will not have negative sources, they consist of positive sources on a positive background.

Is the beam shape to be defined in arc minutes: No

The beam shape will therefore have to be entered in grid units. An average value over the mosaic can be found by looking at the resolution cube file. For the purposes of FINDSRC an average beam shape can be used.

Enter the beam shape in grid units, including position angle:

The position angle should be in degrees.

Has the image been corrected for primary beam effects: No

Correcting for the primary beam results in a noise level that varies across the image. If this parameter request is answered yes, the primary pattern is requested so that

it can be removed before source finding takes place, yielding a working image with uniform noise.

Image to be corrected for inherent noise variation: Yes

The weight array can also be used to correct for noise distribution.

Is a mask file to be created or used: Yes

This new parameter allows the user to create a mask file that will mask out regions with bad sources (source boxes that had problems with base-level fitting.) This option was added to prevent running out of boxes before all the weaker sources were found. In the first run through FINDSRC the mask file must be created in order to use it in subsequent runs of the program.

Limiting Sigma: 1.5

FINDSRC is similar to a CLEAN algorithm in that it searches the map for all peaks and calculates the RMS amplitude. The twenty strongest peaks are then selected. For each of these twenty peaks, a beam shaped component convolved by the wavelet filter function is subtracted from the map using a loop gain of 0.5. The map is then searched for the next twenty strongest points. The sigma limit is not directly related to a limiting flux density of the sources. It is used to halt these search loops by one of the following methods: if a specified maximum number of sources are found (2000), if the RMS of the peaks does not decrease over three successive loops, or finally if no peaks greater than the RMS multiplied by the limiting Sigma are found (Higgs 1999a). For GAUSSMAP tests the limiting sigma used was 1.5. The default is 2.0, but lower values were able to detect more sources.

Box Clustering: 2.0 (default)

A list of the subtracted peaks from above is cumulatively compiled throughout the iterations. Once the algorithm is complete, FINDSRC finds all the peaks within 0.25 beam-widths of one another. These peaks are considered to be the same source and are added together, thus forming a list of major components. The major components are grouped together in source boxes. A single major component is initially centred in the source box. The major component list is then scanned for all components with peaks greater than 10% of the central component's peak lying within N number of beam-widths from that peak. N is specified by the box clustering parameter. Then the major source list is scanned again for all sources with peaks greater than 10% of the central component's peak lying within N number of beam widths from any peak in the source box. If needed the source box is enlarged. This process is repeated until three iterations have taken place, or fifteen components lie in the same source box, or the source box has reached a limiting size. The coordinates of the box, amplitude and position of the components within the box are what make up the BOX file. The default value is recommended except in crowded fields where smaller values may be better.

A filtered image file definition can then be created. This file is produced during the FINDSRC run but is not used in any other processing and therefore does not need to be kept.

Enlarge box size: 2.3

This is a new feature as a result of the GAUSSMAP tests. This parameter allows the user to increase the default box size by the above factor. The default box size is

for point sources; if the user expects slightly larger sources then this option is very helpful in the fitting process. The factor of 2.3 was used for the GAUSSMAP tests, though not quite so large a factor is expected for the mosaic data, as the sources are not so large.

Maximum number of boxes to be outputted: 2000

The default is 2000 and is recommended, as there are numerous sources in the mosaic and even boxes that fail base-level tests are still recorded in the box file.

**Sources thought to be very extended to be
marked as deleted: Yes and No**

For the purposes of the GAUSSMAP tests this parameter was answered no. This is because the GAUSSMAP sources were larger than what is expected for the mosaics. For initial runs of FINDSRC on the actual data, the parameter should be answered yes; this is to avoid including extended emission or considering multiple sources as an extended source. Once all the close double or triple sources have been removed properly (using FLUXFIT), the parameter can be changed to no, so that the slightly extended sources are included in the source lists.

**Are resolved sources to be clumped into one
(extended) component: Yes**

Sources that are slightly extended will usually be detected as a group of point source components. If this option is used these components will be clumped so that FLUXFIT will just fit an extended source to the data, rather than two or three components of the source.

Maximum separation for beam width clumping [0.800]: 1.00

It was found in testing the new version of FINDSRC and FLUXFIT that increasing the clumping factor to one substantially reduces the number of sources that were fit as two components when they were input as one.

Is base-level fitting to be checked for each box: Yes and No

FINDSRC can check the base-level fits of each source and delete the boxes that fail this fitting. The box will fail this test if it is too small or not in the proper position. If these boxes are not marked as deleted then FLUXFIT may have difficulties fitting them. As there are usually many boxes that fail this test, it is recommended to run FINDSRC with this parameter as Yes for the first few runs and on later runs switch it to No. The other alternative is to fit the sources by hand.

Twisted Linear or Twisted Quadratic base-level fitting: L

The twisted linear base-level fit is the default, and it is recommended. To understand the twisted linear and twisted quadratic surfaces, consider the arbitrary surface $z = S(X, Y)$. A twisted linear surface, "twisted plane", is a surface such that there exists a set of orthogonal X, Y axes that are rotated from the horizontal/vertical x, y axes, for which the intersection with z of any vertical plane parallel to the X or Y axes is linear. If the plane is parallel to the Y axis and is defined by $X = X_o$, the intersection will be defined by $S = A(X_o) + B(X_o) \times Y$, where A and B are constants that depend on X_o . A similar relationship holds for a plane parallel to the X axis. A twisted quadratic surface is defined similarly, except the intersection is quadratic rather than linear. $S = A(X_o) + B(X_o) \times Y + C(X_o) \times Y^2$ (Higgs 1999d).

Boxes failing base-level check to be marked as deleted: Yes

(Higgs 1999a).

3.2 Base-Level Fitting

The base-level fitting process described here is used only in FLUXFIT; FINDSRC has the option of checking if the boxes that it produces pass or fail a base-level check. In FLUXFIT the base-level is fit first and then the Gaussian. How the base-level is fit is as follows(Higgs 1999d):

Three pixels at each of the four corners of the box define the twisted plane under the box. The twisted plane has four parameters that are fit using the twelve pixel values. This is only a first approximation to the base-level. Next this approximation is subtracted from the data, giving an array of residuals. The array is then analysed by finding the centroid of the emission and the computed first and second moments around the centroid. This gives an estimate of the half power width of the Gaussian. A first guess of a best fitting Gaussian is then obtained. From here, the routine depends on whether or not a single or a multiple component Gaussian is to be fitted.

For single Gaussians, the amplitude of the proposed best fitting Gaussian is then compared to the RMS residual from the base-level (σ). If the amplitude exceeds 40σ , the source is treated as strong and fitted using the "RMS" method. For weak single sources the "Gaussian" method of fitting is used. Each method identifies different pixels that are flagged for a refinement of the base-level fitting. For strong sources, pixels where the residual is less than 3σ are flagged as pixels to be used in the next determination of a base-level. For weak sources, any pixel where the estimated

Gaussian would have a level below 1% of its peak is flagged. It should be noted that if the number of pixels found is anomalous, the routine might suggest a change of box size or abort the base-level determination. A new twisted linear or twisted quadratic base-level is fit to these points, a new sigma is recorded and a new array of residuals is found. The process of finding a new best fitting Gaussian is then repeated. After the first run, the limits for the two methods of base-level determination are reduced. For a strong source the value becomes 2σ and for weak sources it is 0.5% of the peak of the Gaussian used. After this run through of the procedure the resulting base-level is used as the final base-level, and the resulting residual array is used in fitting the Gaussian, which is done using a non-linear least square fitting routine.

3.3 FLUXFIT

The FLUXFIT program computes the flux densities by fitting Gaussians and correcting for the beam shape. This program analyses specific areas of the map, either predetermined by the program FINDSRC or entered manually within the FLUXFIT program. FLUXFIT removes the sources after the fitting process, thereby leaving the image clear of compact sources. A work file is created in which all the work is done, this file is essentially a copy of the file to be processed. The fitting process can be done in either astronomical coordinates or in pixel coordinates. Unlike FINDSRC, the beam shape at each position in the map needs to be determined using the "resolution cube" and not an average over the entire map. FLUXFIT also converts map units into Jy/beam or Kelvin, for the peak values of sources.

For a FLUXFIT run using the box file produced in FINDSRC, each box is anal-

used in the following way. Each box has its base-level fitted according to the method described in section 3.2. This is an iterative process that checks for centring and an adequate number of points to determine the base-level. During this fitting the peak data point is identified and its position output to the log file. As a starting point the true peak is estimated using quadratic interpolation. Also listed in the log file is the total positive flux density above the base-level, and the total flux density including both positive and negative deviation from the base-level. The user has the option of fitting up to three Gaussians in each of the boxes. The Gaussian fitting previously used the non-linear regression method due to Marquardt. The Marquardt method initially has the characteristics of the steepest descent method, but then takes on the characteristics of Newton's Method as the minimum sum of squared residuals is approached. Changes to this part of the program now allow the user to pick steepest descent method or Newton's method. The parameters and standard errors are output to a table of data including position, peak flux, integrated flux, position angle, and angular size of resolved sources. A resultant map with the fitted Gaussians subtracted is also produced.

3.3.1 Initial Parameters

Only simple Gaussians desired: No

If the simple Gaussian is chosen then no astronomical coordinates or related information is derived from the fitting process. These parameters are essential and need to be listed.

Beam parameters determined from a data cube: Yes

The beam parameters can be determined from the data cube, which allows for variation over the entire map, unlike an average value. For this reason, a better fit is expected if the beam information comes from the data cube. The beam parameter information is essential if units of flux, or source size corrected for the beam are desired.

Epoch of listed RA/DEC coordinates: 2000

The epoch of the listed data is 2000 and not the epoch of the observations.

Are sources to be corrected for primary beam effects: No

If this option is answered yes, there are two possibilities, either correct the whole map for primary beam attenuation (the work file is polar diagram corrected), or correct the analysis results for each selected region if the polar diagram. The first method gives better accuracy for flux densities especially for extended sources, whereas the second gives the best accuracy for positions of point sources. In both cases the half-power width of the primary beam must be given in arc-minutes. The primary beam correction can be based on a Gaussian primary beam or a cosine-power function. the default is the cosine-power function with an exponent of six, which matches the Synthesis Telescope pattern well. Neither of these options are used because the image is a mosaic of separate fields, and this correction is not appropriate.

Are source sizes to be corrected for effects of a ‘‘delay beam’’: No

The effect of the delay beam is a decrease in visibilities over the beam as a function of the field radius. This results from the fact that the phase delay added to correct for the geometric time delay is only exactly correct at the primary beam centre.

Each antenna has a 2.5° field of view, resulting in reduced visibilities from sources at further distances from the centre of the beam. As the delay beam is very large compared to the primary beam this question is answered no.

Selected initial search method emphasis [S]: S

This parameter was newly added after it was found that different computer architectures produced different results. The options are the steepest descent method (S) or Newton's method (N). Tests of these methods showed that the steepest descent method gives the most consistent results between PC and AIX architectures.

Are source box specifications to be read from a file: Yes and No

FLUXFIT can be run automatically using the box file produced in FINDSRC or manually when box information is entered by hand. Both methods are used during the processing of data, as some sources do not fit well with an automatic fitting process and need to be fit manually.

**Are sources to be removed from the work file as they
are analysed: Yes**

This produces a work file that is free of point sources leaving only the extended emission. This information is valuable to the rest of the survey consortium.

First and last sources in list to be analysed [all]:

Do you want a source table to be produced: Yes

The source table records the position and flux information from the FLUXFIT run, and is used in further analysis of the data. In the source table the positions are

recorded in RA and DEC; an additional galactic coordinate table must be produced for galactic coordinates to be recorded.

It is important to note that in the source table, flux densities and errors are always output in mJy. Normally the data are given to one decimal place except if one of the table flux values exceeds 99999.9 mJy, or if the error in flux reads more than 999.9 mJy. In these cases no decimal place will be given. Fluxes with values greater than 999999 Jy will be output as "*****" and errors exceeding 9.999 Jy will be output as "*****". If, however, a source has flux density lower than 999.99 mJy, then its value and its error will be output with two decimal places.

Other important points about the source table are that position angles of the source ellipses are true position angles, measured counter clock wise from the equatorial north pole of the map epoch. The source dimensions in angular units (arcseconds) refer to the projection plane for *lm* type coordinates; they are not necessarily the same units on the sky.

Enter Systematic errors to be incorporated

in the table RA [10.00E-2]: 0

Error in Dec [1.00]: 0

Error in flux (percent) [3.00]: 0

Is an additional flux error to be added quadratically: No

Source sizes in arcmin (M), or arcsec (S): S

Discrimination level (sigma) for extended sources [3.00]: default

The systematic errors for table output are errors in addition to noise effects on the Gaussian fitting. For example, there might be some uncertainty in the flux density

of the standard calibrator, known to some percentage. The real error is then the square root of the sum of the squares.

**Is an ASCII table of sources with Galactic and XY coordinates
also wanted: Yes**

This table is necessary to produce a source catalogue of the data that includes both RA/DEC and Galactic coordinates. This file also includes an estimate of signal-to-noise ratio calculated from the peak flux divided by the RMS noise.

Type of base-level (0 = twisted quadratic, 1 = twisted linear): 1

Are Gaussians constrained to the beam shape: No

This option is usually only appropriate for unresolved sources.

Are Gaussians constrained to be no smaller than the beam shape: No

FLUXFIT can either fit the Gaussian width of sources or the excess width beyond the instrumental resolution. In the GAUSSMAP tests the instrumental resolution was unknown, so the fitting was not constrained. For the CGPS data, the instrumental resolution is fixed. Some benefit can be gained by constraining the fitted Gaussians to be no "sharper" than the resolution - it limits the fitting of noise spikes. The error analysis of these fits might break down with this constraint however, as was seen in Butenhoff (1997). In this mode, rather than fitting the major and minor halfwidths of the Gaussian, the program fits E where the width of the Gaussian is given by $W = 0.95R \times (1 + E^2)$, and R is the resolution width. For large errors, the transferring of error from E to W breaks down (Higgs 1999d).

**Are fittings in which more than 10% of the fitted Gaussian
‘‘volume’’ lies outside the analysis box to be rejected: Yes**

This is a new parameter that prevents the source from migrating out of the analysis box during the fitting process, thereby producing a better fit.

Are derived standard errors in Gaussian parameters to be used: No

If this option is answered no then the standard errors can be deduced from the non-linear confidence intervals (95%) estimated for the parameters. This means that the errors will be limited in magnitude to the magnitude of the parameter to which they apply, (except to angle errors which will be limited to 180 degrees). If this option is answered yes then the standard errors given by the fitting routine can be used.

Is the RMS to be estimated from a given patch of map: No

The RMS noise here refers to a pixel, so if the map is over-sampled, the pixels will not have independent sky noise, therefore the true sky noise will not be correctly represented. When the above parameter is answered no, the RMS noise level is derived from deviations from the fitted base-level, where the Gaussian source contribution is negligible. This value is only used in the “ χ^2 ” analysis of the goodness of fit of Gaussians.

3.3.2 Log file

The log file from the FLUXFIT program contains a best estimate of the Gaussian parameters along with their estimated standard errors. An integrated flux density may be derived from the fitted amplitude, and is also included in the log file. An

estimation of the χ^2 statistic based on the variance of the fit and the estimated RMS for a single map point, and the theoretical value for a 95% probability of a good fit are also listed. The total flux in the Gaussian is shown with an estimate of its error. If more than one Gaussian component is fit, the flux and error estimate for each component are listed in parentheses. Finally, for each Gaussian component, an estimate of the corresponding intrinsic source size is given (Higgs 1999b).

3.4 Summary of previously detected fitting problems

During the CGPS pilot project (Butenhoff 1997) several problems with the source detection and fitting software were found. Two problems with FINDSRC were noticed. The first arises from the source box array being filled with previously detected “bad” boxes. Boxes that were found in an earlier run of FINDSRC and deleted due to failed base-level checks are found on later passes of the FINDSRC program. Secondly, crowding in 408MHz due to poorer resolution, caused problems in identifying individual sources.

FLUXFIT was found to have a number of problems as well.

- A problem with base-level fitting. In the case of strong sources, the faint wings of the Gaussian are interpreted as the base-level, as the source is much larger than the background noise. Therefore, when sources are subtracted a percentage of the source is left behind.
- Spurious sources are either artefacts of the Fourier Transform, extended emission or residuals of strong sources. these are fit as individual sources, but are not true compact sources.

- Slightly resolved sources can be fit with two or more Gaussian components when only a single component is required. This causes two or three sources to have lower flux density than what would be expected for just one source.
- A problem with bifurcation in the distribution of integrated-to-peak flux density ratio of less than 1.1 was also noted. This is a problem because slightly resolved sources and unresolved sources will have different integrated fluxes, in that sources with integrated-to-peak flux ratios less than 1.1 will have their integrated flux set to equal their peak flux.

3.5 GAUSSMAP

The program GAUSSMAP was used to ensure that the detection and fitting software from DRAO was working correctly prior to running it on the actual data and to fix any problems that appeared. Chris Butenhoff's work on the Pilot Project of the Canadian Galactic Plane Survey identified the problems described above. These problems as well as additional ones found during the test needed to be fixed prior to work being done on the CGPS data.

GAUSSMAP is a part of the DRAO software package. Its purpose is to create artificial 2D Gaussian sources and add them to an already existing map, or create a new map. These sources can have a random distribution of sizes and orientations, with random or power-law-like amplitude distributions. This software was used to create images with artificial Gaussian sources to test FINDSRC and FLUXFIT.

3.6 How GAUSSMAP image was created

The GAUSSMAP test map was made from a residual map of the mosaic MV1. A residual map is what remains after FINDSRC and FLUXFIT have been run. If the source subtraction worked well, the residual map should be clear of compact sources and only extended emission should remain. The residual map for the test was made using FINDSRC and FLUXFIT with no regard for correct subtraction. Multiple runs were required to ensure that most of the source emission was removed; however, some still remained. For instance, the large variable near the centre of the mosaic did not subtract properly and has therefore left a signal. There were some sources that were not found and are therefore still present in the map. An image of the test map prior to the adding of Gaussians is shown in Figure 3.2. Several compact sources remain. However, the map provides a realistic criterion for testing. It should be noted that the program checks for overlapping sources; if sources are separated by less than their average FWHM, a listing of these overlapping sources is compiled and printed at the end of the log file (Higgs 1999c).

3.6.1 Initial Parameters

For the purposes of this thesis the following options were entered in the GAUSSMAP program, to produce a test map for the FINDSRC and FLUXFIT programs. The positions, sizes and amplitudes of the GAUSSMAP test sources were input using the default random seed, therefore, all other runs of GAUSSMAP would produce identical maps.

Is Gaussian noise to be added: No

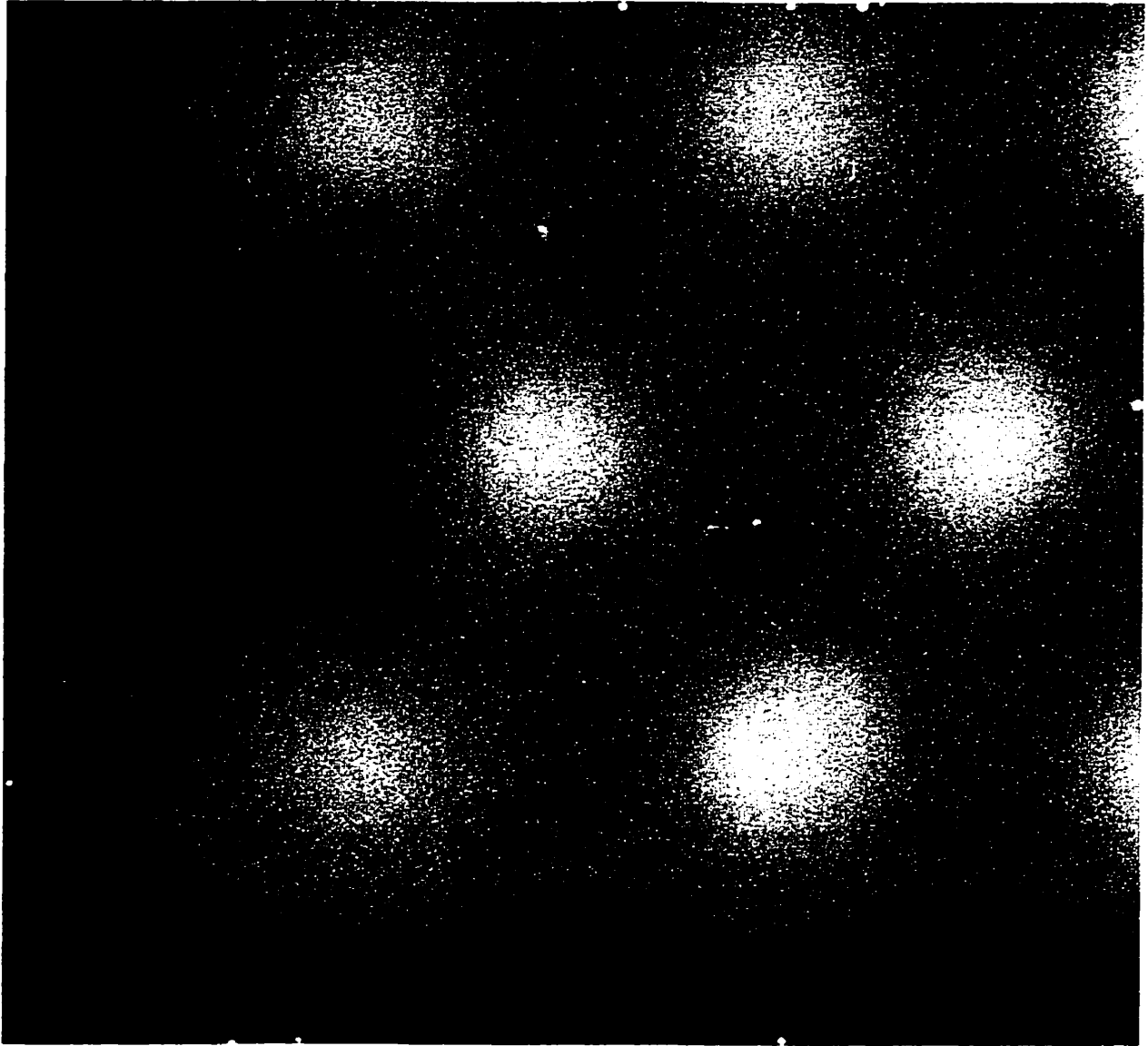


Figure 3.2: Original mosaic MV1 with sources removed

Gaussians defined by the user: No

A maximum of 500 sources with same or different amplitudes can be added. A detailed list of the random Gaussians is then listed in the log file. If the amplitudes are to be different, a maximum amplitude is required. The distribution can be either uniform or according to a power-law distribution of the form $dN = S^E dS$. Where dN is the number of sources having flux densities between S and $S + dS$, and E is the given exponential. If a power-law is chosen, one Gaussian source will have maximum amplitude and the number of sources will then increase as the amplitude decreases, according to the above differential equation. The number of sub-ranges are determined by the user, wherein the amplitudes are distributed uniformly (Higgs 1999c).

All Gaussians have the same width and orientation: No

A maximum major width (Full Width at Half Maximum) and a minimum minor width (FWHM) is needed for the random distribution, and the sources will vary within that range. The orientation can also be determined randomly or set explicitly. If random, the program chooses for each Gaussian a value between 0 and 360°. For the purposes of the test, the sources are allowed to have any orientation, but their widths have been restricted to a maximum major half width of 5.0 grid units and a minimum minor half width of 3.34. These numbers come from the average beam shape over the mosaic which has size: major half width 3.33 grid units, minor half width of 2.74 grid units, and position angle of 53.86°. The input minor half width must be larger than the beam or there is a division by zero error in the fitting software and a fit can not be found. The convolution of two Gaussians gives a third but wider

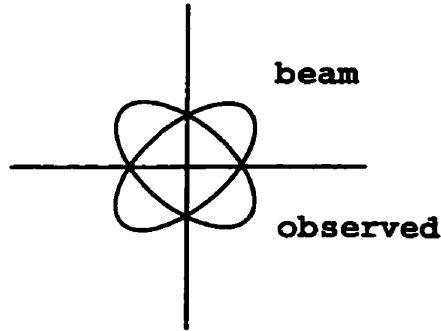


Figure 3.3: Depiction of unphysical situation, beam outside the range of the source Gaussian. In one dimension the deconvolution can be expressed simply as

$$\phi_s = \sqrt{\phi_o^2 - \phi_b^2}, \quad (3.2)$$

where ϕ_o is the observed FWHM, ϕ_s is the source FWHM, and ϕ_b is the beam FWHM. So if the observed ϕ_o is less than the beam ϕ_b an imaginary number is computed and the result is unphysical. Therefore the source must be larger than the beam on input into GAUSSMAP. If, due to orientation angle, the beam ever goes beyond the source size the situation becomes unphysical (Figure 3.3). This will not be a problem with the actual data.

Gaussians were added to the source removed MV1 map using GAUSSMAP, according to the above prescription. Using FINDSRC and FLUXFIT, the sources were fit and removed. A Log file of each of these processes was kept so that a comparison between the input and output data could be made. With the output from FINDSRC and FLUXFIT, C programs were written to compare the data.

3.7 Results of initial GAUSSMAP test

Running FINDSRC and FLUXFIT on Figure 3.4 produced a residual, source subtracted map (Figure 3.5) that had source emission left behind, and oversubtraction of a number of sources.

To understand this result, the log files were analysed to compare the input and output data. A comparison graph of the FLUXFIT peak amplitude divided by the GAUSSMAP peak amplitude versus the FLUXFIT peak amplitude is shown in figure 3.6. The line on the graph indicates unity, and is not a regression line. The cluster of points that lie a large distance from one are close doubles or extended sources. In the case of the close doubles, the sources were input as two individual sources with particular flux, and FLUXFIT attempted to fit them as one slightly extended source. The case of the extended sources is the opposite. The source was input as one source and FLUXFIT fit it as two or more. For the remaining sources the mean ratio is 1.011 and standard deviation of 0.113. A regression was performed giving a slope of 2.39×10^{-6} and y-intercept of 1.011. In this graph it can be seen that the points fall somewhat above one, indicating that the determined peak flux is about 1% higher than the input value.

A comparison of the angular size was performed using the major and minor FWHM. Figure 3.7 shows a graph of the division of FLUXFIT major halfwidth by GAUSSMAP major halfwidth versus FLUXFIT amplitude. An underestimate of the major halfwidth is easily visible as the sources are well below the line at one. Again this is not a regression line. The graph has a mean of 0.987 with standard deviation of 0.018. The regression line produced a slope of -7.23×10^{-6} with y-intercept



Figure 3.4: GAUSSMAP image used to test the program FINDSRC and FLUXFIT. White sources are 2D Gaussians inserted into the image with random orientations.

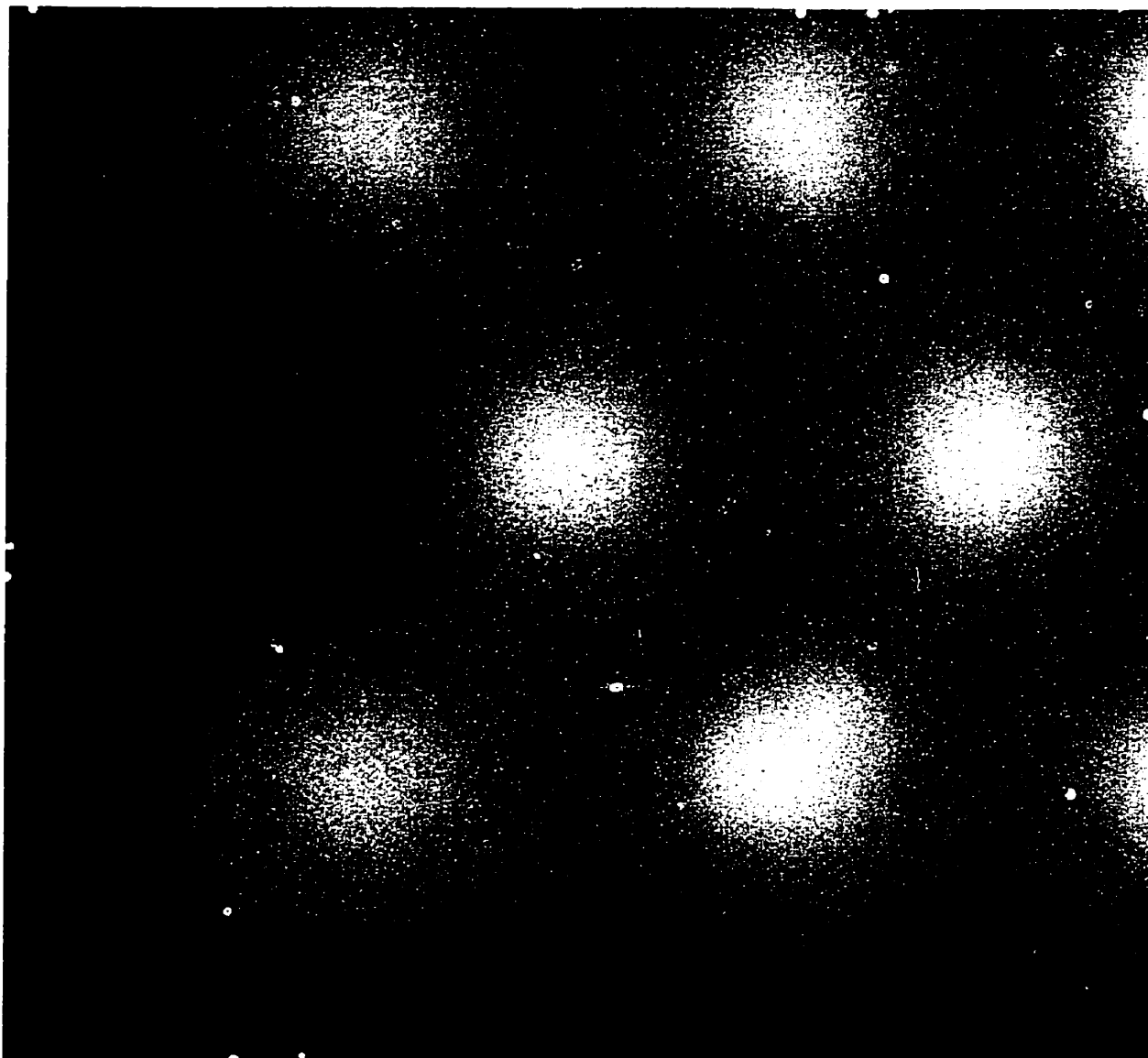


Figure 3.5: Work file from original GAUSSMAP test. This image shows the residual of the subtracted sources detected by FINDSRC and fit by FLUXFIT.

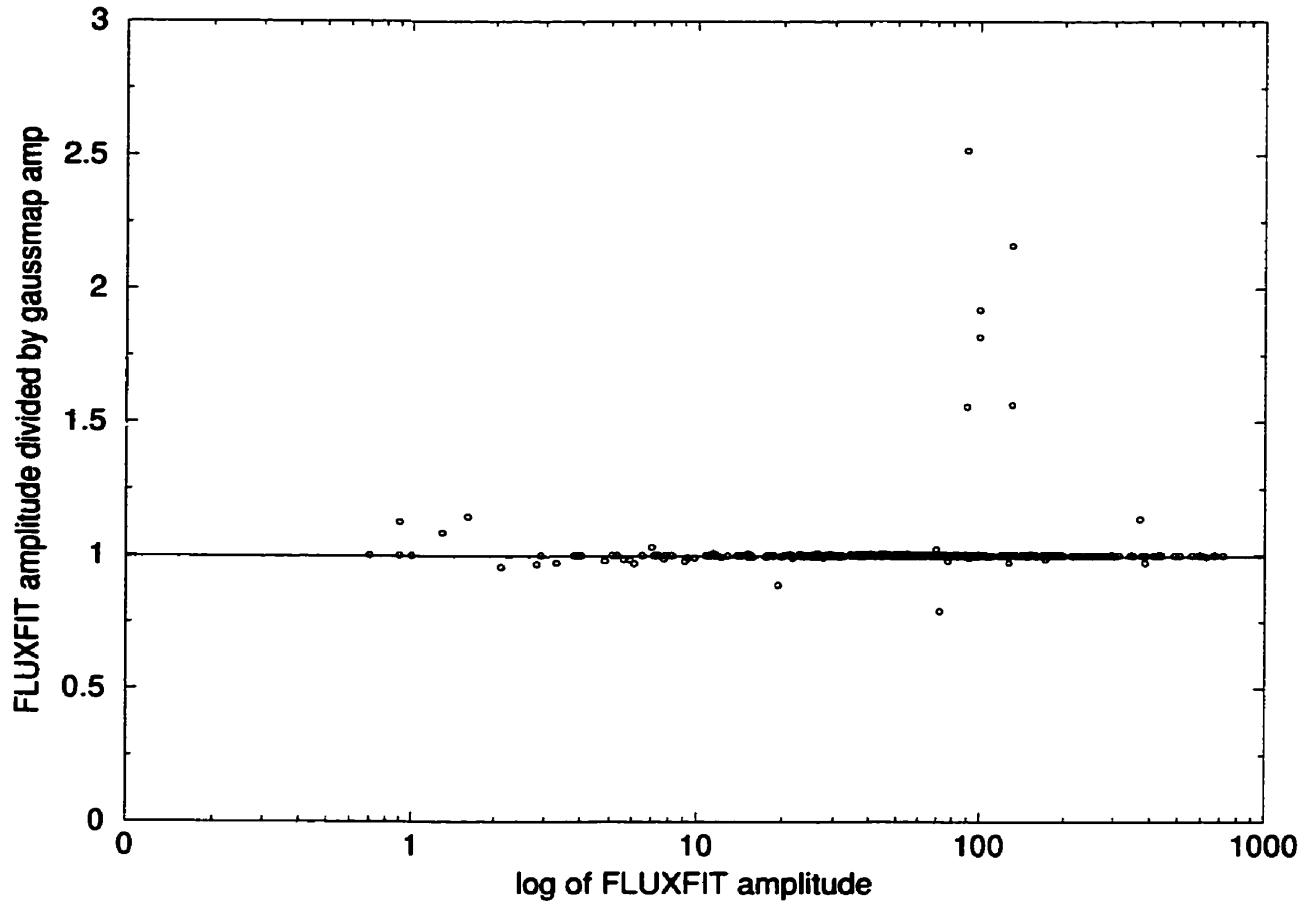


Figure 3.6: Graph of input peak amplitude divided by output peak amplitude versus output peak amplitude, old version

0.987, well below the value of one. This graph shows that there is a systematic error in the determination of the major halfwidths. A similar error is seen with the minor halfwidths (Figure 3.8). The mean of the minor halfwidth ratio is 0.985 with standard deviation of 0.015. The slope of the regression line is 1.39×10^{-5} with y-intercept of 0.983, again visibly below the value of one.

3.8 How Problems were fixed

Once the testing of FINDSRC and FLUXFIT was done using GAUSSMAP, a list of the problems was made – including the problems found by Butenhoff (1997) and the difficulties with angular size fitting. A trip to the DRAO was needed so that work with the author of the software could be more productive. The problems and possible solutions were discussed. Some of the solutions were implemented and further tests were run, and this process was repeated until a satisfactory result was obtained. Below are the results of this trip, indicating what changes were made to the programs.

The problem concerning invalid boxes filling up the maximum 2000 boxes, thereby not allowing valid sources to be found, was dealt with by introducing a mask file. This mask file can be made on the first run through of FINDSRC, and used on additional runs. The mask file is a collection of invalid boxes and their sizes and locations. FINDSRC will not look at the masked out regions on a second pass through the program. In the case of the large variable in MV1 it was found to be an invalid box so it was masked out. FLUXFIT can be run so that the sources are entered manually; this can be used to remove those masked out sources. It may, however,

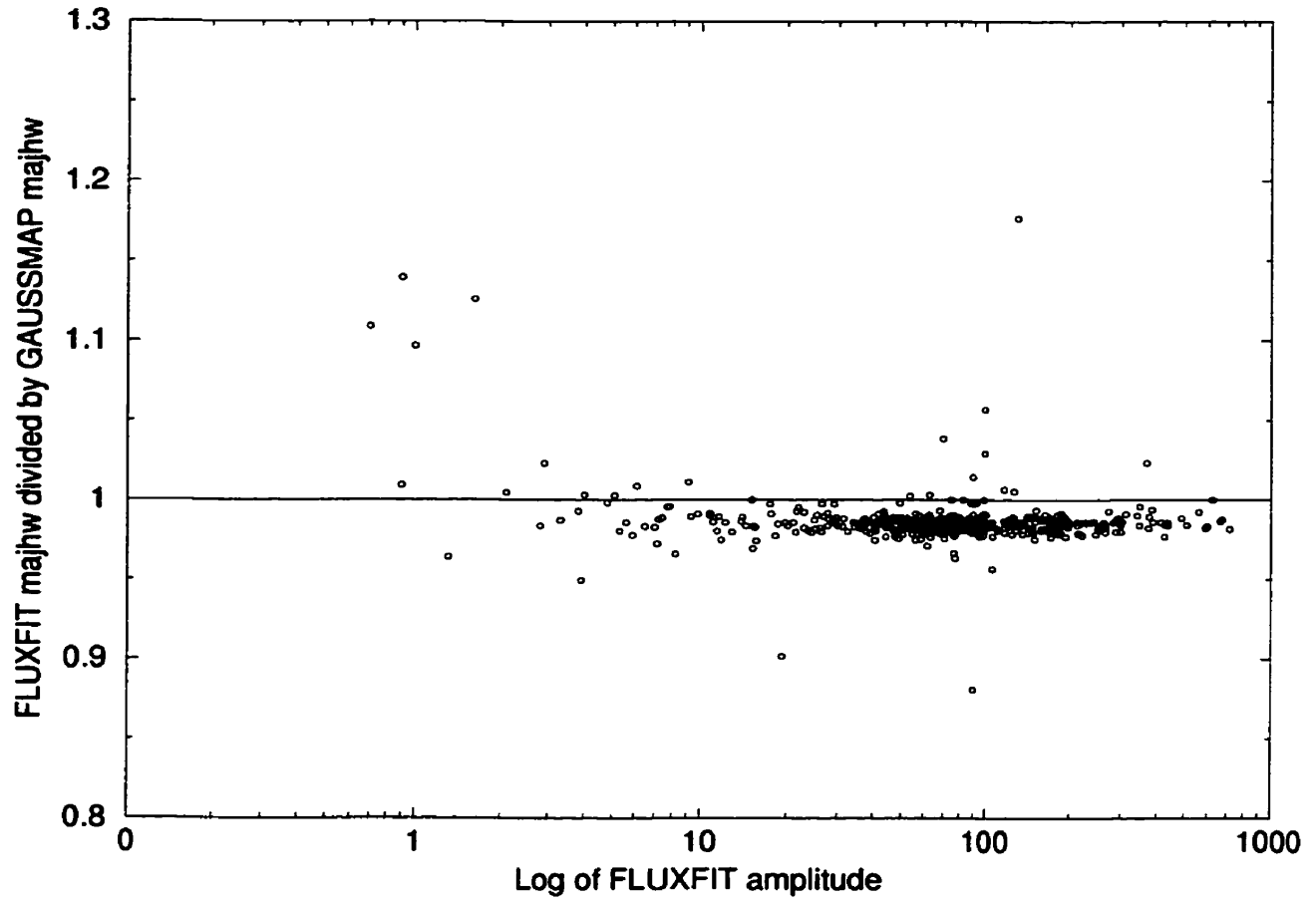


Figure 3.7: Graph of ratio (output major / input major) vs log of FLUXFIT amplitude, old version

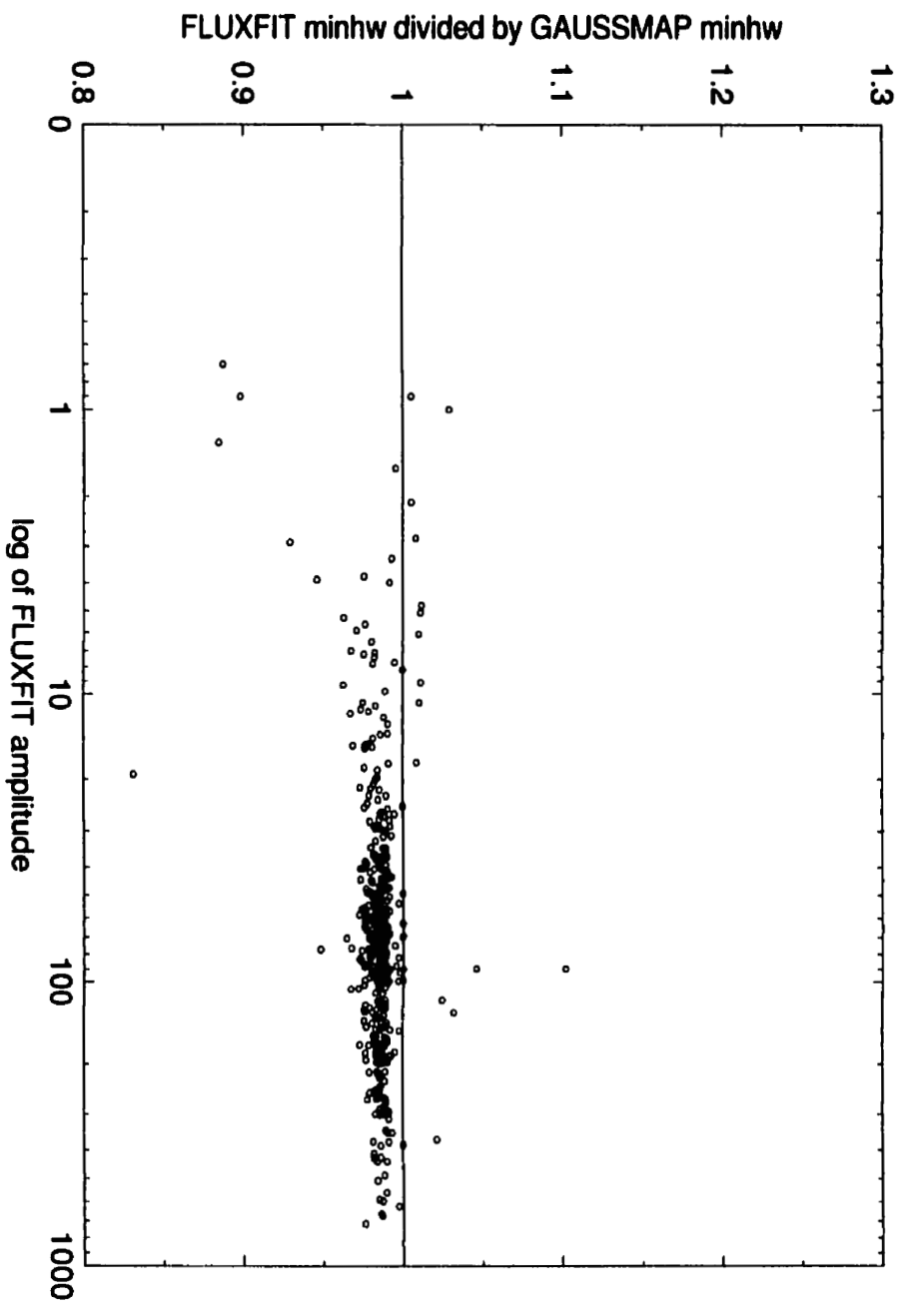


Figure 3.8: Graph of ratio (output minor / input minor) vs log of FLUXFIT amplitude, old version

need to be done first in the case of bright sources. For this reason a preview pass of FINDSRC and FLUXFIT is needed in order to find the problem sources. Once these problem sources have been found they are removed manually and then the automatic run of FINDSRC and FLUXFIT can be done.

The FINDSRC program was altered so that the division by the noise map could be done in the program prior to looking for sources, however, no new image is made. As a result, when looking at FLUXFIT images no noise pattern, caused by the short spacings, is seen like the one in the first GAUSSMAP test image.

A problem of reading the beam array resolution cube in FLUXFIT was a result of the parameters entered into the program SUPERTILE prior to my receiving of the data. The definition file of the resolution cube needs to be altered before it can be used in FLUXFIT. The parameters that need to be changed are: units – they should be undefined (option 0). “Auxiliary astronomical parameters wanted” should be answered no. With these two changes, the resolution cube can be used in the FLUXFIT program.

Underestimation of the true angular size was partially a result of errors in converting the position angle to radians rather than entering the angle in degrees. There were however some problems with the code as well. A previously undetected bug in the reduced precision fitting was found. There was a problem fitting simple sources (only one source in a box), so that the program was better at fitting sources if there were multiple sources in a box (complex fitting). This has since been changed.

Base-level fitting was considered to be a possible cause of the problem concerning angular size. The base-level is fit according to a twisted linear plane. The program originally had a base-level fitting routine that found a base-level of 3% of the Gaus-

sian. A first guess Gaussian is fit to the data then a base-level is chosen to be at 3% of this Gaussian. If the data is noisy, as is the case with the CGPS data, the 3% level is assumed to be in the noise, thereby being a suitable base-level. If however, the source is strong, 3% might not be in the noise, causing the base-level to be higher and the angular size underestimated. This base-level was lowered to 2% of the peak which gave a better fit to the angular size of strong sources.

Spurious sources can be a result of either of two things. The first was found while testing FLUXFIT using GAUSSMAP. GAUSSMAP can put two sources on top of each other or very nearly so, FLUXFIT has difficulty fitting these sources and it usually results in a black negative line between the two sources and a black tip at each of the edges (Figure 3.9). Sources that result in this pattern have two sources that are really close together and need to be fitted manually. Another possibility is that the box is moved slightly and that one of the multiple sources has been moved out of the box. A check has now been set to see if a source has moved out of the box. If so the box is adjusted again and fitting is retried (Higgs 1999b).

3.8.1 Other Enhancements of FINDSRC and FLUXFIT

Galactic coordinates will be needed in the final source catalogue. They were not previously recorded in the source table file, although they were calculated in the log file. The source table file is needed for other programs and therefore has a fixed format. So, another ASCII table output file has now been added that contains the source number, size (major and minor axes) with uncertainty, grid position, integrated flux, peak flux, position angle, galactic coordinates with uncertainty and signal-to-noise ratio. This new file can then be matched with data from the source

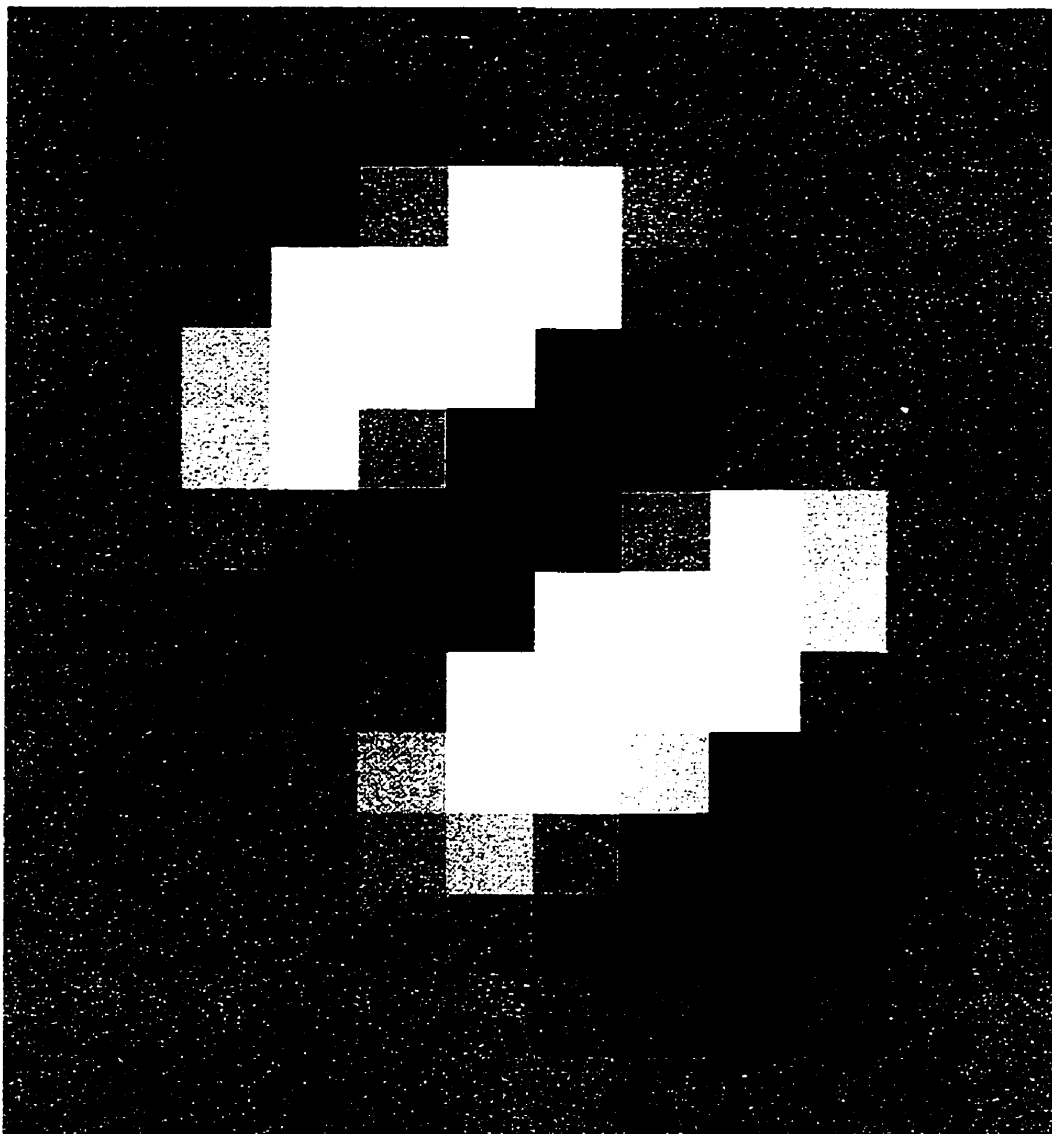


Figure 3.9: This pattern is the residual of a near double source, resulting from an automatic fit using FINDSRC and FLUXFIT. This pattern is typical of near double sources, therefore manual fitting is required for these objects.

table file to produce the source catalogue.

A note for running FLUXFIT manually: if entering parameters for double or triple sources, relative amplitude will have to be entered as well as the coordinates of the sources. Relative amplitudes require that the stronger component must be given a value of 1.0 and the weaker component something smaller. The program is not expecting an estimate of the peak amplitudes.

After these changes were made, a final run through of the GAUSSMAP test was run, to see if all the problems had been sorted out. These test results are given below.

3.9 Revised FINDSRC and FLUXFIT run

As previously mentioned, GAUSSMAP was run using the default random seed so that the sources in the revised test are identical to the sources in the original test. The difference in the images results from the change made to FINDSRC in that the noise map division is done internally so that the noise pattern is no longer present in the new image.

The new version of FINDSRC and FLUXFIT produced a work map that was clean of sources except for the ones on the edge of the image (Figure 3.10). There are some remaining signals present in this image, however, they are the actual sources of the MV1 mosaic prior to adding the test Gaussians (compare to Fig 3.2). From this image it is clear that the software is subtracting sources better than previous performances.

A comparison of the FLUXFIT peak amplitude divided by the GAUSSMAP peak

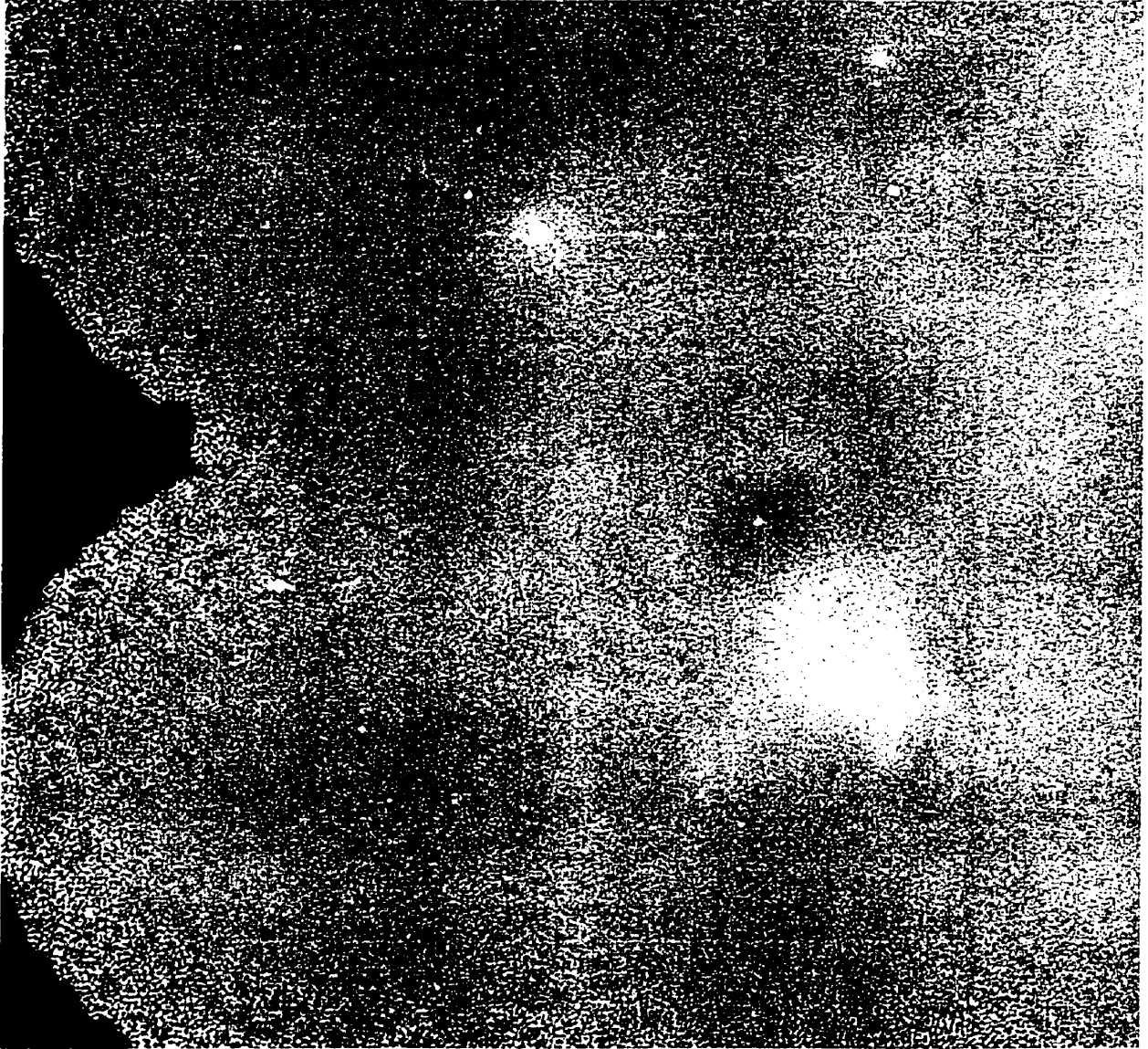


Figure 3.10: Work file from new GAUSSMAP test

amplitude versus the FLUXFIT peak amplitude was made (Figure 3.11). If a source is input as a slightly extended source and is fit as two or three sources, the flux will be lower on the components than on the single source. After raising the clumping factor from 0.8 to 1.0 there were only the few sources remaining below and above the line, whereas initially there were more than 50. Scatter is seen in this graph as well as the old version graph. The new version had a mean of 1.004 and standard deviation of 0.072, indicating an improved fit to peak amplitude compared to the old version. The new version is much closer to the expected value of one, with a slope of 2.97×10^{-5} and y-intercept of 0.999.

The graph of the division of FLUXFIT major halfwidth by GAUSSMAP major halfwidth versus FLUXFIT amplitude was plotted (Figure 3.12). The new version shows a graph that is much closer to the expected value of one. The mean is 1.002 with standard deviation of 0.022 indicating slightly more scatter than the old version, but the regression line is much closer to 1 with a y-intercept of 1.004. The new version has removed the systematic error in angular size fitting. This is confirmed by comparing the minor halfwidths. The division of output minor halfwidth by input minor halfwidth versus FLUXFIT amplitude graph (Figure 3.13) shows a much better fit, with mean of 0.999 and standard deviation of 0.019. Slightly higher scatter is seen in the new version but the y-intercept is 0.998, again much closer to one.

Another improvement in the new version is that more sources were removed automatically. In the new version 41 sources were removed by hand, of these 16 were single sources, 21 were double sources, and 4 were triple sources. Out of the 500 input sources, 428 were found automatically. This is a 86% automatic removal rate. In the old version this rate was less than 80%.

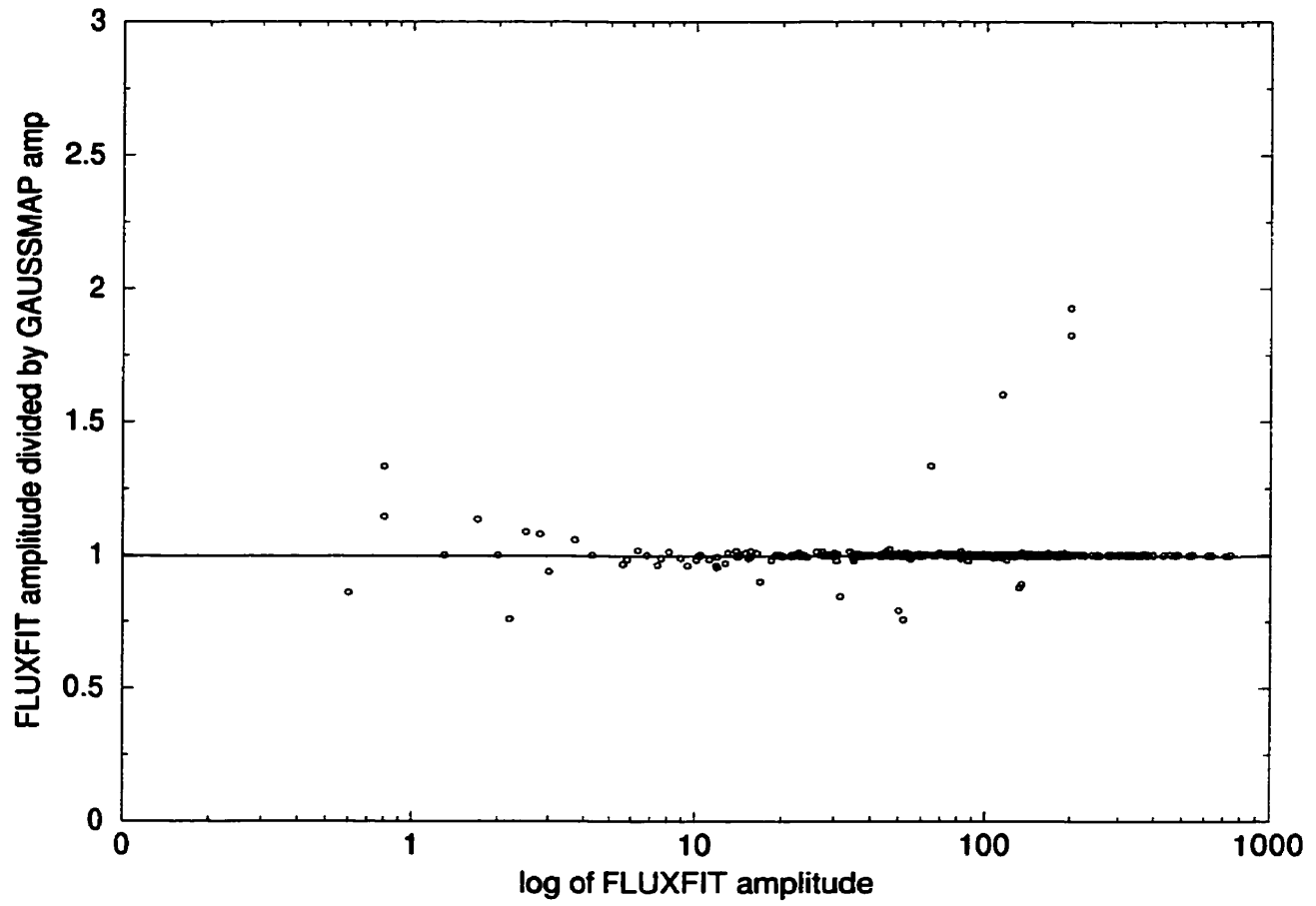


Figure 3.11: Peak amplitude ratio vs FLUXFIT peak amplitude graph, new version.
To be compared with Fig:3.6

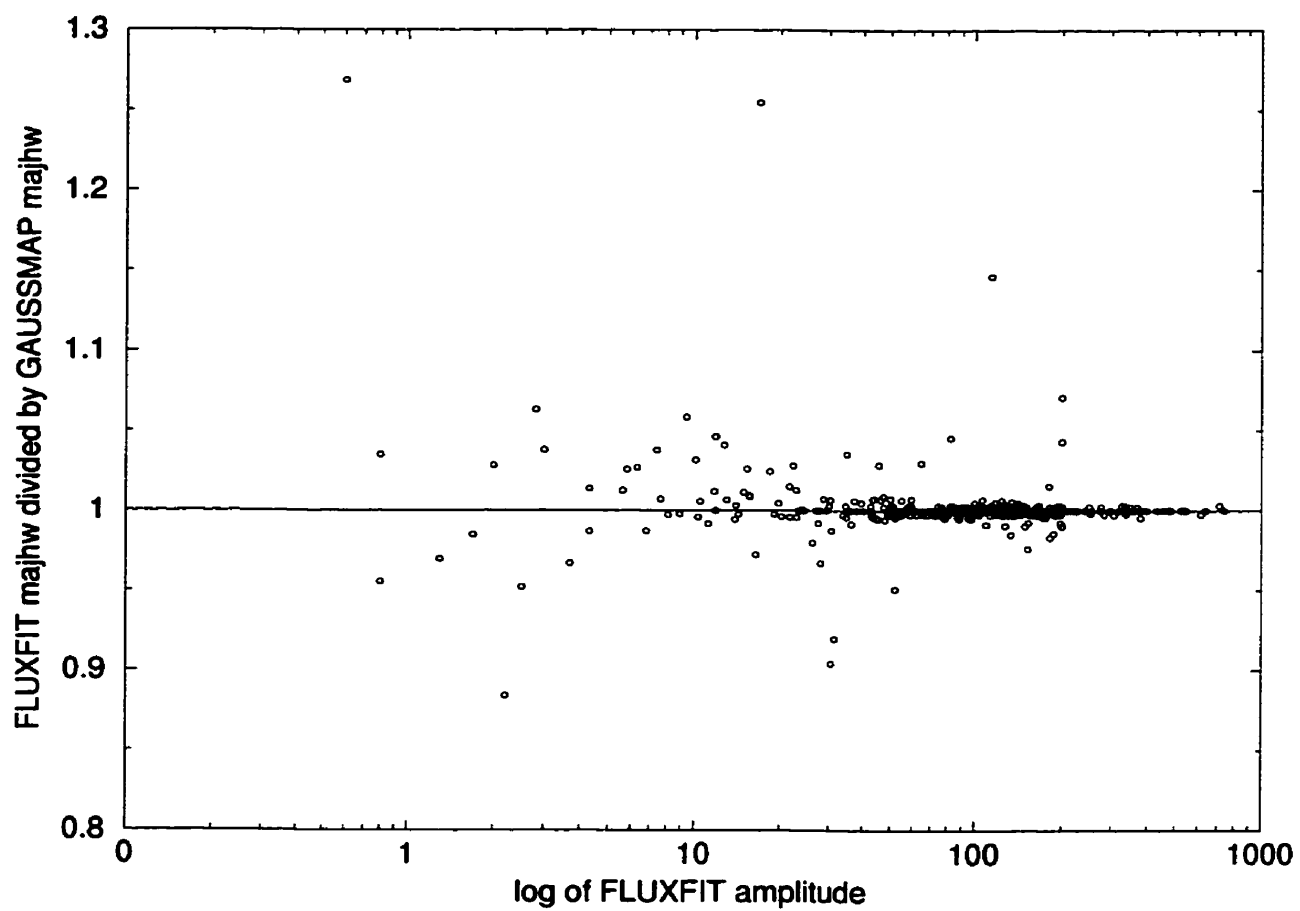


Figure 3.12: Graph of ratio (output major / input major) vs log of FLUXFIT amplitude, new version. To be compared with Fig:3.7

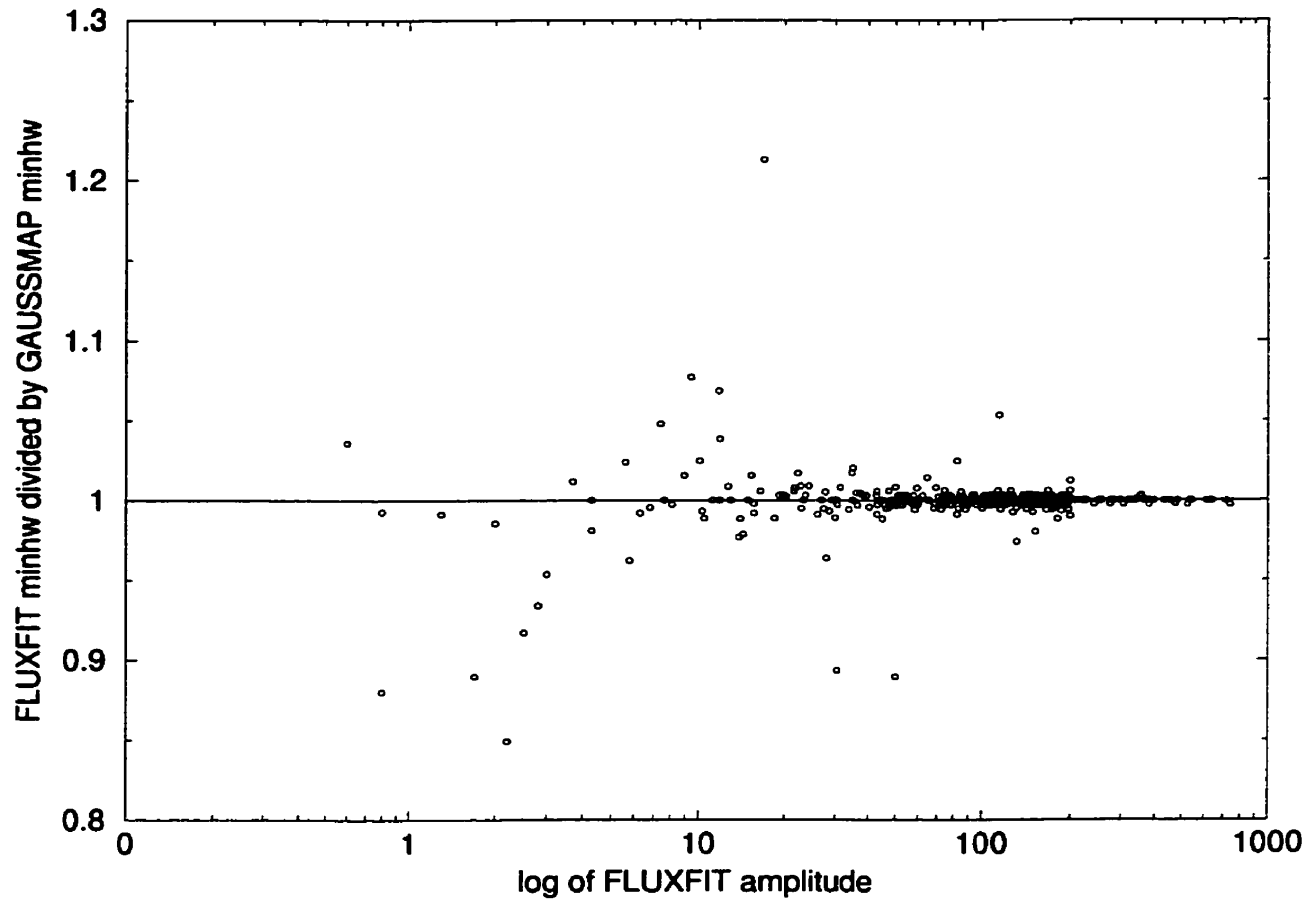


Figure 3.13: Graph of ratio (output minor / input minor) vs log of FLUXFIT amplitude, new version. To be compared with Fig:3.8

These graphic comparisons show that the automatic source fitting programs are working much better after the above changes were made. Peak fluxes are matched very well with the input values, except for when two sources are too close together. This error can be corrected with manual fitting of the few cases. Finally, the major and minor halfwidths are fit much more accurately, resulting in a more accurate integrated flux. These test results allow for confidence in the output from the source fitting programs.

3.10 My programs

For the testing of the FINDSRC and FLUXFIT software, I wrote four programs designed to take information out of the log files (since the log files contain peak flux which was recorded by the GAUSSMAP log file for the input data) and compare them with the input data. The first program PARSE takes out the fitted Gaussian information and creates an ASCII table of all the sources. Any source that was found to have two or three components is treated as two or three separate sources. This table is then matched with the input data using the program SEARCH. SEARCH looks at the parsed output from the FLUXFIT log file and matches it with the GAUSSMAP log according to xy grid positions. A matched table is produced to compare the amplitudes, angular sizes, and position angles. Next a program called DIVISION is used to divide the FLUXFIT amplitude by the GAUSSMAP amplitude and print all three to an ASCII table. This table was used to produce the comparison graphs above. Finally the program HALFWIDTH is run on the matched table file to produce another table consisting of major and minor halfwidths, and divisions of

FLUXFIT major and minor halfwidths by GAUSSMAP major and minor halfwidths. This table was also used to produce the graphs above.

3.11 The CGPS source catalogue

To extract a catalogue of radio sources from the mosaics MV1, MV2, MW1, and MW2, other programs had to be written. First, a program to read the data from the source and galactic coordinate tables, and not the log files, was written. The problem with the table files is that they have varying formats. If the source that is being entered has components, then first a row containing data and the word "centroid" is entered. This information pertains to the two or three components of the source as a group and not the individual sources. For this reason these rows needed to be removed from the table. The program CENTROID was used to change the table into something with constant format and remove the rows containing the word "centroid".

Next a program PRUNE is run on CENTROID's output. This program removes all the alpha characters resulting from multiple component source numbers listed as 1A, 1B or 1C. Also the program ensures that all lines have the same length of characters. In this case the unresolved sources have source sizes of 0 added to the rows so that the format is constant for the production of a source catalogue. Lastly a program SOURCECAT is run. This program combines data from the galactic and source table files after the above alterations have been made. The source data are combined source by source according to array location. Caution must be taken that both files are checked for non alpha-numeric characters: "*" characters might be

present for a source in one table but not in the other – causing a mismatch of data.

The source catalogue produced contains the position of the source in both RA/DEC and galactic coordinates, peak flux, integrated flux, angular size, position angle, all with uncertainties, signal-to-noise ratio and which mosaic the source is located in. A catalogue of sources including these parameters was produced for each of the mosaics. Sources with signal-to-noise ratios of less than 5 were removed from these catalogues. The catalogues were then combined into one, and repeated sources caused by mosaic overlap were removed. This combined area of the four mosaics, a 9 degree by 9 degree image, contains 5498 compact sources. An image of the combined mosaic is shown in Figure 3.14. Figure 3.15 is the source subtracted MVW mosaic. Once the catalogue is produced, the search for variable sources can take place.

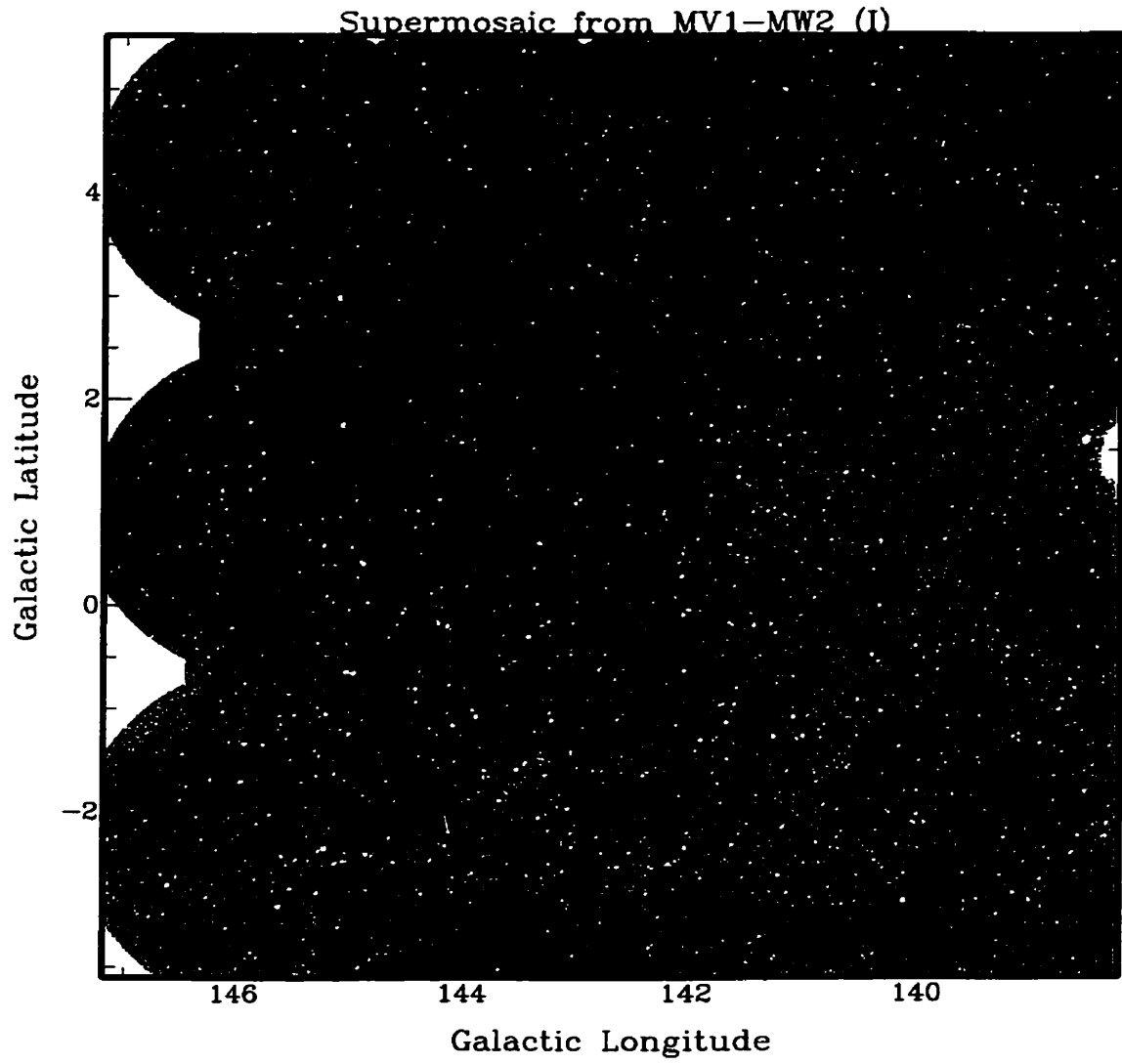


Figure 3.14: Compilation of MV and MW mosaics

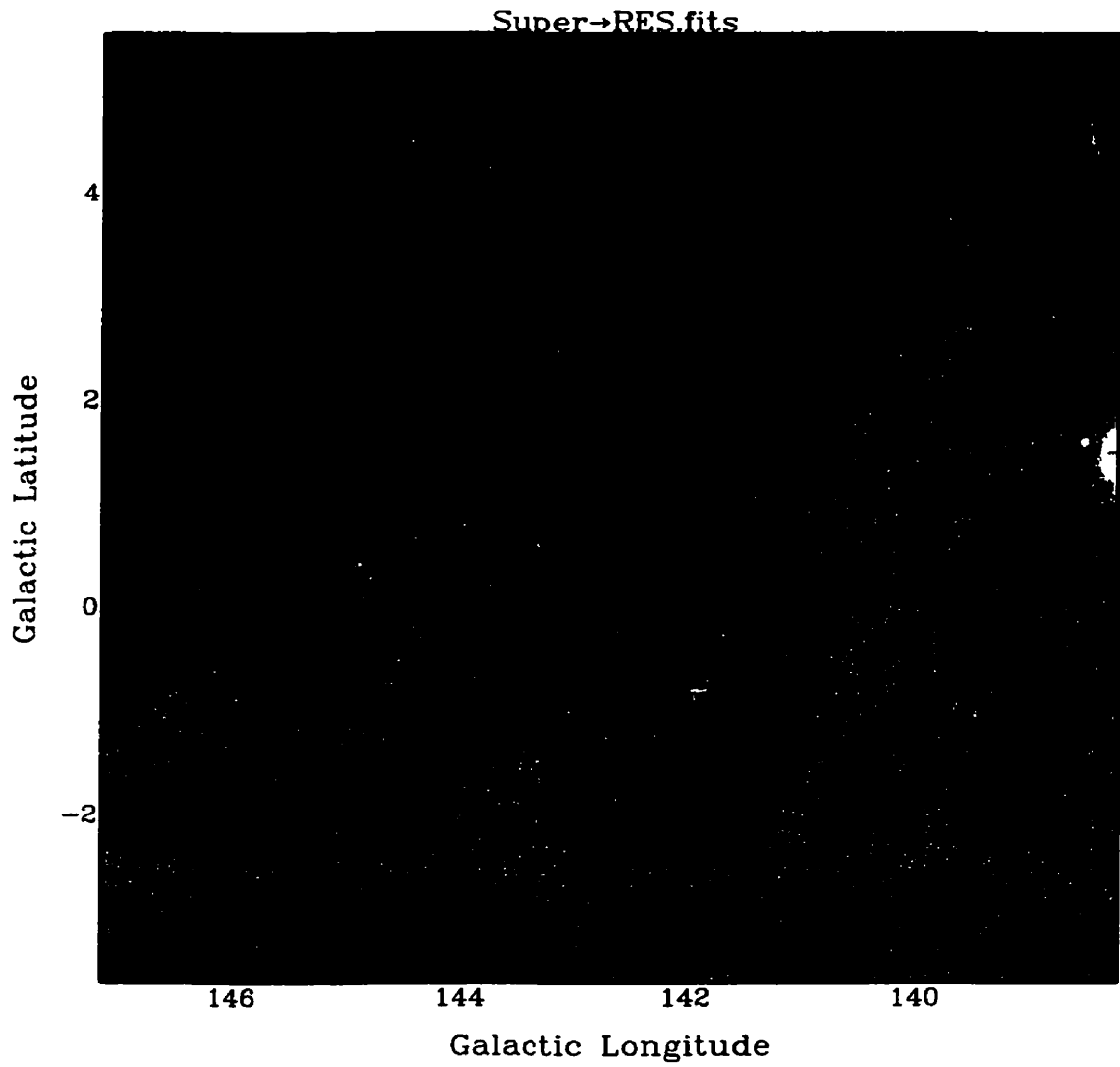


Figure 3.15: MVW mosaic after the removal of 5498 sources.

Chapter 4

Variable Search and Spectral Index Measurements

Variable sources are interesting to the astrophysical community because they give insight into the nature of the objects in the sky. This variable study considers variability, over a few years, in the galactic plane at 1.4 GHz, and involves comparing the CGPS integrated flux densities with the NRAO VLA Sky Survey (NVSS) integrated flux densities.

4.1 The NVSS Survey

The NRAO VLA Sky Survey is a survey covering 10.3 sr of the sky, north of J2000 declination -40° , at 1.4 GHz. The survey was done, using the compact D and DnC configuration of the Very Large Array, between September 1993 and October 1996. The aim of this survey was to provide the astronomical community with access to a large archive of radio sources at intermediate frequencies. No other scientific goals were identified at the onset of this project. The full survey consists of 217,446 “snapshot” observations of partially overlapping primary beam areas. Each “snapshot” was imaged separately over a time period of 30 seconds. The RMS brightness fluctuations for Stokes I are about 0.45 mJy/beam or 0.14 K. The survey consists of almost 2×10^6 discrete sources stronger than 2.5 mJy (Condon & et al. 1998). The following table compares the NVSS and CGPS surveys. The similarities of resolution and sensitivity make the NVSS an excellent tool for a comparison

<i>Survey</i>	<i>sensitivity</i> 1σ	<i>resolution</i> "	<i>obs frequency</i> MHz
NVSS	0.45	45	1400
CGPS	0.23	$60 \times 60 \text{ cosec } \delta$	1420

Table 4.1: Comparison of CGPS and NVSS survey parameters

variable search.

4.2 Removing Systematic Effects

In order to compare the two surveys a catalogue, covering the same region of the sky as the MVW mosaics, was made from the complete NVSS source catalogue. Since the CGPS catalogue contains sources with lower flux density than the NVSS catalogue, more sources are present in the CGPS catalogue. These two catalogues were then matched according to RA/DEC coordinates with a tolerance of 30 arc seconds – producing a catalogue of 3837 matched sources.

A test was done to see if there were any systematic differences between the two survey's integrated fluxes. The flux ratio (CGPS integrated flux over NVSS integrated flux) vs CGPS integrated flux graph is shown in Figure 4.1. A systematic difference is noticed between the two surveys. For strong sources the CGPS flux is on average 4% higher than the NVSS, and for weak sources ($\leq 10\text{mJy}$) there is a very strong deviation from the expected value of one, in the sense that the NVSS data has higher integrated flux for lower amplitude sources.

A correction was made to the NVSS data so as to remove this systematic differ-

<i>bin number</i>	<i>flux range (mJy)</i>		<i>mean ratio</i>	<i>RMS</i>
1	1	2	0.48	0.13
2	2	3	0.62	0.18
3	3	4	0.80	0.24
4	4	8	0.88	0.20
5	8	16	0.97	0.14
6	16	32	1.01	0.09
7	32	64	1.04	0.06
8	64	128	1.04	0.06
9	128	256	1.05	0.05
10	256	512	1.07	0.07
11	512	1024	1.06	0.06

Table 4.2: Binning of CGPS integrated flux density

ence in flux density between the two catalogues. The data were binned into 11 bins according to CGPS integrated flux – between 1 and 1024 mJy. The bins are shown in table 4.2; there are more bins included for smaller amplitudes as a result of the larger and more rapidly changing discrepancy.

The number of sources, mean flux, mean ratio, and RMS mean ratio were calculated for each bin. To remove the effects of possible highly variable sources from this calculation, sources that differed from the mean by more than 2.5σ , where σ is the RMS of the mean ratio, were removed. This process was done iteratively until no more sources above 2.5σ remained. The mean values are included in table 4.2, and a graph of mean flux ratio vs mean flux in each bin is shown below (Figure 4.2). A correction for each source was derived by linear interpolation using the following equation

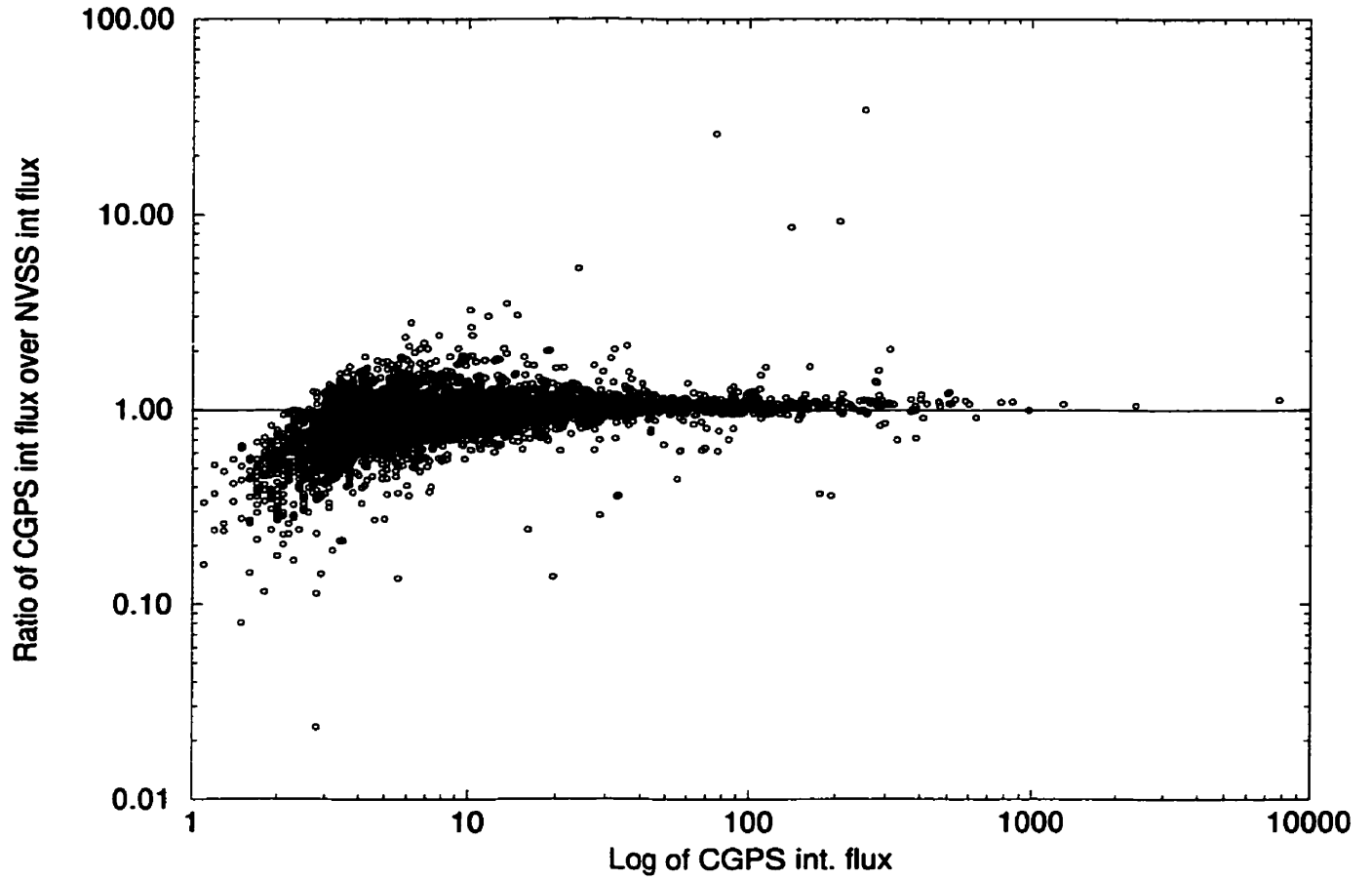


Figure 4.1: The preliminary systematic error graph of Flux ratio vs CGPS integrated flux

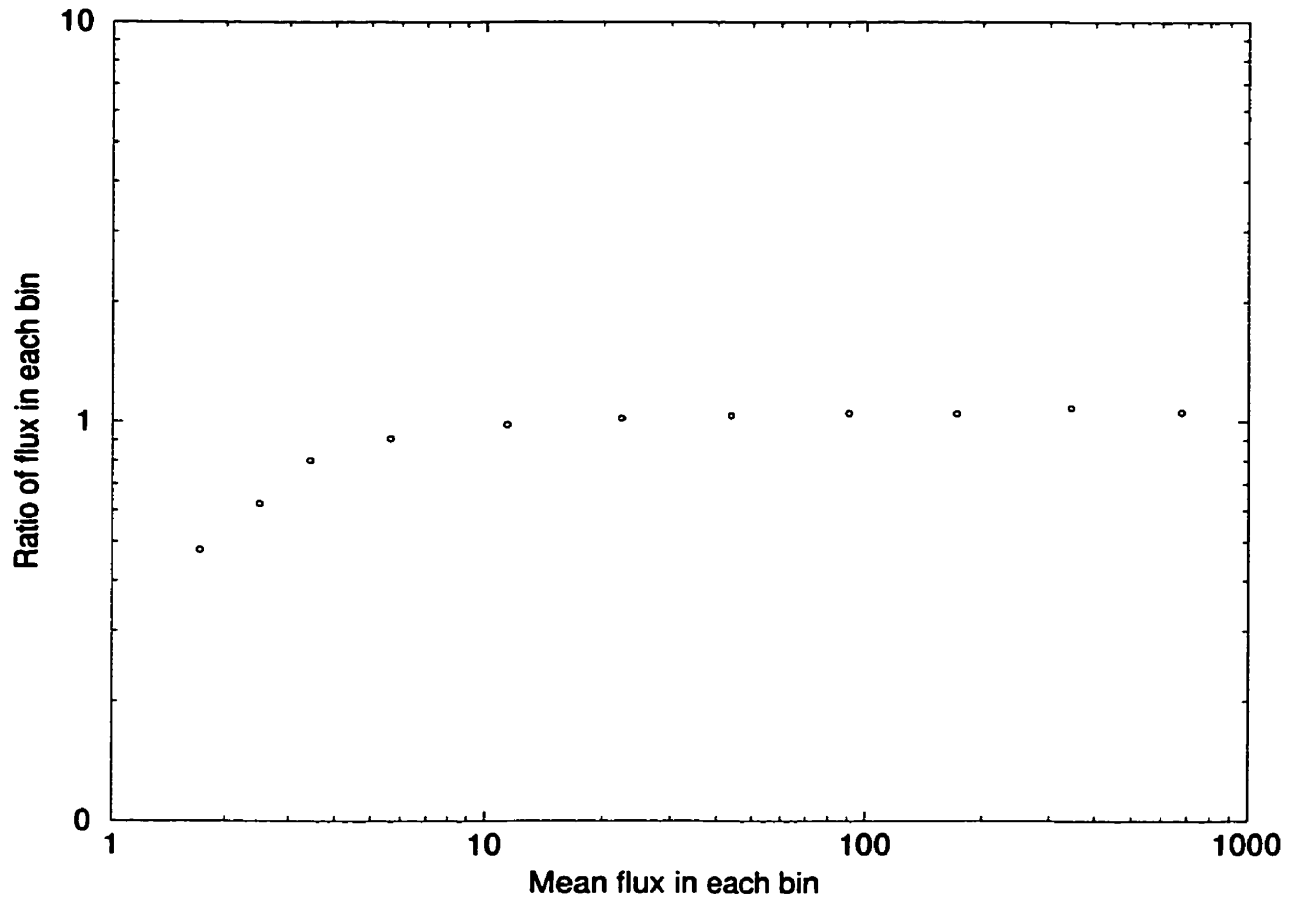


Figure 4.2: Mean flux ratio vs mean flux in each bin. Sources greater than 2.5σ from the mean have been removed to determine this mean.

$$y = y_1 + \frac{(y_2 - y_1)}{(x_2 - x_1)} \times (x - x_1). \quad (4.1)$$

Where x is the CGPS integrated flux value between the bin values of x_1 and x_2 and y is the flux ratio correction to be applied to the NVSS integrated flux for that bin. A new catalogue including the corrected NVSS integrated flux and uncertainty was made using the linear interpolation. For the remainder of this thesis, the NVSS integrated flux refers to the corrected integrated flux. The new flux ratio graph (Figure 4.3), below, shows that the systematic difference has been removed, as all sources are clustered around a ratio of 1.

4.3 Detection of Variability

For clarity in determining variables a graph of fractional differences in flux densities vs CGPS integrated flux was made (Figure 4.4), where the fractional difference in flux density is defined as:

$$\Delta = \frac{2(S_{CGPS} - S_{NVSS})}{(S_{CGPS} + S_{NVSS})}, \quad (4.2)$$

and the variance of the fractional difference in flux densities is:

$$\sigma_V^2 = \frac{16 \times S_{NVSS}^2}{(S_{CGPS} + S_{NVSS})^4} \times \sigma_{CGPS}^2 + \frac{16 \times S_{CGPS}^2}{(S_{CGPS} + S_{NVSS})^4} \times \sigma_{NVSS}^2 \quad (4.3)$$

Variable index is defined as fractional difference in flux densities divided by the square root of the variance.

$$V_I = \frac{\Delta}{\sigma_V} \quad (4.4)$$

If all source flux changes are due to noise, the variable index should be Gaussian shaped with a standard deviation of one. If variables are present then the wings

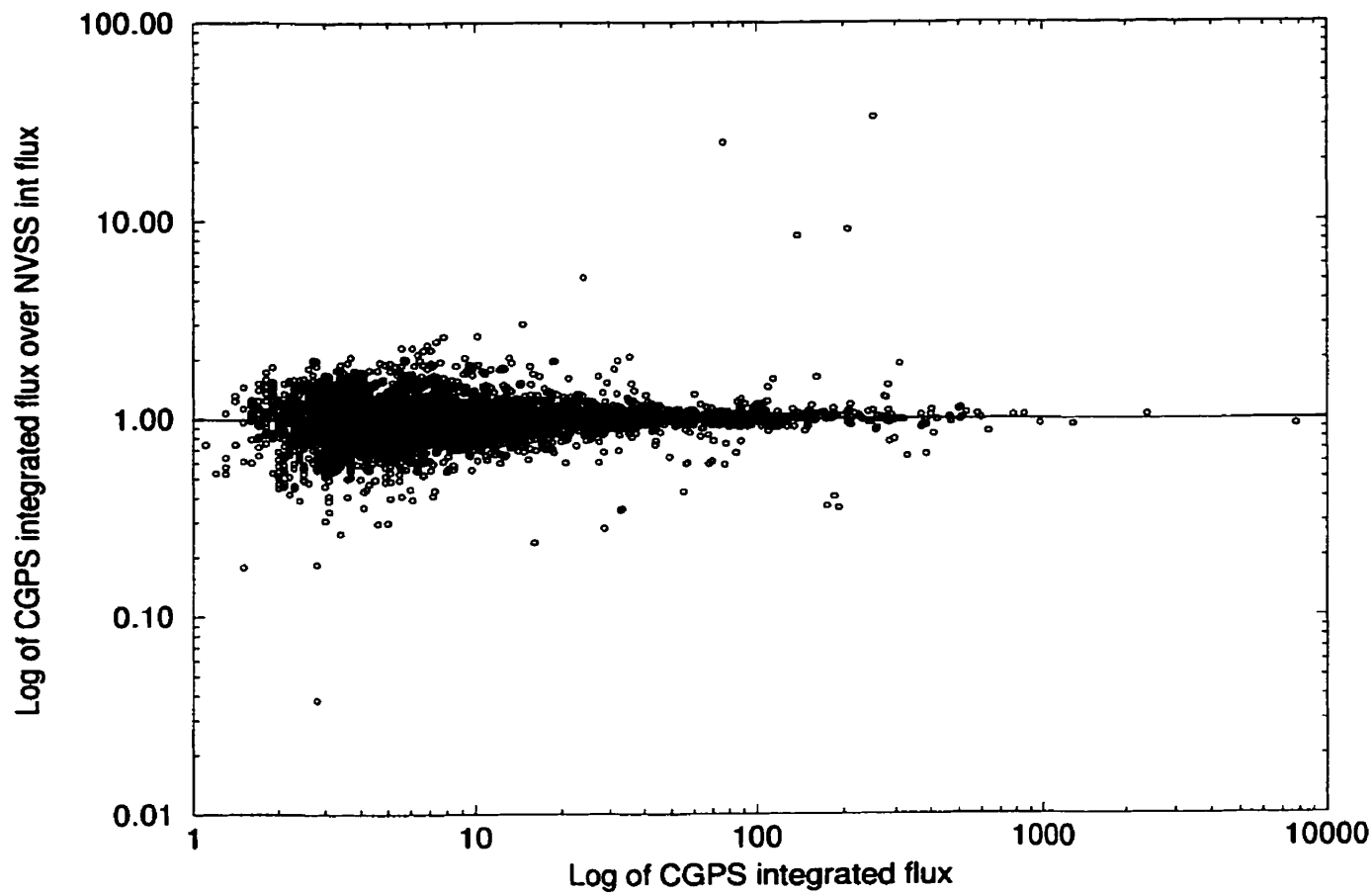


Figure 4.3: Corrected integrated flux ratio graph vs CGPS integrated flux

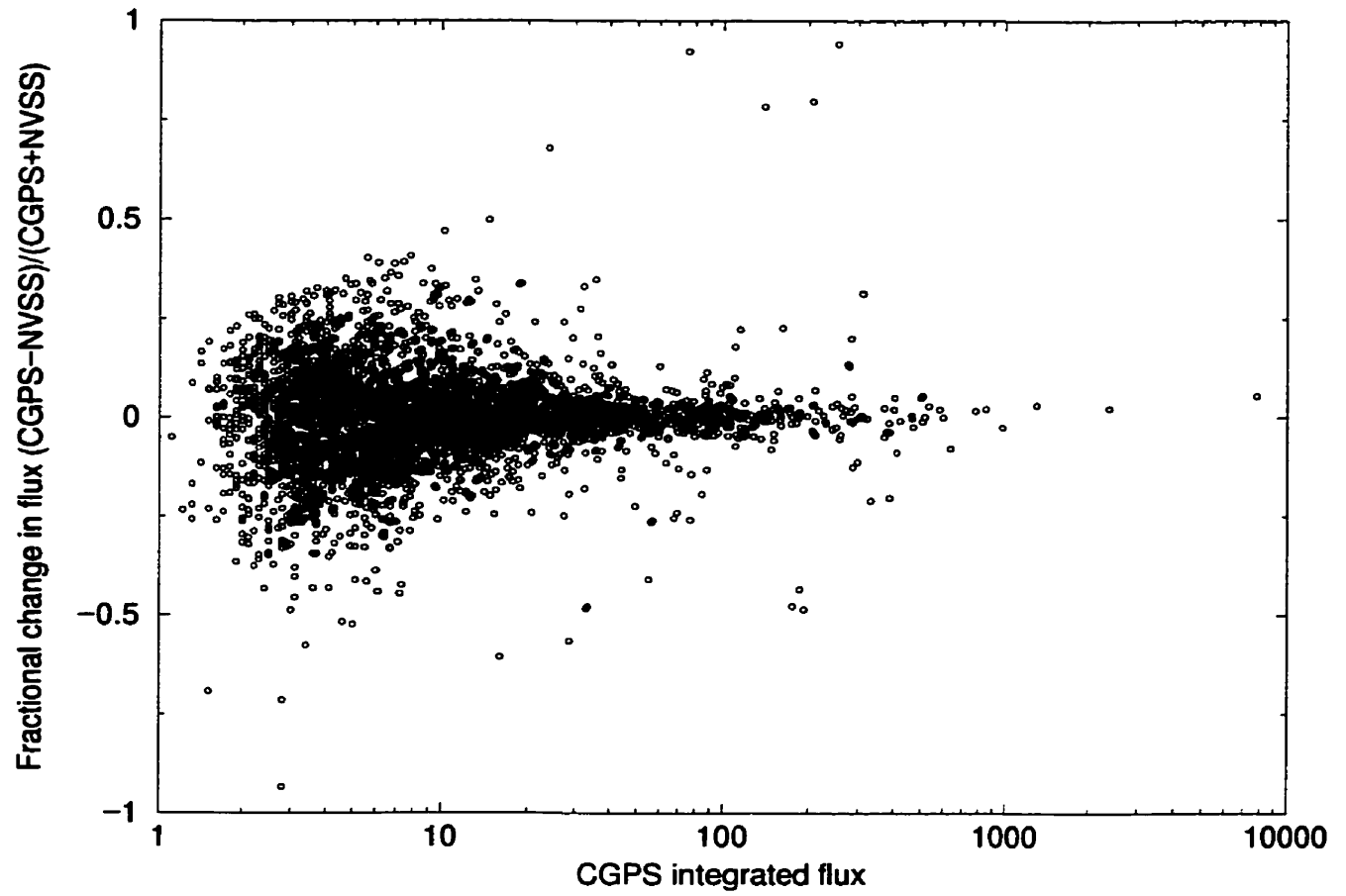


Figure 4.4: Graph of fractional change in flux densities vs CGPS integrated flux using corrected NVSS integrated flux

of the distribution will be more stretched out, as is seen in Figure 4.5. Therefore, the variable index can be used to check the uncertainties as well as determine the variability of a source. The variable index is used to determine the final list of variable sources. Based on the 3837 sources considered and the probability of 4σ (0.00006) and 3σ (0.00270) deviations from the mean, it is expected that 10 sources at 3σ occur due to random error, whereas, at 4σ only 0.2 random sources are expected to occur. Any source with variable index of greater than 4σ or less than -4σ is considered for a true variable (see Figure 4.6) and any source with variable index between 3σ and 4σ , or -3σ and -4σ , is considered for a possible variable.

There were 142 sources with variable index greater than $|3\sigma|$, possible and true variables. These sources needed to be checked by hand to see if the source was single with no extended nature. Sources that are close doubles might have been treated differently by the two surveys and therefore can not be considered as true variables. Sources that are slightly extended are rejected for similar reasons. From the 142 possible sources, 71 were single, isolated, compact sources. Of these 71 sources, 19 had a variable index above $|4\sigma|$ and are considered in the true variable source catalogue.

4.3.1 Unmatched Sources

To complete the variable search between the CGPS and NVSS catalogues it is important to check the unmatched sources, sources that appear in one list and not the other. There were 1524 sources present in the CGPS catalogue but not in the NVSS catalogue. Five of these sources had an integrated flux of over 100 mJy, 47 had an integrated flux over 10 mJy, and 1306 had an integrated flux below

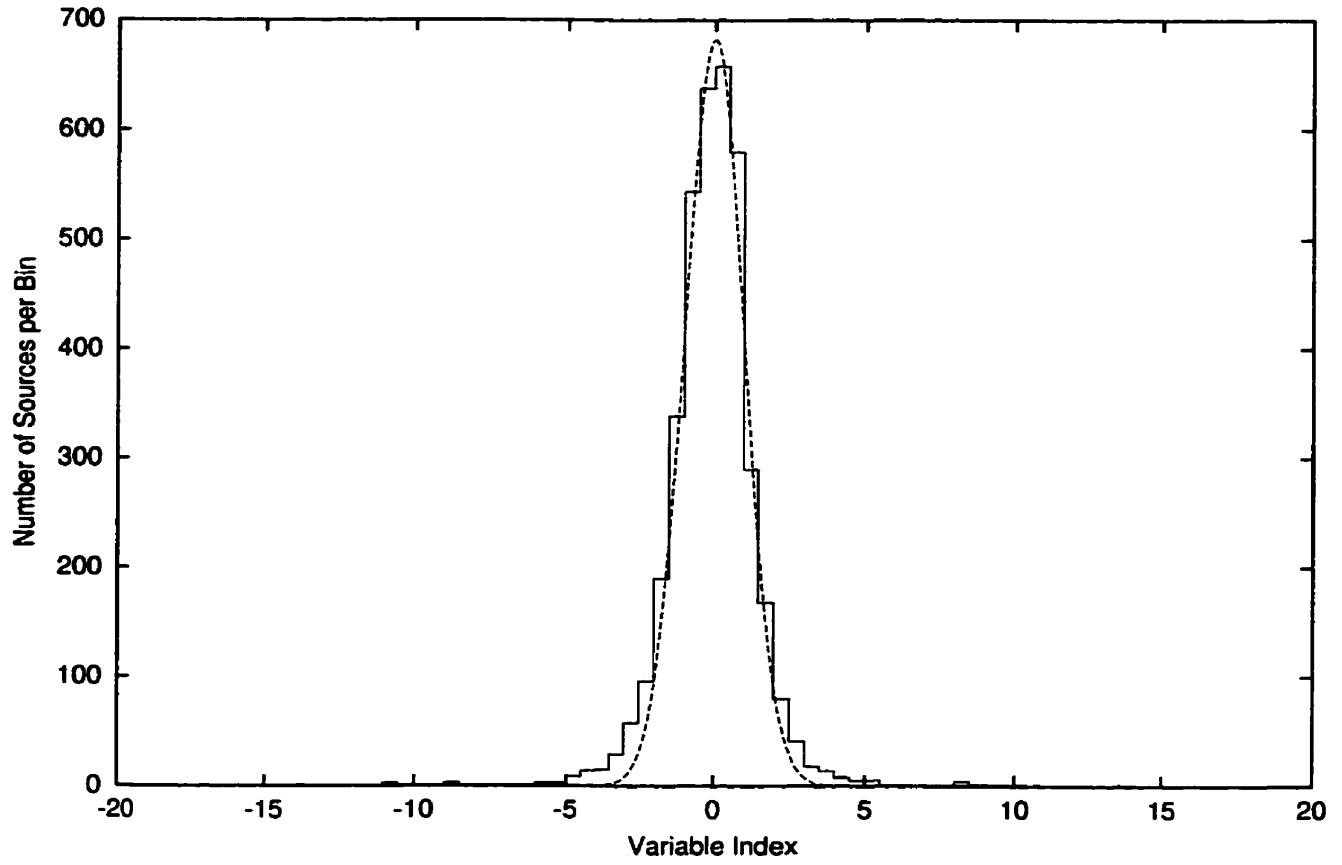


Figure 4.5: Graph of number of sources vs variable index. Overplot of Gaussian with standard deviation of one and mean zero.

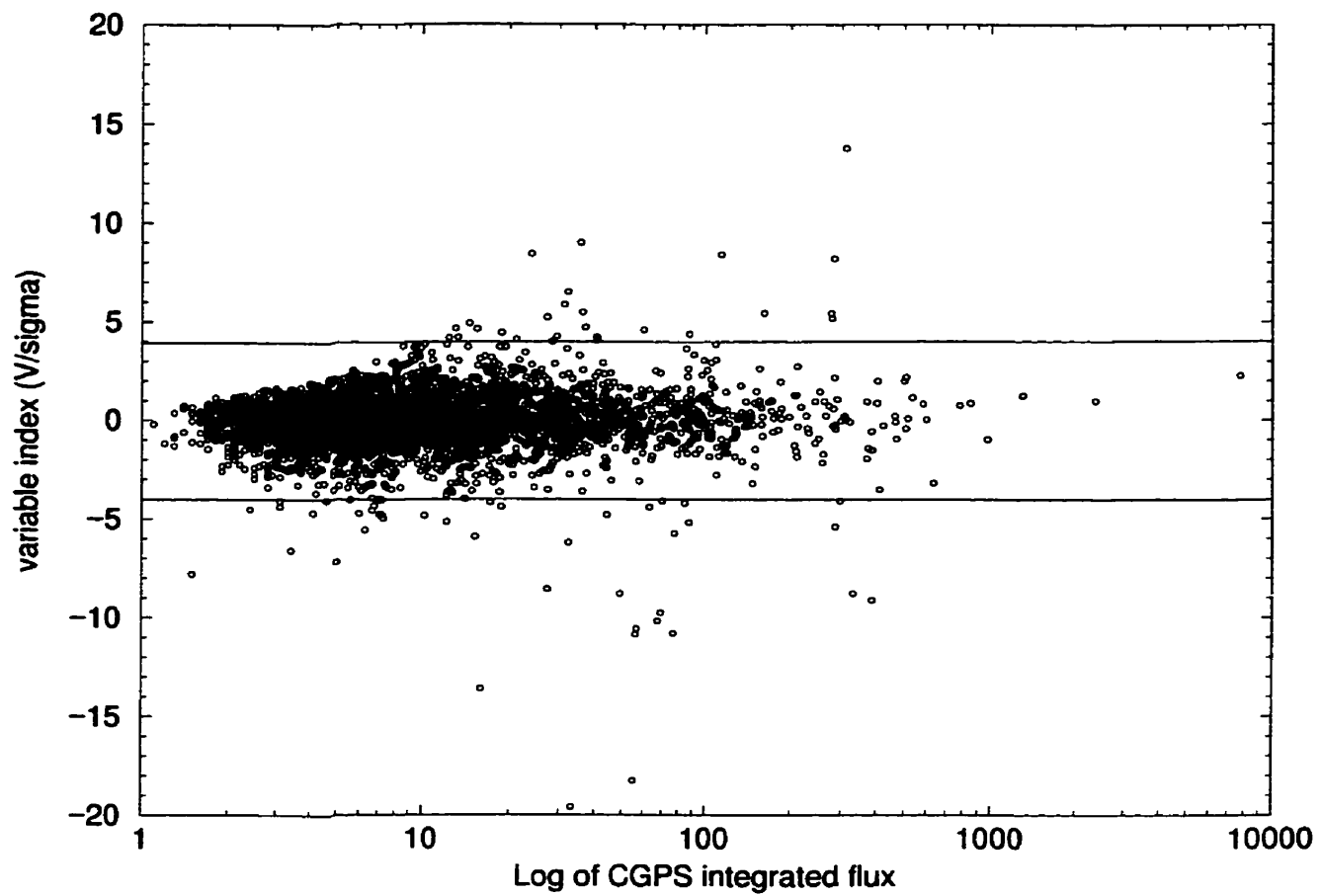


Figure 4.6: Graph of variable index vs CGPS integrated flux with $\pm 4\sigma$ lines indicated

3.5 mJy. The sources above 100 mJy were all extended but one. The source at $RA = 3^h16^m54.74^s, DEC = 53^\circ23'55''$ was not in the NVSS catalogue but is in the NVSS map. The source is single and not extended, however it is not variable according to a comparison of the NVSS and CGPS maps. The extended sources were not matched as FLUXFIT seems to have found a peak in a different location (greater than 30 arcsec away) than the NVSS survey. The brightest 32 sources below 100mJy were checked by hand, 19 were extended, four were close doubles, four turned out not to be variables as a result of not being entered in the NVSS catalogue, and four “sources” found by FLUXFIT were not in either the NVSS or CGPS maps. This strange phenomenon occurs only on the very edge of the mosaics where the noise level is highest. Why this occurs will need to be looked at.

Sources that are in the NVSS catalogue and not the CGPS catalogue also needed to be checked. There were 4968 sources in the NVSS catalogue between the range of 147.99 and 138.00 degrees longitude. This range is slightly larger than that of the CGPS MVW mosaics, so a large number of the unmatched sources were missed as a result of being out of the range of the CGPS images. There are some artefacts in the NVSS image around the bright source with $l = 143.89$ and $b = -1.0578$. These artefacts appear as small “sources” in a ring around the bright source; and are seen as negative as well as positive deflections (Figure 4.7). These “sources” are a result of the map artefacts, and are not real. They are however, in the NVSS catalogue. Despite the artefacts, there were still other sources that needed to be checked by hand. There were 98 sources with integrated flux density of greater than 10 mJy, 51 were out of range, 34 were extended, 7 were close doubles, 3 turned out not to be variable, all of which were on the very edge of the mosaic, and 3 were variables. A

table of all the variables found is in the next chapter.

4.4 Spectral Index Determination

Along with a variable search, the spectral index of the sources was also calculated. This was done by comparing the CGPS with the Westerbork WENSS 325 MHz and Cambridge 151 MHz surveys. These surveys and the spectral index determination are described below.

4.4.1 The Westerbork Northern Sky Survey

The Westerbork 92 cm survey covers approximately 570 square degrees of the northern sky greater than declination $\delta = 30^\circ$. The survey consists of 80 evenly spaced fields, each of which were observed with the Westerbork Synthesis Radio Telescope for 12 hours at different array configurations, using a bandwidth of 5MHz. Observations began in the spring of 1991. The catalogue consists of 11,299 sources with a limiting flux density of about 18 mJy. The sensitivity of the CGPS is better but the resolution of the WENSS survey is similar with $54'' \times 54'' \text{cosec}\delta$ (Rengelink et al. 1997).

4.4.2 The Cambridge 151 MHz survey

The Cambridge 7C(G) survey is another galactic plane survey covering a range between $80^\circ < l < 104^\circ$ and $126^\circ < l < 180^\circ$, for $-5.5^\circ < b < 5.5^\circ$. Observations were taken at the Cambridge Low Frequency Telescope from 1990 to 1991, and some fields were re-observed in 1993 and 1994. There are 96 high resolution maps and 24 low resolution maps. The high resolution is 70 arcsec which is similar to the

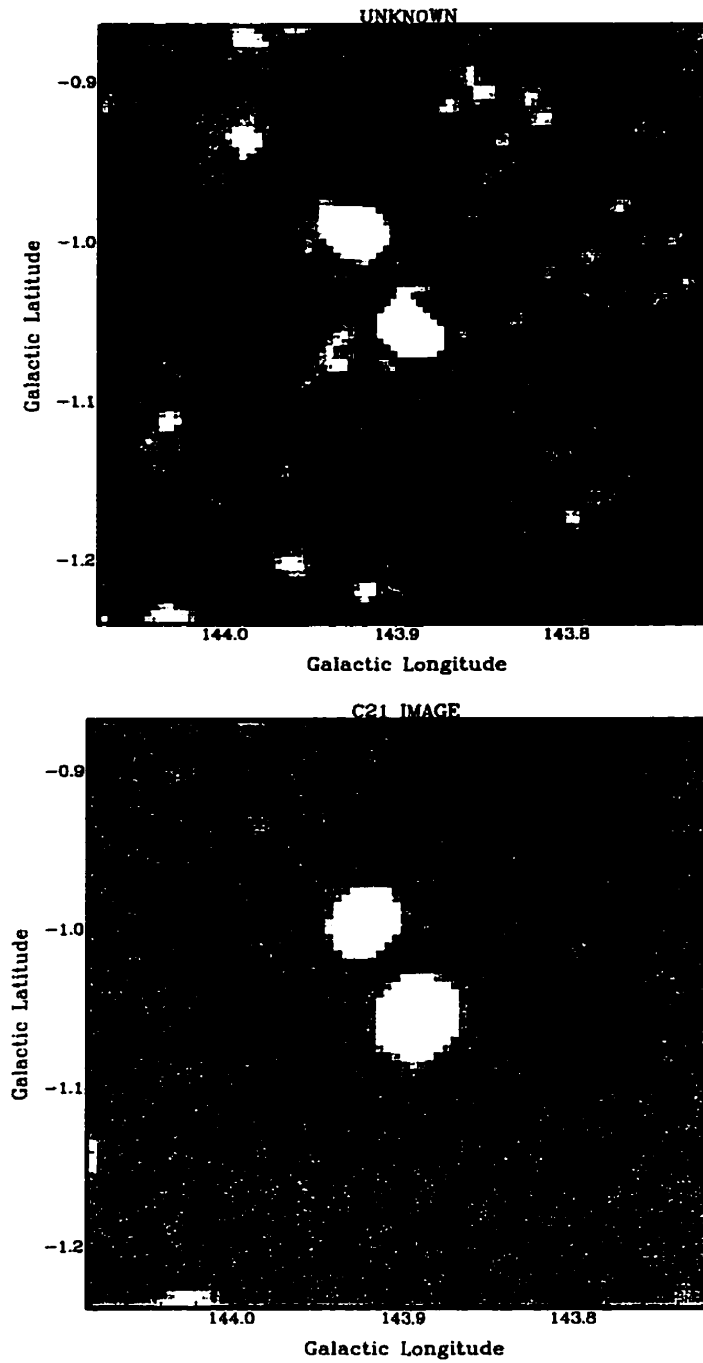


Figure 4.7: (top) NVSS image including artefacts in a ring shape about the centre source. (bottom) CGPS image of same area with no ring of artefacts present.

CGPS, however the sensitivity is much lower having an average completeness limit for compact sources of 250 mJy. The catalogue consists of 6262 compact sources, with a positional accuracy of better than 10 arcsec (Vessey & Green 1998). As the sensitivity of this survey is much less than the CGPS it is expected that not many sources will be matched between the two surveys. Of the matched sources, most will have negative spectral indices.

4.4.3 CGPS spectral index determination

Finding the spectral index of sources in the CGPS was done using flux density information from the Westerbork survey (325 MHz) and the Cambridge 7C survey (151 MHz). Spectral index was calculated for both α_{1420}^{325} and α_{1420}^{151} . There were 619 sources in the Cambridge survey that overlapped with the CGPS MVW mosaics, 338 sources were matched with a tolerance of 30 arc seconds. The Westerbork survey had 2012 sources in the MVW region, 1806 of these sources matched. This resulted in 47% of the CGPS sources having spectral index information. Of the 71 possible variables 50 have spectral index information, and nine of these indicate a thermal source.

As expected, the majority of compact sources are non-thermal emitters. It should be noted that the spectral indices given for the variable sources are only an indication of their spectrum. To get an accurate measure of the spectral index of a variable, either repeated measurements of flux density would have to be taken and averaged for each frequency, or multiple frequency measurements would have to be taken at the same time. As only one measurement of the flux density was taken for each frequency at different times the spectral index can only be used to suggest whether

the source is thermal or non-thermal.

The spectral index distribution for the entire catalogue is expected to peak around -0.85, the typical spectral index of an extragalactic radio galaxy. Figure 4.8 shows the spectral index distribution for matched 325/1420 MHz sources and the 151/1420 MHz sources respectively. As expected, both histograms show a peak around -0.85.

4.5 Polarisation

The polarisation of a source can give valuable information about its nature. Pulsars, for instance, are strongly linearly polarised, while supernova remnants are between 5 and 15% polarised. Polarisation maps made from Stokes Q and U images of the MVW mosaics were used to check the polarisation of the variable sources. No significant polarisation was found.

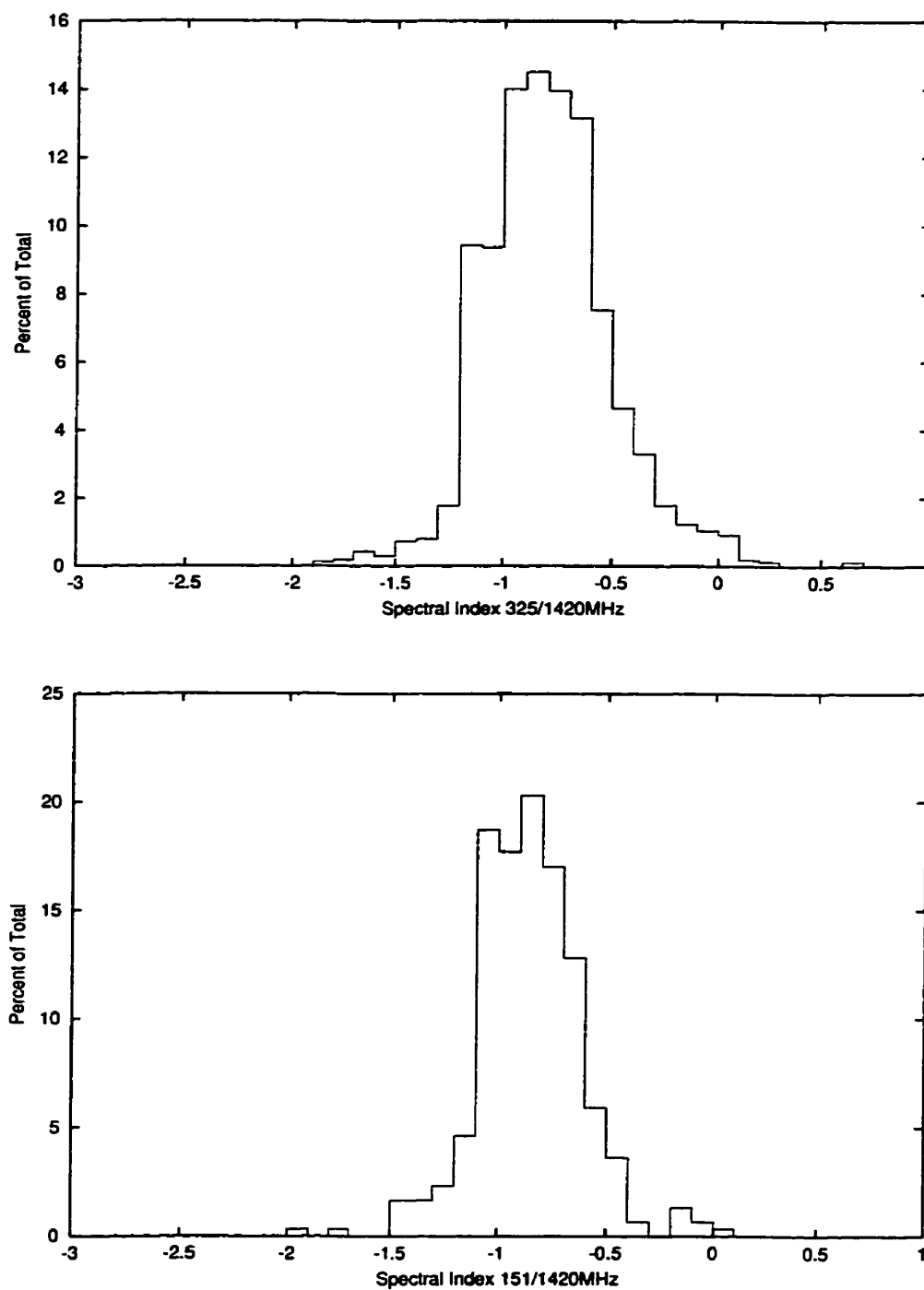


Figure 4.8: (top) The spectral index distribution between 325 MHz and 1420 MHz.
(bottom) The spectral index distribution between 151 MHz and 1420 MHz

Chapter 5

Results

The CGPS variable search covered an area of 81 square degrees, in which 3837 sources, with flux densities down to the order of 1.0 mJy, were checked for variability. A list consisting of 142 possible variable sources was compiled, and after checking for discreteness (single, isolated, compact object) only 60 possible variables remained. The following results only pertain to the true variables ($|V_I| > 4\sigma$) that are single, isolated and compact sources. Sources that are slightly extended or are a component of a multiple source are not considered in this thesis. These objects are left for further study. The following is a catalogue of variable sources in the MVW mosaics and comparison contour plots of NVSS and CGPS images verifying their variability.

5.1 The Variable Sources

The results of the CGPS variable search are given in Table 5.1. This table shows the 19 variables that were found by matching the NVSS data and the CGPS data. The three variables that were found as a result of the unmatched data are given in table 5.2. Both of these tables are sorted by galactic longitude. The first column of table 5.1 is the source number. The next two columns give the right ascension and declination coordinates, with uncertainty, for the 2000 epoch. The fourth and fifth columns give the galactic coordinates. Following the coordinates is the NVSS integrated flux and CGPS integrated flux with uncertainties. The variable index is

given next; this is the value that determined whether or not the source was variable. All of the sources in table 5.1 have a variable index above 4 or below -4σ . Variable index is a value to denote how many sigma away from the mean that particular source lies ($V_I = \Delta/\sigma$). The fractional difference in flux, given in column 8, is a measure of how much the flux changed between the two surveys. The last two columns are the spectral index of the variables. First is the comparison between the CGPS and Westerbork WENSS survey, α_{1420}^{325} . Second, the CGPS-Cambridge spectral index is given, α_{1420}^{151} . Again it should be noted that these values are only indications of the sources' true spectral index. If the spectral index is negative then the source is probably a synchrotron emitter, and if it is positive, then it is likely a thermal emitter.

Table 5.2 gives the parameters of the variable sources found as unmatched sources. All three of these sources were not in the CGPS catalogue but were in the NVSS catalogue, their information stems from the NVSS catalogue. Similar to the Table 5.1, the first column is the source number, the next two columns are the right ascension and declination with uncertainty for the 2000 epoch. The following two columns are the galactic coordinates, galactic longitude and galactic latitude. The peak flux with uncertainty is given in column 5, followed by the integrated flux and its uncertainty. The next column is an estimated upper limit on the CGPS data. The upper limit was estimated by finding the location of the source in the CGPS map. The peak brightness temperature at this location is found using KVIEW, and the average background noise is determined. Subtracting the background noise from the peak brightness temperature results in an upper limit of the brightness temperature,

<i>num</i>	<i>RA J2000</i> <i>h m s s</i>	<i>DEC J2000</i> <i>d m s s</i>	<i>l</i> <i>deg</i>	<i>b</i> <i>deg</i>	<i>NVSS iflux</i> <i>mJy</i>	<i>CGPS iflux</i> <i>mJy</i>	<i>VI</i>	<i>FF</i>	α_{1420}^{325}	α_{1420}^{151}
1	2 51 54.59 ±0.01	56 16 19.6 ±0.1	139.1288	-2.7635	210.8 ±10.7	277.0 ±1.5	5.4	0.27	0.33	NA
2	2 59 39.51±0.02	57 39 14.1 ±0.2	139.4315	-1.0510	77.7 ±4.0	49.3 ±0.7	-8.8	-0.45	-0.42	NA
3	3 34 26.78±0.29	60 8 25.6 ±2.4	141.9332	3.4274	6.0 ±0.7	2.4 ±0.5	-4.5	-0.86	NA	NA
4	3 39 9.43±0.01	60 8 56.8 ±0.1	142.4028	3.7798	189.2 ±9.6	284.0 ±1.8	8.2	0.40	0.74	NA
5	3 37 43.18±0.03	59 47 48.6 ±0.2	142.4674	3.3895	113.3 ±5.8	67.6 ±1.0	-10.2	-0.50	-0.23	NA
6	3 19 0.67±0.21	54 52 40.8 ±1.9	143.1510	-2.0936	13.3 ±1.3	6.7 ±0.9	-4.5	-0.66	NA	NA
7	3 25 56.46±0.09	55 44 34.1 ±0.7	143.5063	-0.8312	6.9 ±1.1	13.4 ±0.8	4.2	0.64	-0.31	NA
8	3 24 25.60±0.09	55 20 43.9 ±0.8	143.5477	-1.2806	8.6 ±1.1	15.5 ±0.9	4.6	0.57	NA	NA
9	3 54 38.69±0.06	60 18 55.0 ±0.5	143.8146	5.0992	23.6 ±1.5	17.3 ±0.7	-4.2	-0.31	-0.65	NA
10	3 25 55.72±0.20	55 6 48.9 ±1.5	143.8545	-1.3553	4.9 ±1.2	14.6 ±1.9	4.9	1.00	-1.10	NA
11	3 28 57.39±0.07	55 13 30.9 ±0.6	144.1501	-1.0206	23.9 ±1.5	36.2 ±1.6	5.5	0.41	-0.93	-1.02
12	3 29 13.98±0.04	55 1 22.9 ±0.3	144.2970	-1.1651	30.8 ±1.8	40.4 ±1.1	4.2	0.27	-0.71	NA
13	3 46 47.59±0.07	57 28 42.1 ±0.6	144.8117	2.2559	15.6 ±1.2	10.2 ±0.5	-4.8	-0.42	NA	NA
14	3 32 59.38 ±0.01	54 34 42.8 ±0.1	144.9954	-1.2207	162.2 ±8.2	310.3 ±1.7	13.8	0.63	-0.86	-0.71
15	3 39 35.36 ±0.02	55 33 8.2 ±0.2	145.1898	0.1221	114.4 ±5.8	87.7 ±1.1	-5.2	-0.26	-0.356	NA
16	4 4 33.58±0.11	59 36 20.6 ±0.8	145.2230	5.3741	19.5 ±1.4	29.4 ±2.1	4.2	0.40	NA	NA
17	3 40 22.95±0.05	53 32 33.3 ±0.5	146.4822	-1.4213	91.0 ±4.6	70.4 ±2.7	-4.1	-0.26	-0.18	NA
18	3 42 58.26±0.12	53 30 44.6 ±1.0	146.8076	-1.2138	124.8 ±6.4	84.3 ±6.8	-4.2	-0.39	0.19	NA
19	4 11 23.63±0.14	57 35 33.1 ±1.1	147.2467	4.4911	101.4 ±5.1	161.0 ±11.7	5.4	0.46	-0.54	-0.64

Table 5.1: Variable list from MVW mosaics

which is converted to flux density using

$$S = \frac{2kT\nu^2\Omega}{c^2}, \quad (5.1)$$

where $\Omega = 1.64 \times 10^{-7}$ sr for the CGPS, k is Boltzmann's constant, T is brightness temperature, ν is frequency, and c is the speed of light. This equation gives SI units which are then converted to mJy. In the last column is the size of the source – this is the area within the FWHM of the 2D Gaussian in units of arcseconds. A fractional flux and variable index can not be given for these sources as they are not visible in the CGPS maps and therefore do not have catalogue information. In all cases the change in flux density is much greater than 100%.

Past surveys such as the Westerbork 327MHz survey found about 1% variability. Considering the 19 variables found from 3837 match sources results in only 0.5% variability. When the 3 additional variables are included, this percentage drops to 0.4% for the 5498 sources found in the MVW mosaic. These low percentages could be a result of neglecting the close doubles and extended sources. Another possibility is that the CGPS is more sensitive than past surveys. A test of variability as a function of flux density was performed on the CGPS data, the results are shown in table 5.3 below. This table shows that the percentage of variability matches past studies when restricted to higher flux densities.

5.2 Contour Plots of Variable Sources

To ensure that each source was a clear detection in each catalogue a contour plot of the CGPS and NVSS maps for each source was made. These plots are presented here. The CGPS maps are in galactic coordinates and have contours of surface brightness

<i>num</i>	<i>RA J2000</i> <i>hours</i>	<i>DEC J2000</i> <i>degrees</i>	<i>l</i> <i>deg</i>	<i>b</i> <i>deg</i>	<i>NVSS pflux</i> <i>mJy</i>	<i>NVSS iflux</i> <i>mJy</i>	<i>CGPS limit</i> <i>mJy</i>	<i>size</i> <i>area</i>
20	3.3454 ±0.14	55.2661 ±1.55	143.1492	-1.6347	9.02 ±0.54	11.13 ±1.2	0.6	1.2339
21	3.7220 ±0.11	54.3043 ±1.55	146.3685	-0.5528	9.49 ±0.54	10.5 ±1.1	1.0	1.1020
22	3.7708 ±0.09	54.4846 ±1.46	146.5961	-0.1496	10.5 ±0.6	11.1 ±1.1	4.0	1.0510

Table 5.2: List of unmatched variable sources. Data are from the NVSS source catalogue.

<i>limiting flux density mJy</i>	<i>% variability</i>
20.0	1.4
40.0	2.0
60.0	3.0
80.0	3.5
100.0	4.2

Table 5.3: Percentage of variability as a function of flux density.

in units of Kelvin. For ease of comparison the NVSS maps were converted to galactic coordinates also with contours of surface brightness. It should be noted however, that since the CGPS data has short spacing information there is a background of about five degrees Kelvin present that is not present in the NVSS maps. This background is assumed to be constant over the CGPS mosaics for the purposes of these contour plots; in that, the contours on the CGPS maps are set five Kelvin higher than the NVSS maps in order to compensate for the background. Since the background is not constant over the CGPS mosaics these contour plots do not have identical contours, however the consistent correction is approximately correct and these contour plots do show the variability of the above sources. The variable sources will be in the centre of the image, except in two cases where the source was on the edge of the CGPS mosaic. In these cases an arrow indicates the variable source. An arrow is also used for the variable sources found from unmatched data.

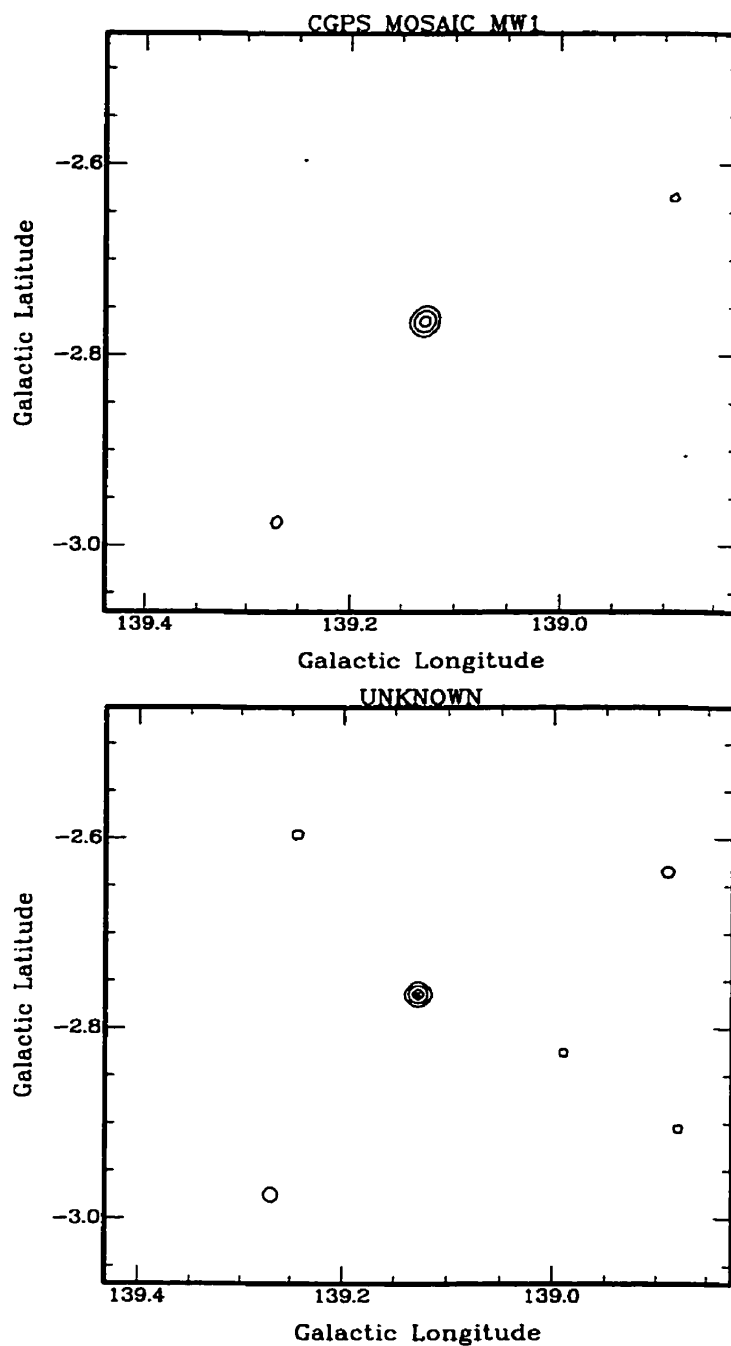


Figure 5.1: Comparison of the CGPS (top) and NVSS (bottom) contour plots for source 1. The base contour for the CGPS is 10K, while the base for the NVSS is 5K, the contour interval is 20K.

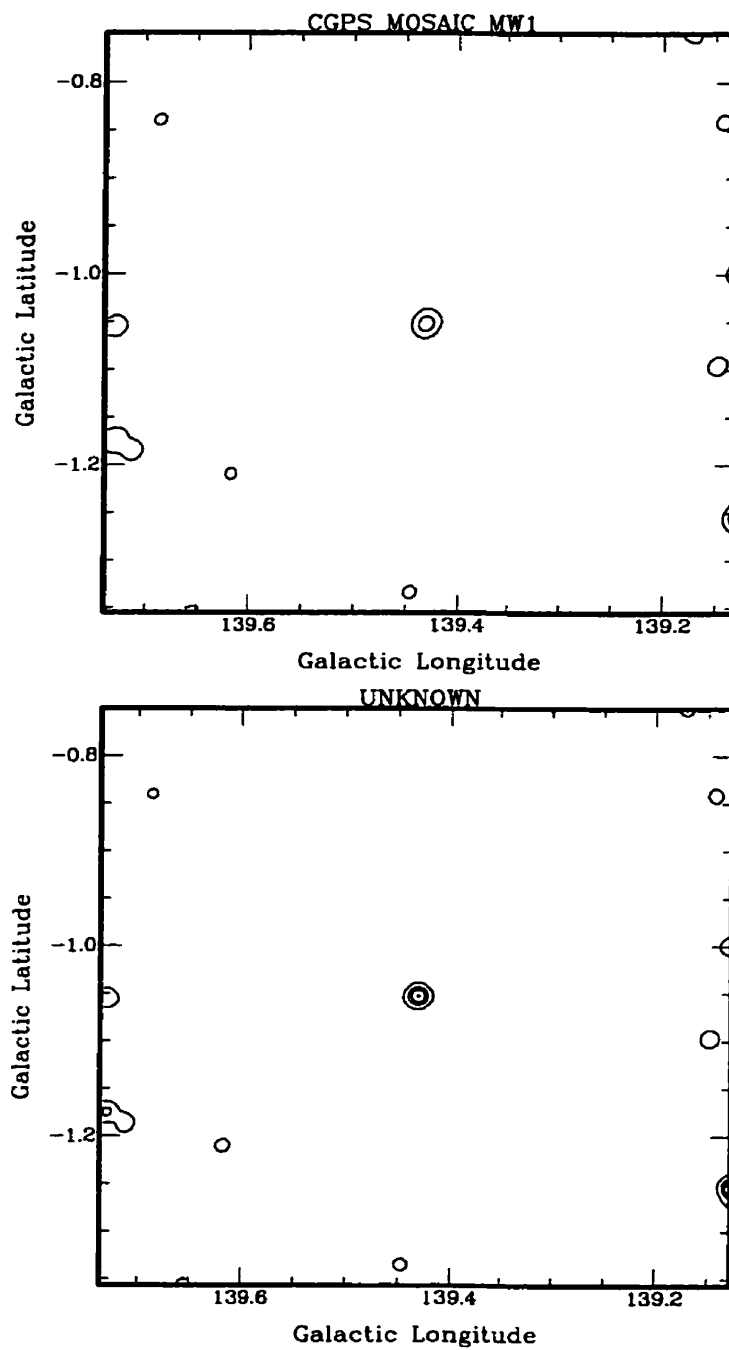


Figure 5.2: Comparison of the CGPS (top) and NVSS (bottom) contour plots for source 2. The base contour for the CGPS is 6K, while the base for the NVSS is 1K, the contour interval is 5K.

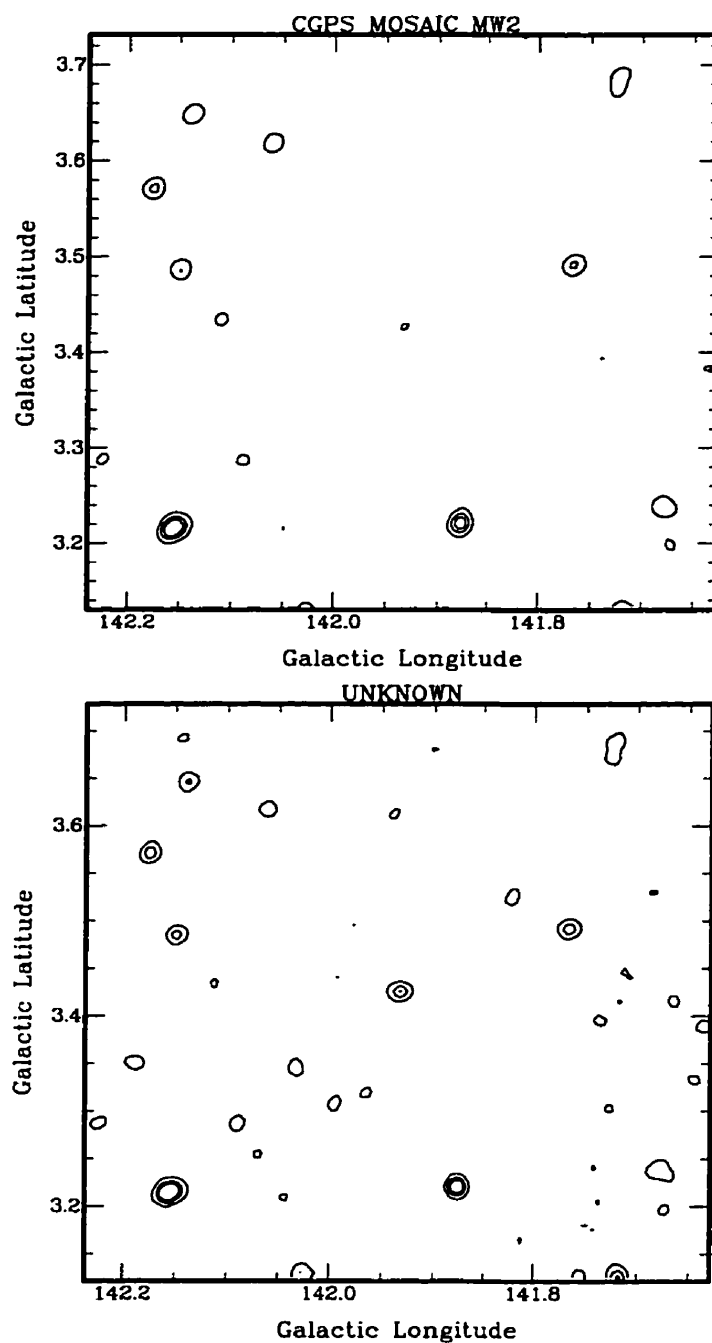


Figure 5.3: Comparison of the CGPS (top) and NVSS (bottom) contour plots for source 3. The base contour for the CGPS is 5.4K, while the base for the NVSS is 0.4K, the contour interval is 1K.

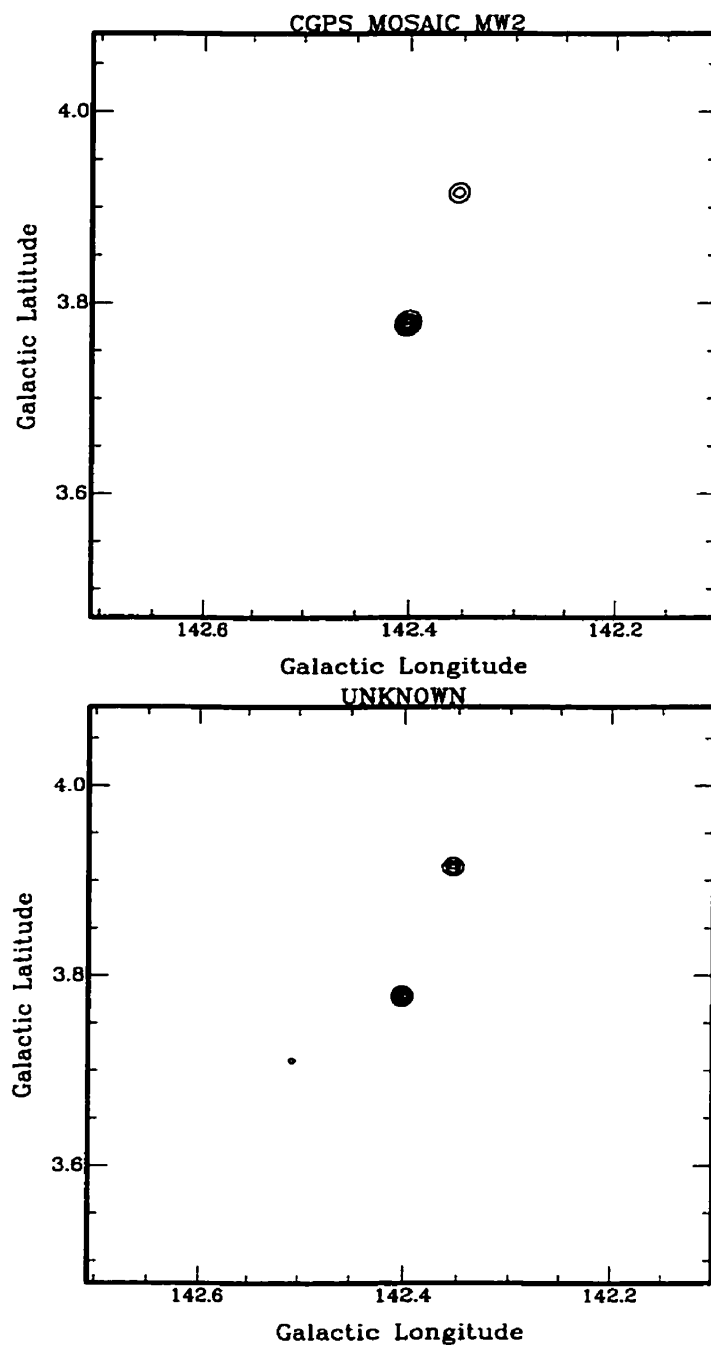


Figure 5.4: Comparison of the CGPS (top) and NVSS (bottom) contour plots for source 4. The base contour for the CGPS is 17K, while the base for the NVSS is 12K, the contour interval is 10K.

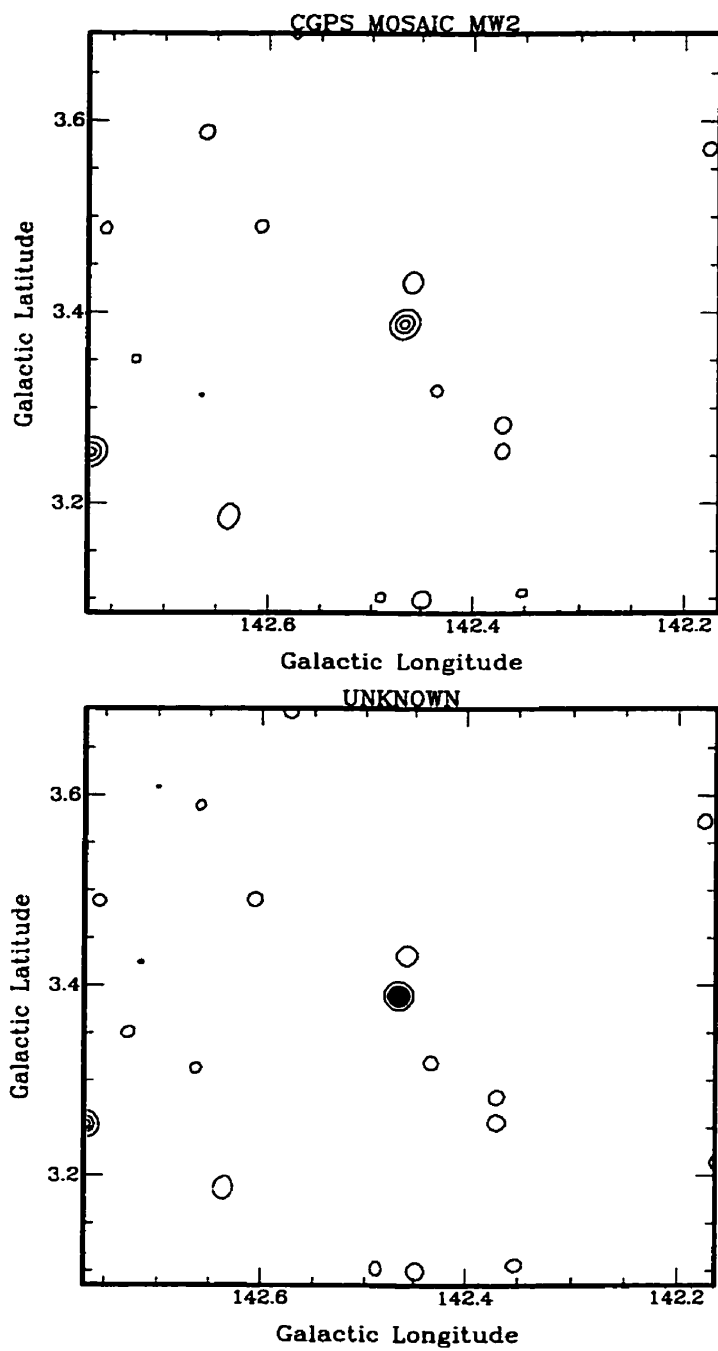


Figure 5.5: Comparison of the CGPS (top) and NVSS (bottom) contour plots for source 5. The base contour for the CGPS is 6K, while the base for the NVSS is 1K, the contour interval is 5K.

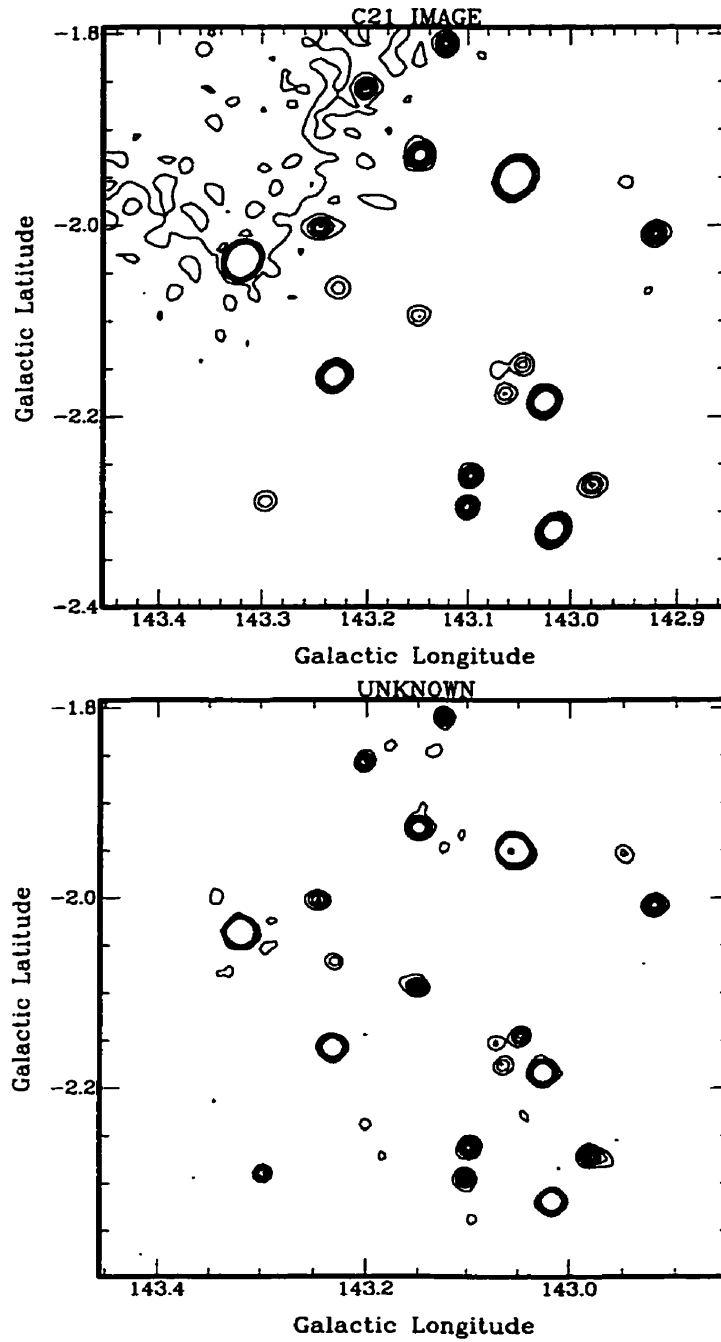


Figure 5.6: Comparison of the CGPS (top) and NVSS (bottom) contour plots for source 6. The base contour for the CGPS is 5.5K, while the base for the NVSS is 0.5K, the contour interval is 0.5K. Background noise visible in top image.

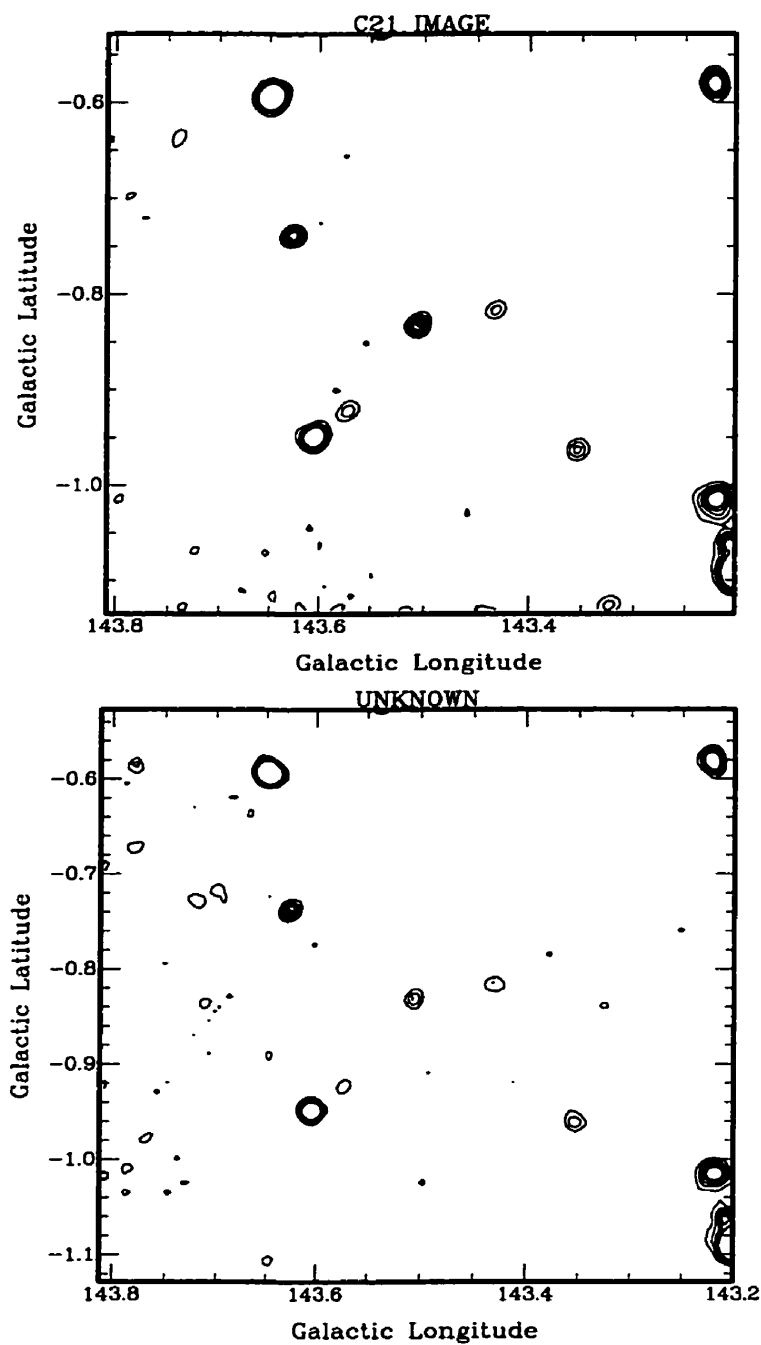


Figure 5.7: Comparison of the CGPS (top) and NVSS (bottom) contour plots for source 7. The base contour for the CGPS is 5.5K, while the base for the NVSS is 0.5K, the contour interval is 0.5K.

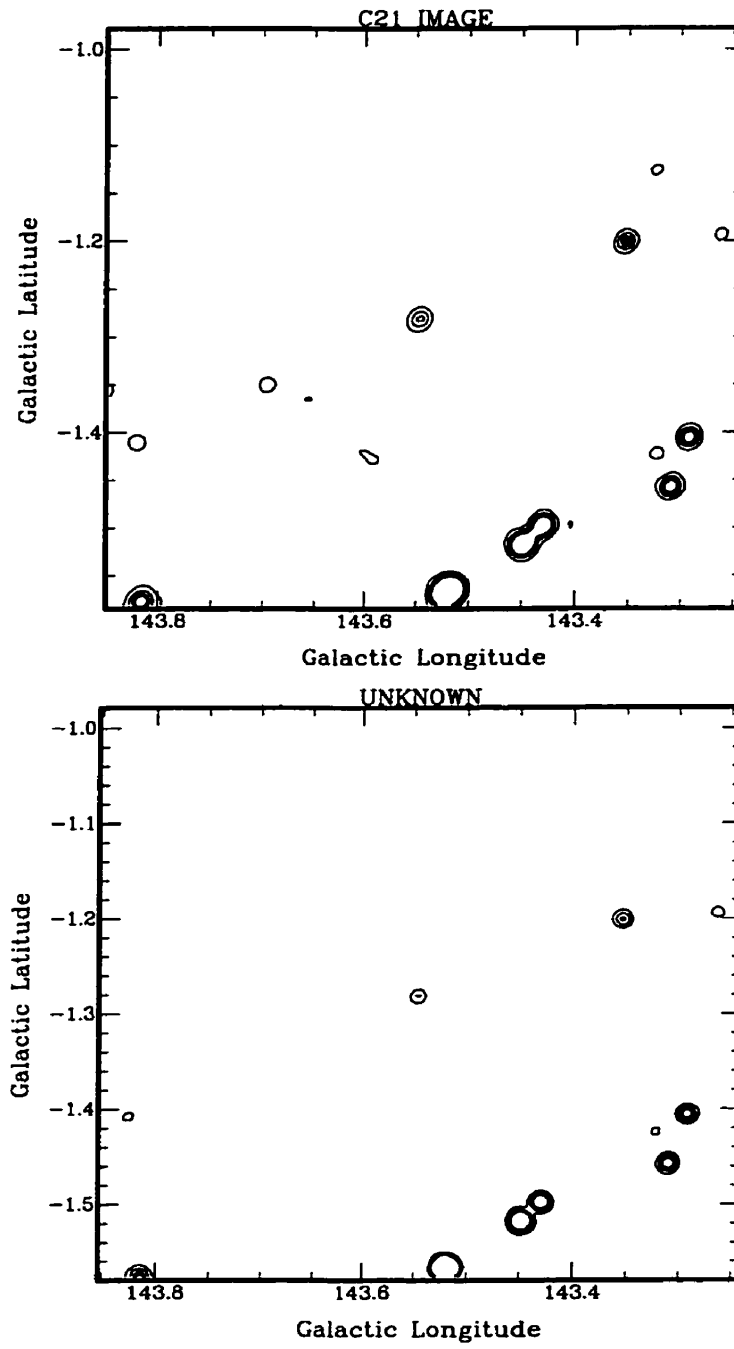


Figure 5.8: Comparison of the CGPS (top) and NVSS (bottom) contour plots for source 8. The base contour for the CGPS is 6K, while the base for the NVSS is 1K, the contour interval is 1K.

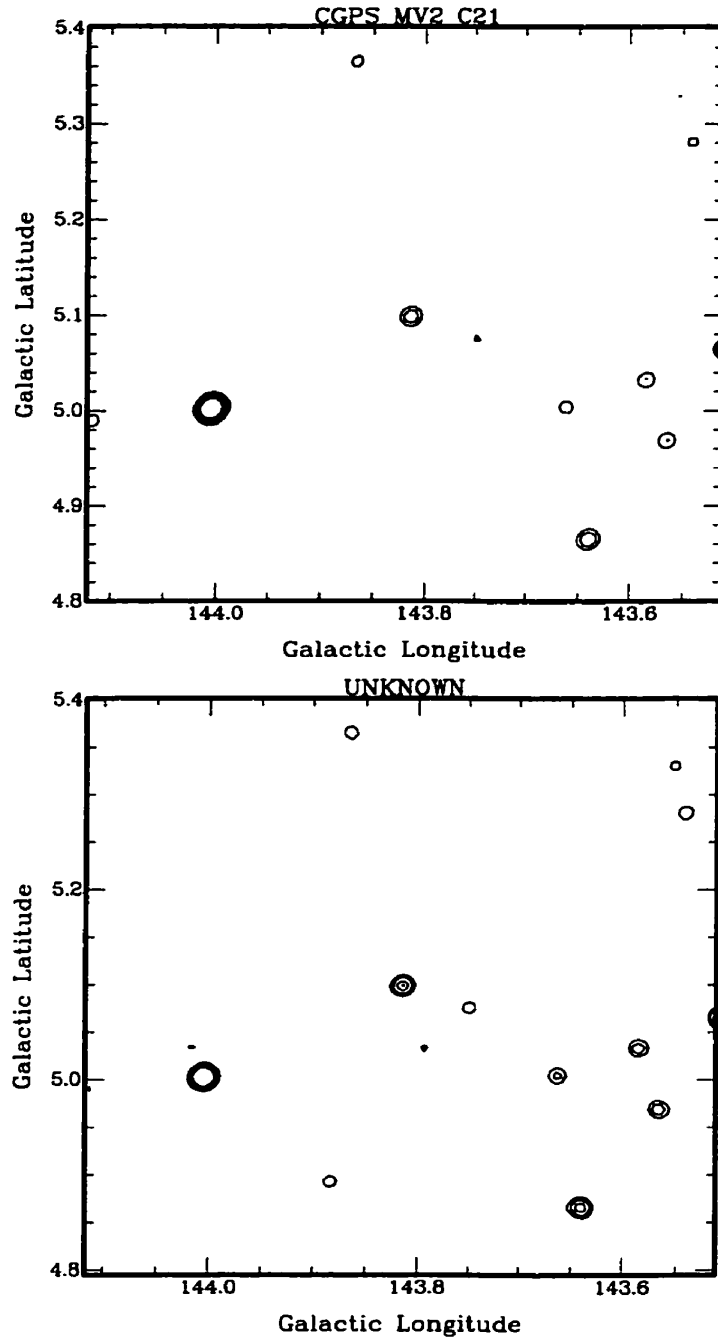


Figure 5.9: Comparison of the CGPS (top) and NVSS (bottom) contour plots for source 9. The base contour for the CGPS is 6K, while the base for the NVSS is 1K, the contour interval is 1.5K.

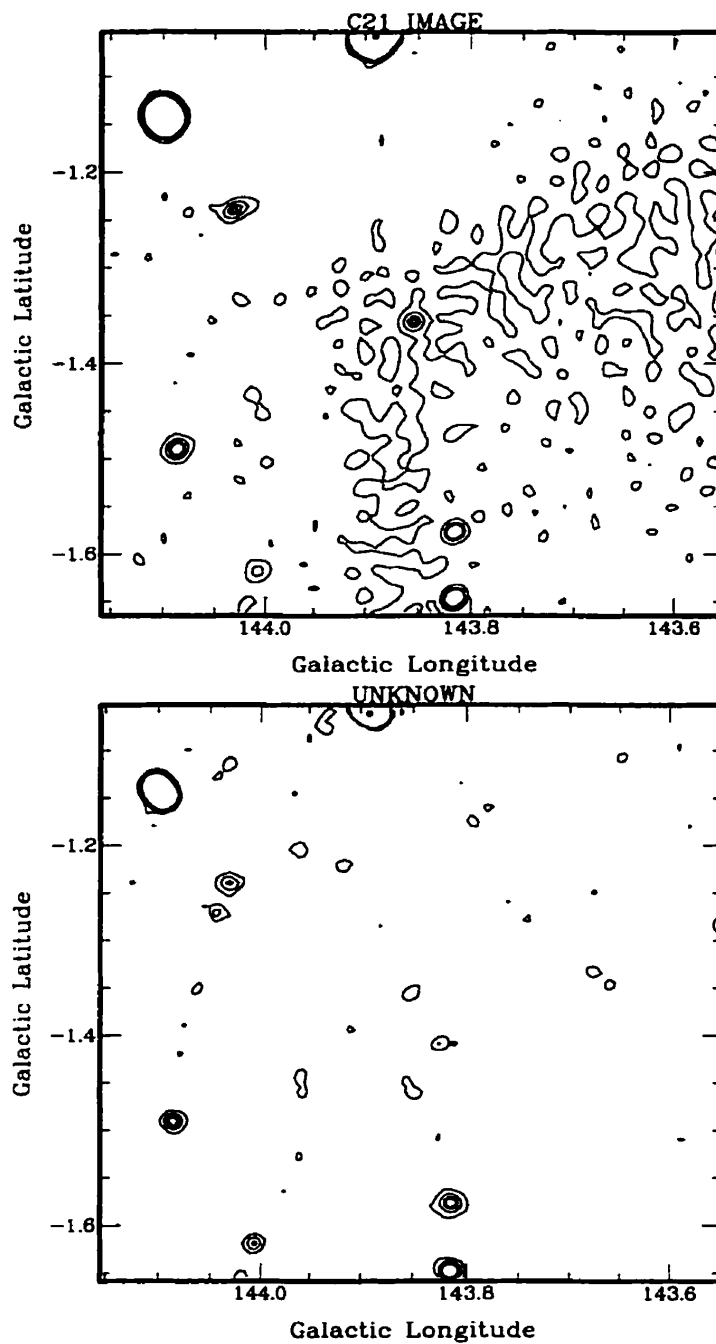


Figure 5.10: Comparison of the CGPS (top) and NVSS (bottom) contour plots for source 10. The base contour for the CGPS is 5.5K, while the base for the NVSS is 0.5K, the contour interval is 0.8K. Background noise visible in top image.

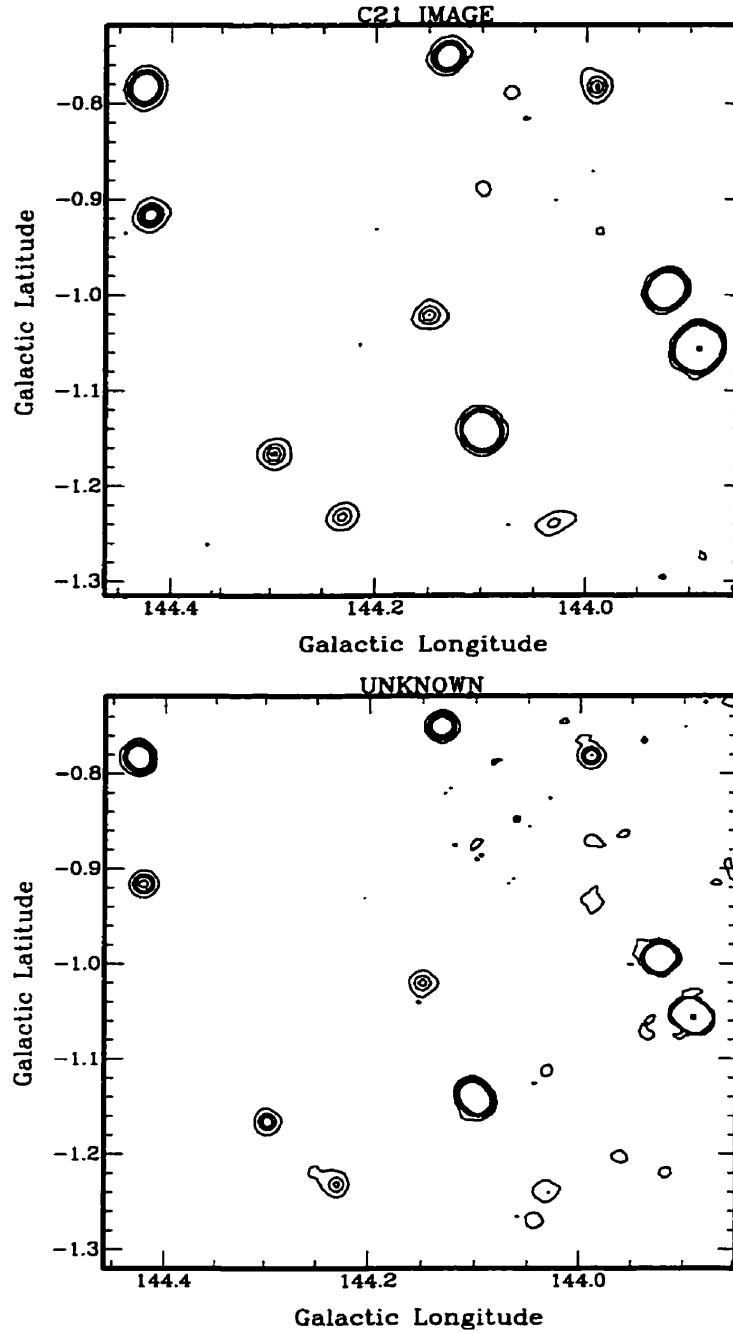


Figure 5.11: Comparison of the CGPS (top) and NVSS (bottom) contour plots for source 11. The base contour for the CGPS is 5.6K, while the base for the NVSS is 0.6K, the contour interval is 2K.

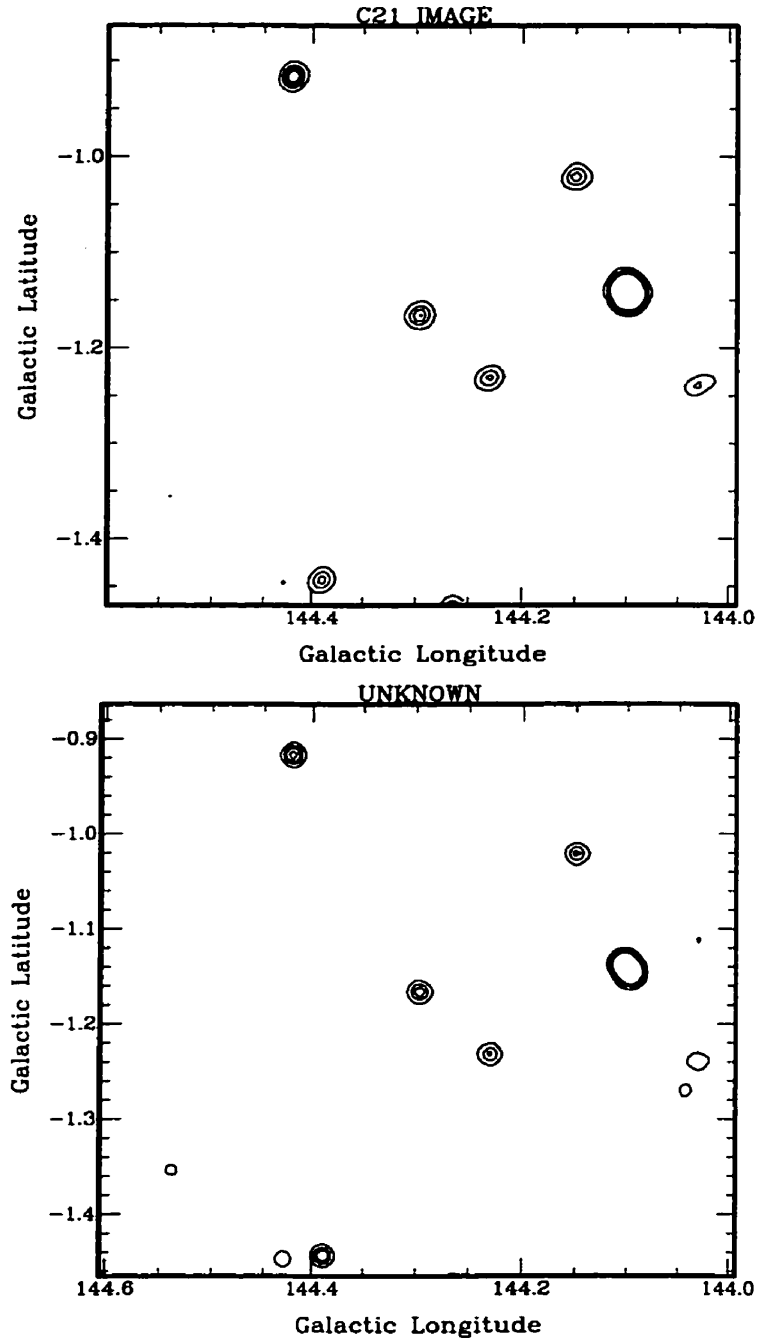


Figure 5.12: Comparison of the CGPS (top) and NVSS (bottom) contour plots for source 12. The base contour for the CGPS is 6K, while the base for the NVSS is 1K, the contour interval is 2K.

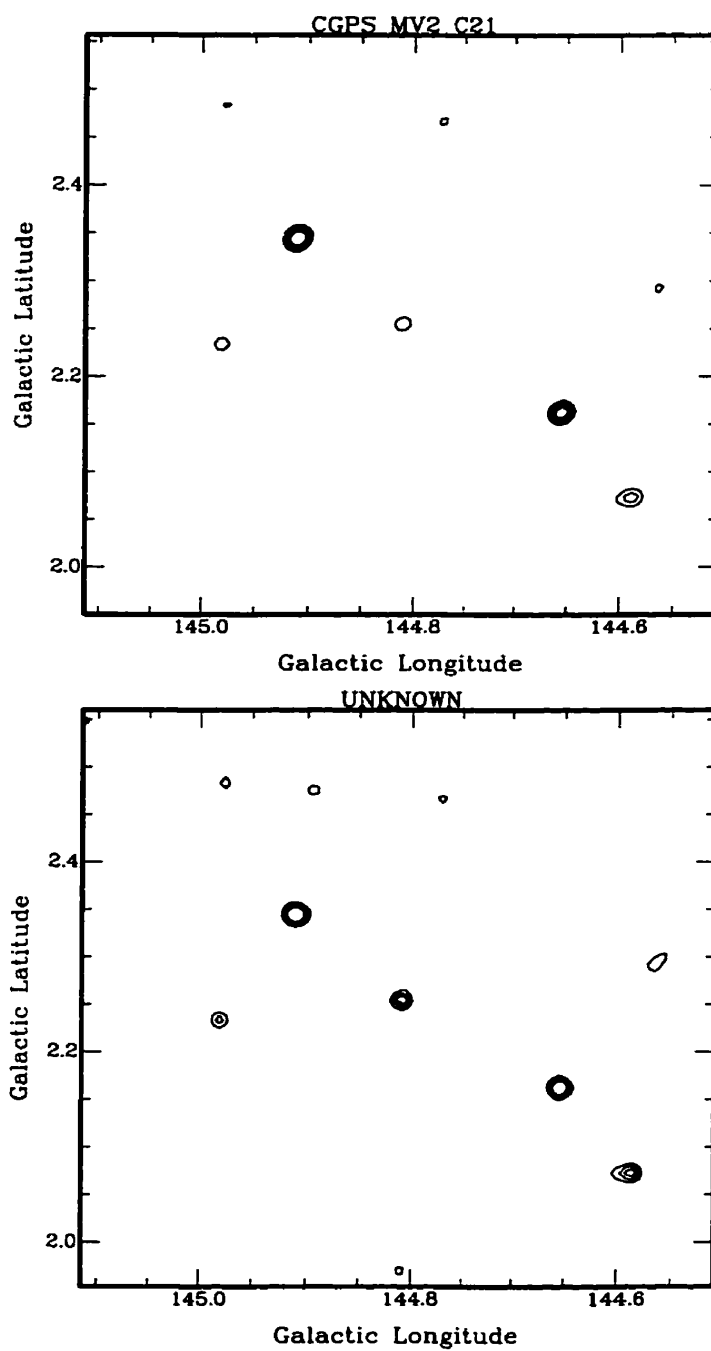


Figure 5.13: Comparison of the CGPS (top) and NVSS (bottom) contour plots for source 13. The base contour for the CGPS is 6K, while the base for the NVSS is 1K, the contour interval is 1K.

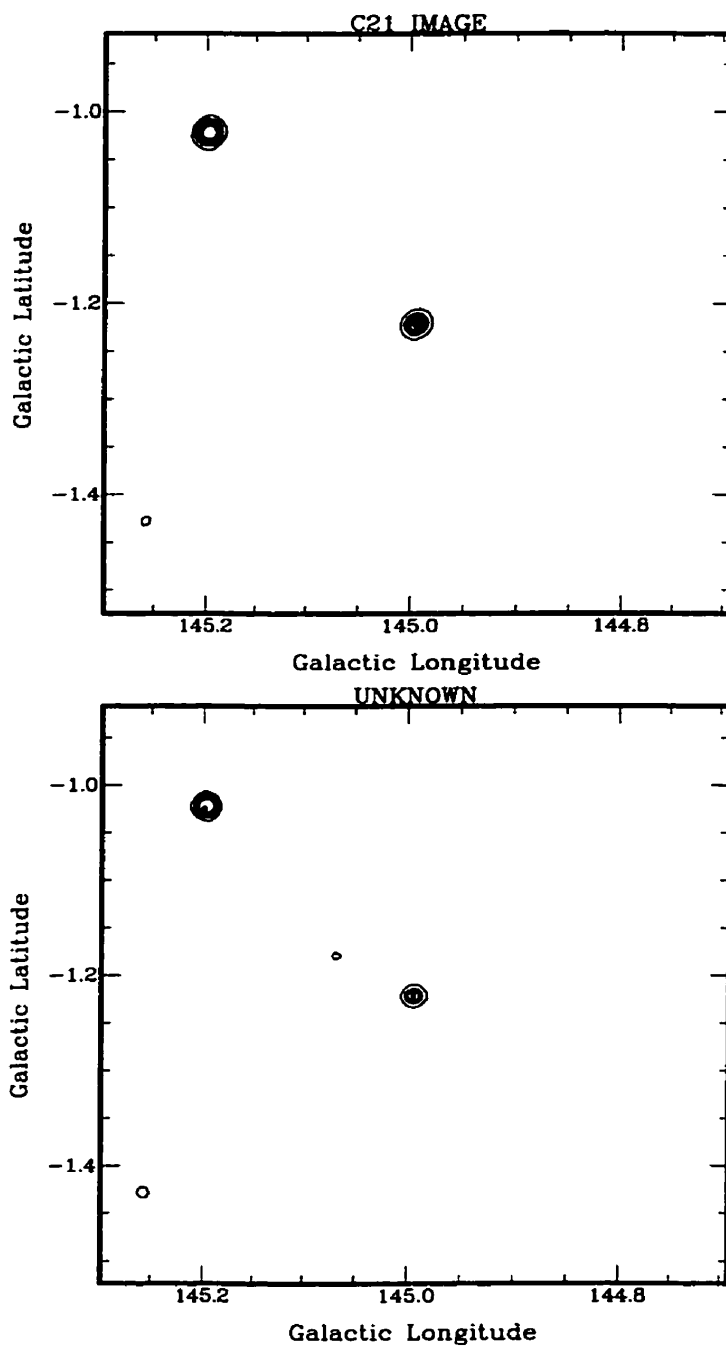


Figure 5.14: Comparison of the CGPS (top) and NVSS (bottom) contour plots for source 14. The base contour for the CGPS is 10K, while the base for the NVSS is 5K, the contour interval is 10K.

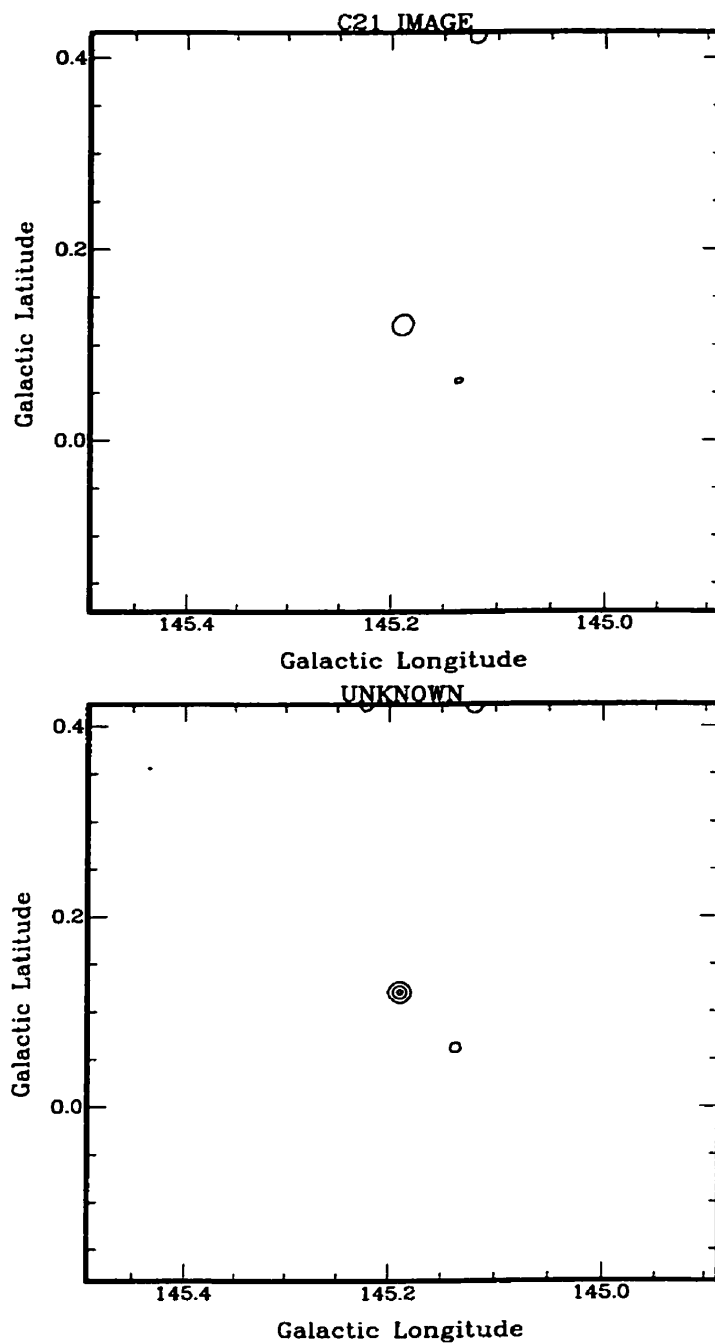


Figure 5.15: Comparison of the CGPS (top) and NVSS (bottom) contour plots for source 15. The base contour for the CGPS is 10K, while the base for the NVSS is 5K, the contour interval is 10K.

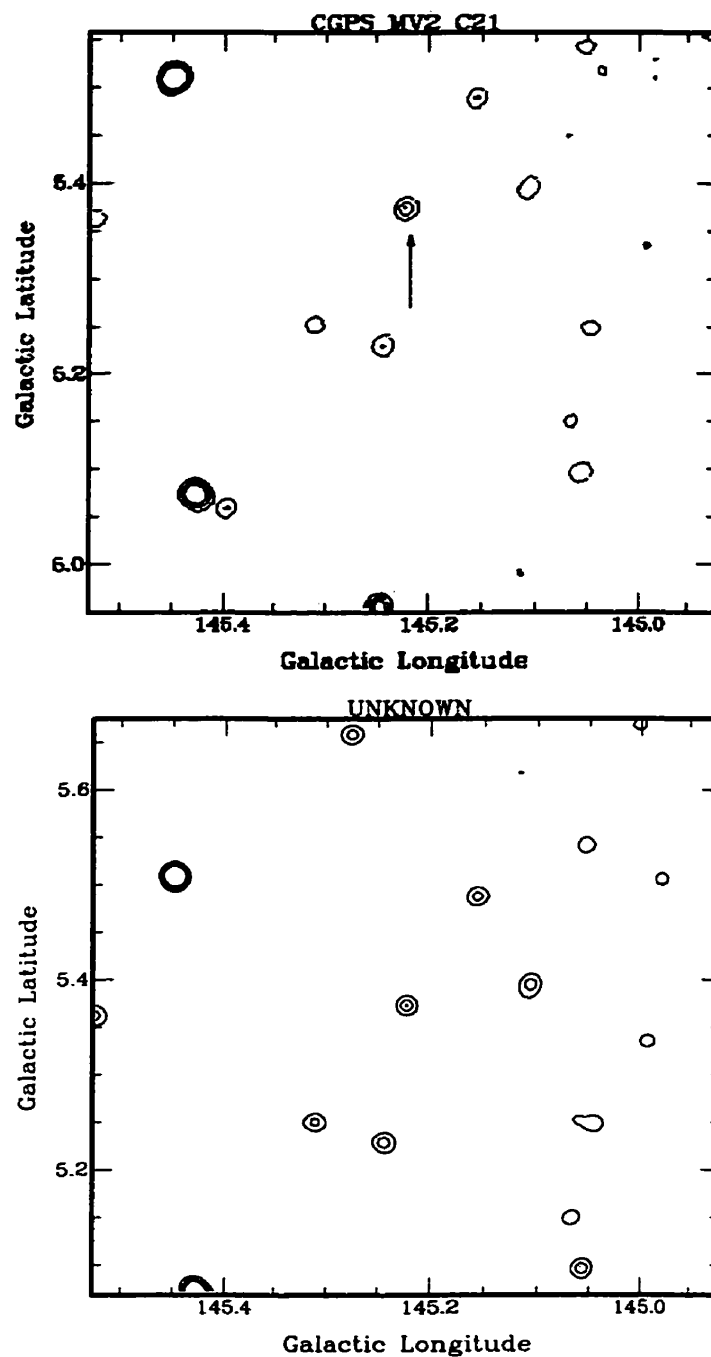


Figure 5.16: Comparison of the CGPS (top) and NVSS (bottom) contour plots for source 16. The base contour for the CGPS is 5.5K, while the base for the NVSS is 0.5K, the contour interval is 2K.

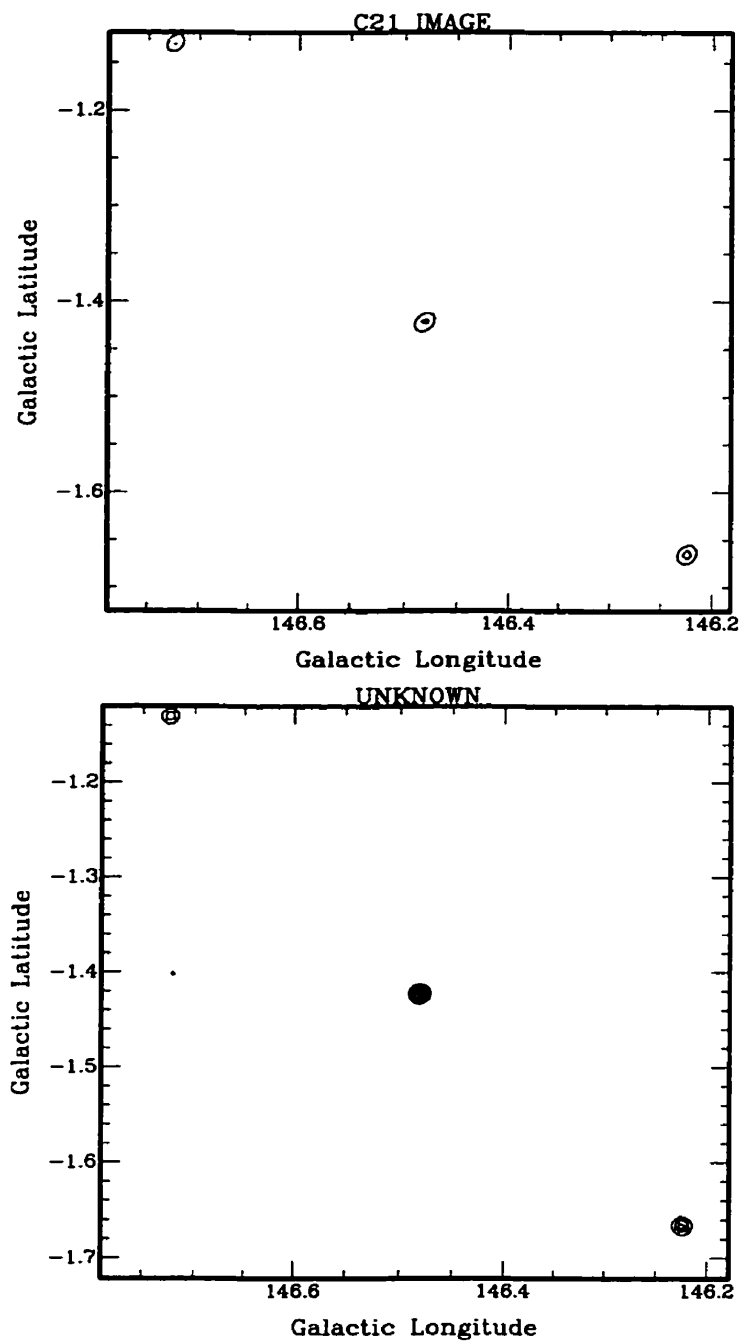


Figure 5.17: Comparison of the CGPS (top) and NVSS (bottom) contour plots for source 17. The base contour for the CGPS is 10K, while the base for the NVSS is 5K, the contour interval is 5K.

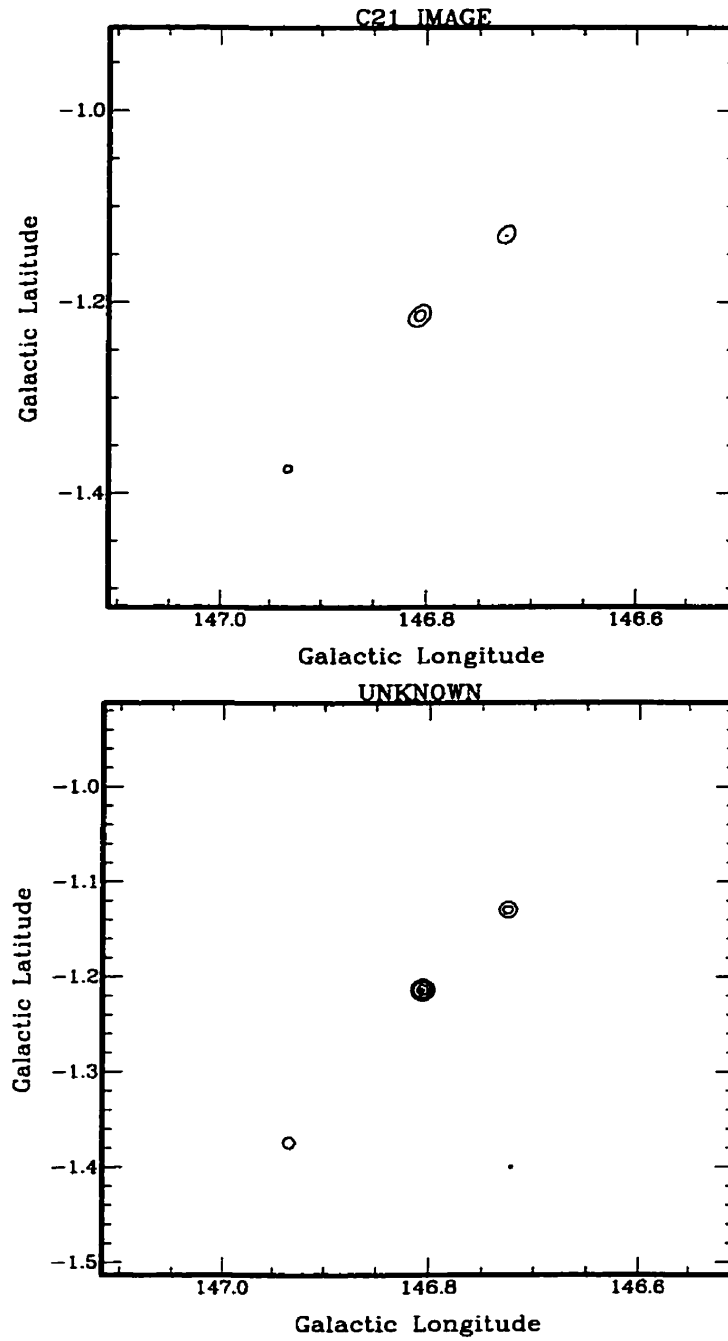


Figure 5.18: Comparison of the CGPS (top) and NVSS (bottom) contour plots for source 18. The base contour for the CGPS is 10K, while the base for the NVSS is 5K, the contour interval is 5K.

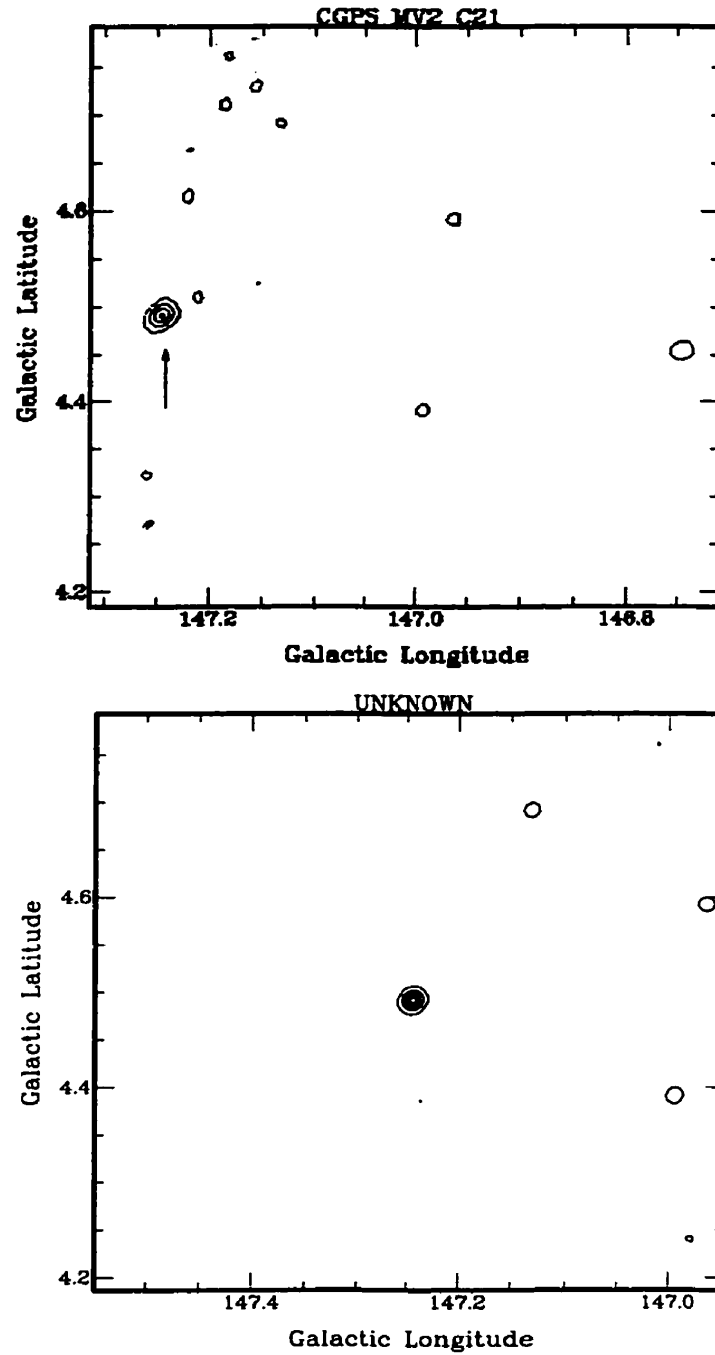


Figure 5.19: Comparison of the CGPS (top) and NVSS (bottom) contour plots for source 19. The base contour for the CGPS is 6K, while the base for the NVSS is 1K, the contour interval is 5K.

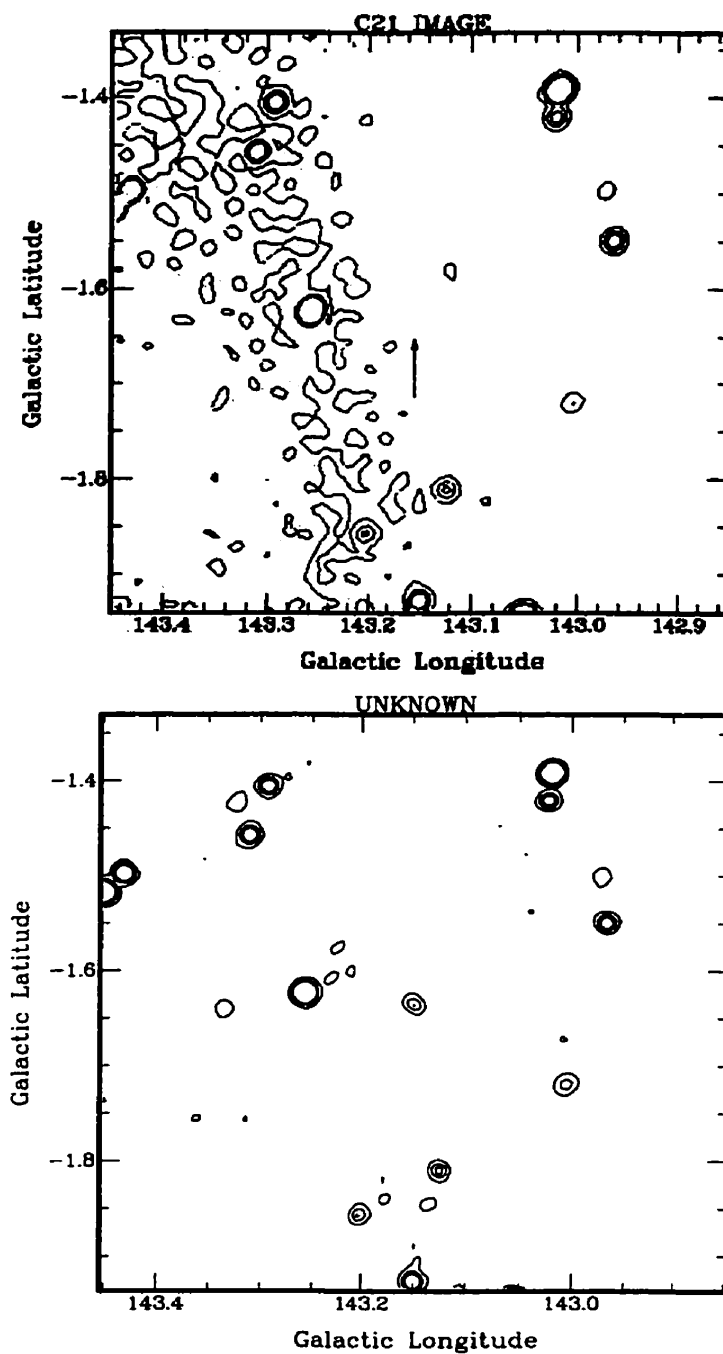


Figure 5.20: Comparison of the CGPS (top) and NVSS (bottom) contour plots for the unmatched source 1. The base contour for the CGPS is 5.5K, while the base for the NVSS is 0.5K, the contour interval is 1K. Background noise visible in top image.

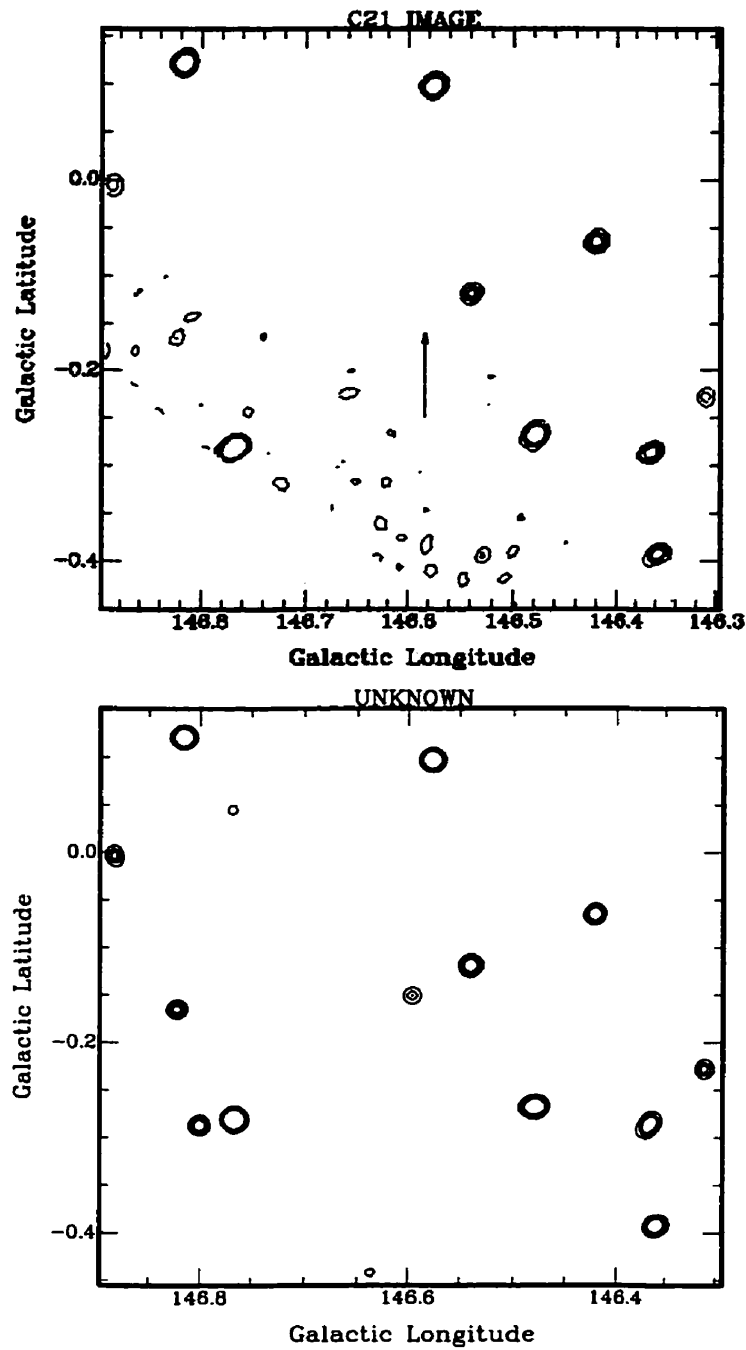


Figure 5.21: Comparison of the CGPS (top) and NVSS (bottom) contour plots for the unmatched source 2. The base contour for the CGPS is 6K, while the base for the NVSS is 1K, the contour interval is 1K. Mosaic edge visible in top image.

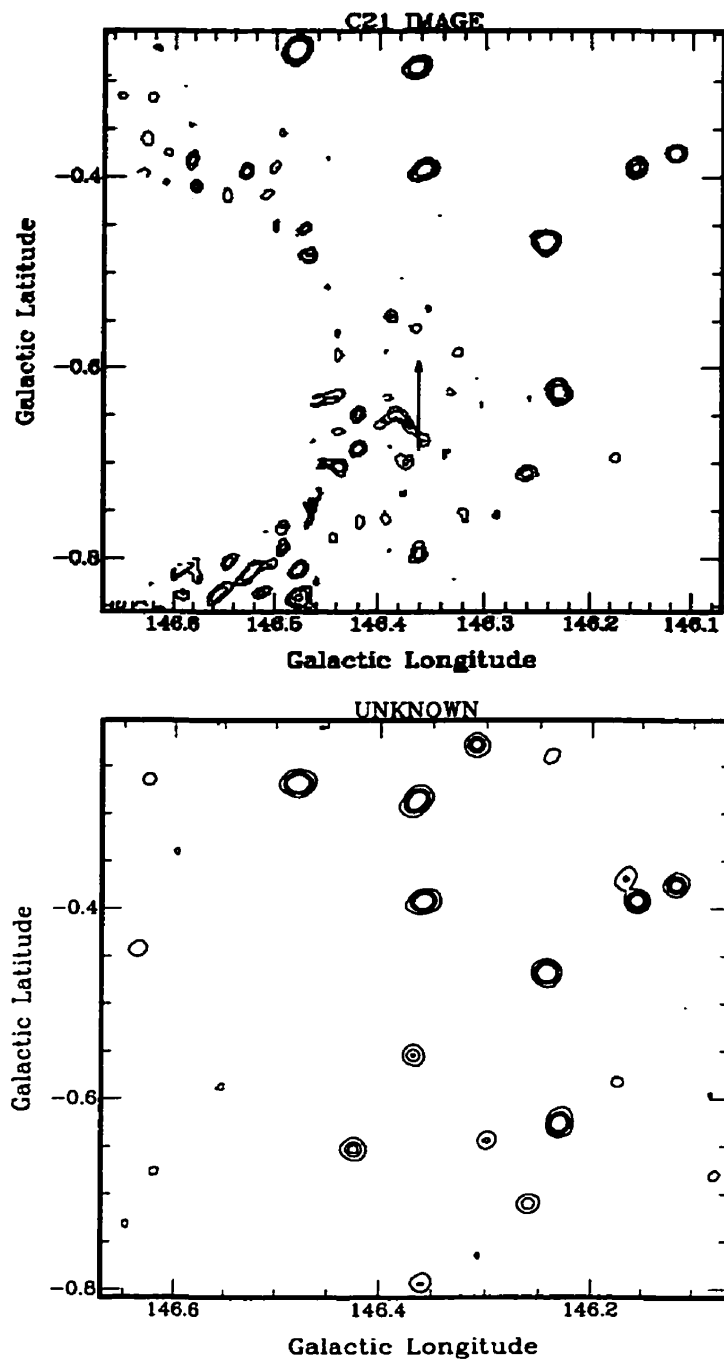


Figure 5.22: Comparison of the CGPS (top) and NVSS (bottom) contour plots for the unmatched source 3. The base contour for the CGPS is 5.5K, while the base for the NVSS is 0.5K, the contour interval is 1K. Mosaic edge visible in top image.

5.3 Comparison to the GB Variable Survey

A comparison with Bill Scott's PhD thesis (Scott 1996) was used to determine if there were any of the variable sources that coincided with previously known variable sources. Scott's thesis looks at the variability at centimetre wavelengths (6 cm). The search was done using the Greenbank 91m transit radio telescope between the years of 1986 and 1987. Variability information was obtained for both short term (on the timescale of one month) and long term (on a one year timescale). Ten of the CGPS variables were detected in the GB survey, of these there were three classified as variable by Scott. Sources 1 and 14 ($l = 139.1288, b = -2.7635$ and $l = 144.9954, b = -1.2207$ respectively) were found to have both short term and long term variability, while source 5 ($l = 142.4674, b = 3.3895$) was found to exhibit long term variability. The results are summarised in table 5.4. Table 5.4 indicates the source number, GB86 flux density with uncertainty, GB87 flux density with uncertainty, and the variable index as defined earlier. Only the confirmed variables from Scott's thesis appear as variables in this table. The CGPS variable sources that were not found in the Green Bank catalogues were all weak sources with flux density less than 41mJy. Therefore they were probably missed due to being below the sensitivity for variability in the GB survey.

5.4 Palomar Sky Survey

A search of the Palomar Sky Survey E plates (red) at the locations of the CGPS variables was performed to determine if any of the variables had optical counterparts. No bright sources were found to coincide. Faint optical counterparts are seen for

<i>Source number</i>	<i>GB86 flux mJy</i>	<i>GB87 flux mJy</i>	<i>V_I</i>
1	353±20	247±15	4.399
2	68±7	68±7	0.000
4	262±15	234±13	1.419
5	171±11	114±9	4.092
14	49±7	8±5	4.648
15	88±8	76±8	1.055
16	35±6	24±7	1.139
17	69±7	80±8	1.045
18	74±8	60±7	1.322
19	22±6	34±7	1.313

Table 5.4: Comparison of CGPS variables with GB86 and GB87 catalogue

source 8, source 13, source 14 and source 16. The Palomar survey images with radio source positions overlaid are given in the figures below. The position of the radio sources are indicated by the circles with radii of 10 arcseconds, which is much larger than the uncertainties on the radio position, typically less than 1".

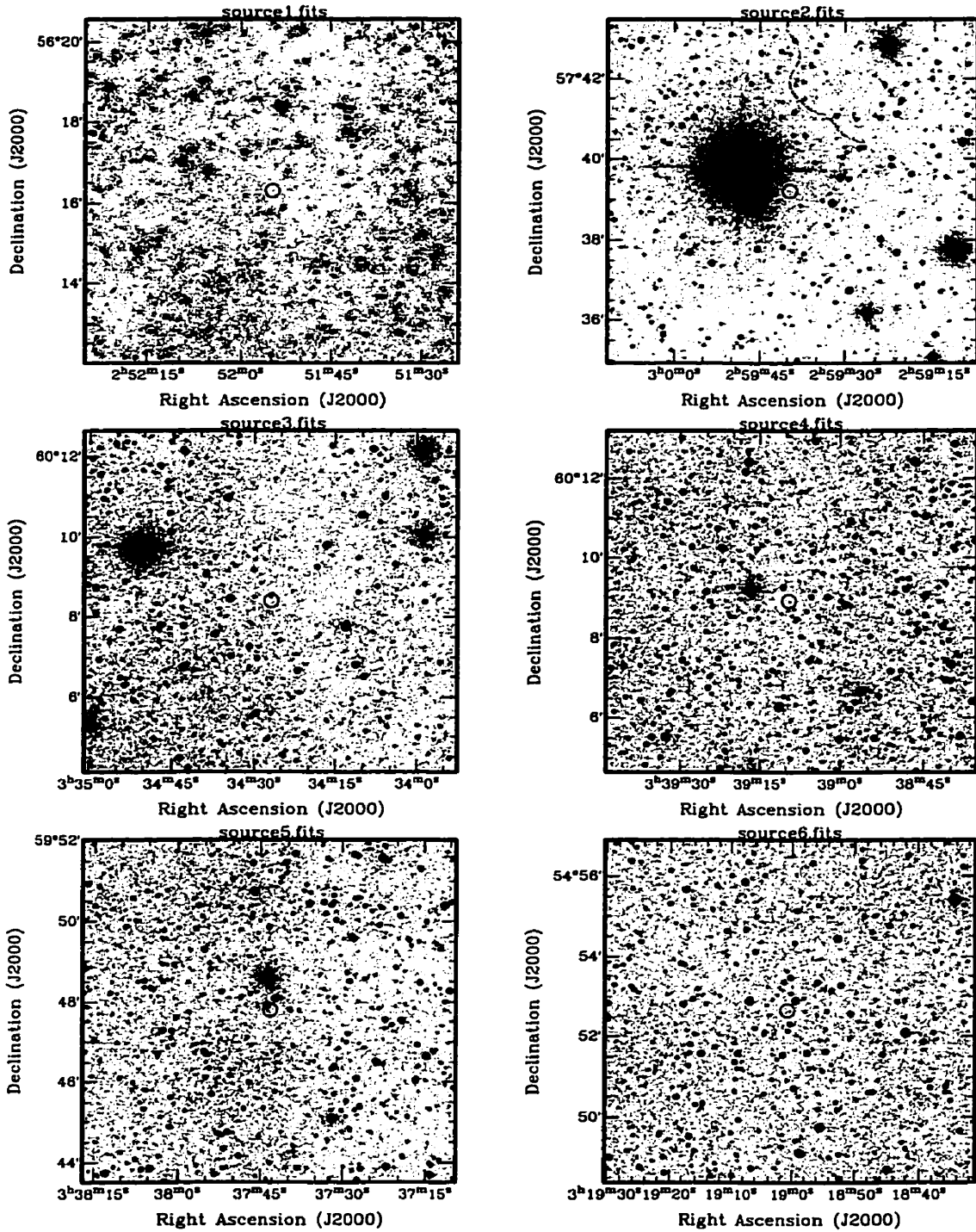


Figure 5.23: Comparison of the Palomar Sky Survey and the CGPS variables

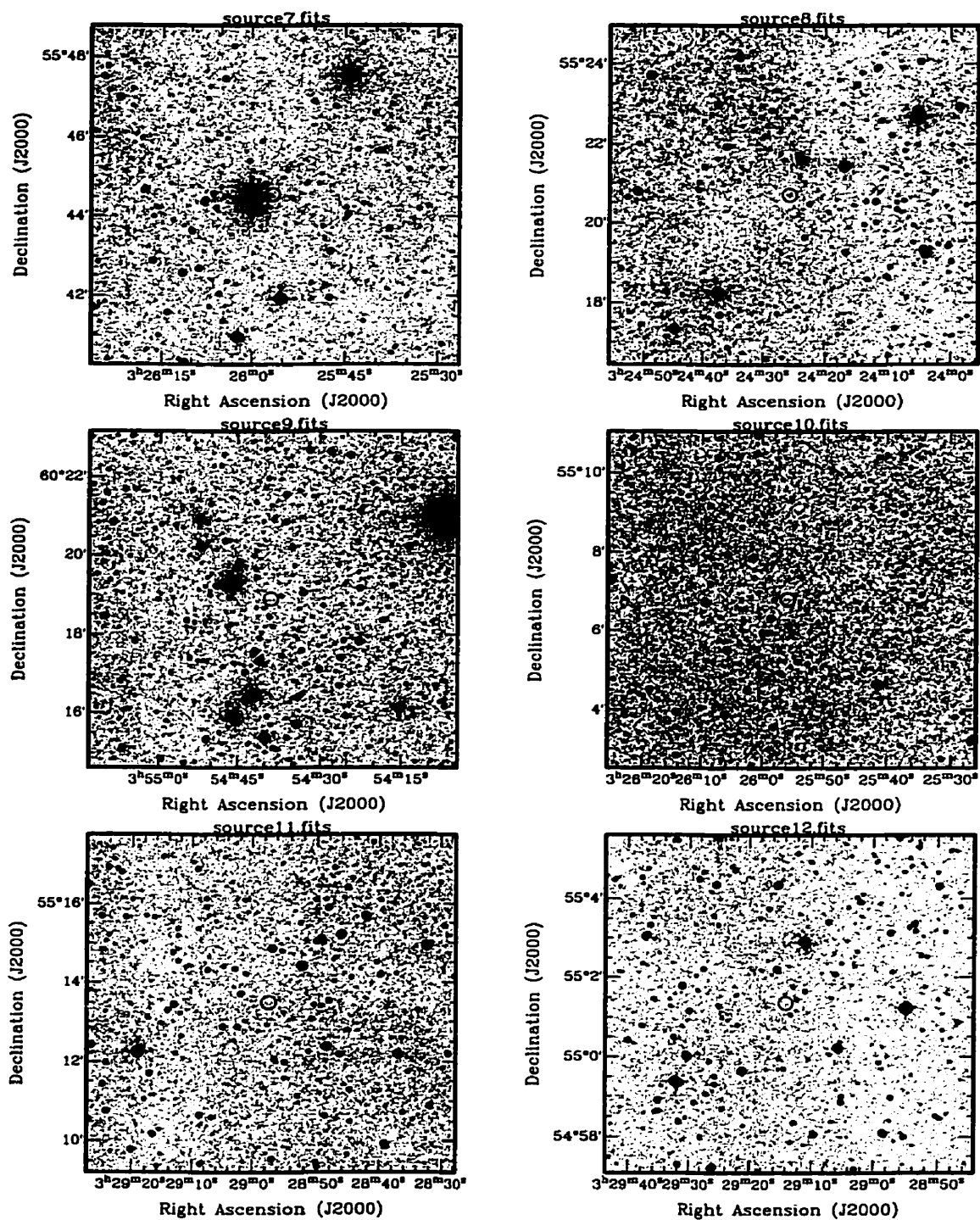


Figure 5.24: Comparison of the Palomar Sky Survey and the CGPS variables

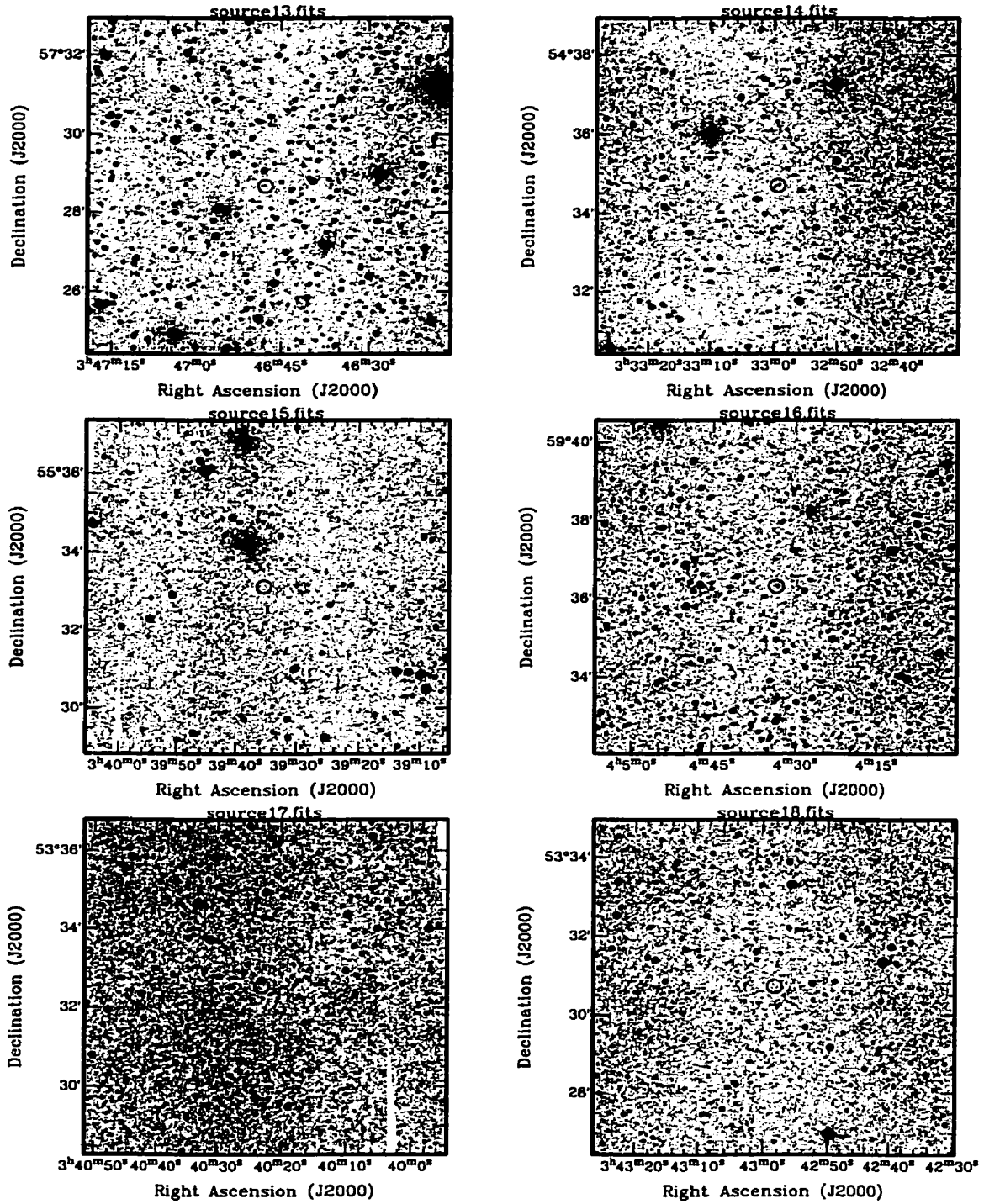


Figure 5.25: Comparison of the Palomar Sky Survey and the CGPS variables

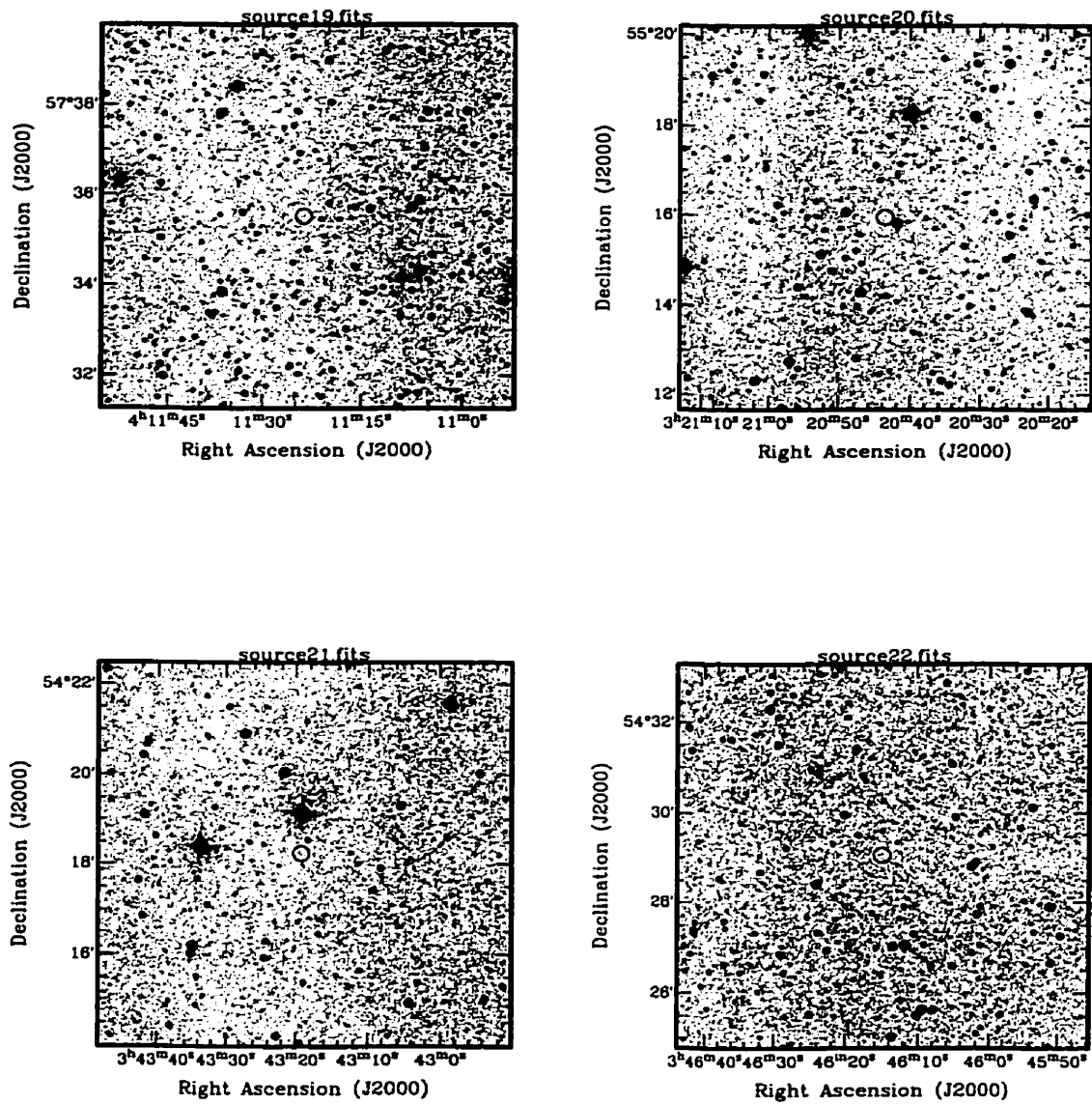


Figure 5.26: Comparison of the Palomar Sky Survey and the CGPS variables

Chapter 6

Conclusions and Future Study

6.1 Conclusions

The Canadian Galactic Plane Survey began in April 1995. Over the last five years observations have been taken at the Dominion Radio Astrophysical Observatory in Penticton B.C. Observations were also taken at the Effelsburg Observatory in Bonn, Germany to add short spacing information to the survey. The CGPS is a large scale survey of the northern galactic plane. The entirety of the project spans 70 degrees in galactic longitude and 9 degrees in galactic latitude at 1420 MHz. This frequency allows the study of both thermal and non-thermal sources, with resolution of 1 arcmin and sensitivity down to 0.2 mJy. The CGPS allows the scientific study of compact sources, polarisation, and diffuse radio emission. The focus of this thesis was to study the variability of compact sources at 1420 MHz, in a small region of the CGPS. This variability search is an order of magnitude deeper than any previous survey for variable radio sources in the galactic plane.

Compact sources at radio frequencies can be either galactic or extragalactic. Chris Butenhoff's work on the pilot project suggested that approximately 20% of the compact sources would be galactic. These sources would be primarily HII regions, planetary nebulae or supernova remnants. There are also stellar objects that radiate at radio frequencies; these are flare stars, novae, pulsars or X-Ray emitting binary stars. Of these objects, pulsars, novae and most types of radio stars are variables.

The other 80% of compact objects are extragalactic: radio galaxies, Seyfert galaxies, quasars or other active galactic nuclei.

The major purpose of this thesis was to search for compact variable sources at 1420 MHz. This search was done by comparing the CGPS and NVSS surveys, and is discussed in chapter 4 and 5. There were 5498 sources found in the CGPS catalogue, from the MV1, MV2, MW1 and MW2 mosaics, with signal-to-noise ratio greater than 5.0. 4968 sources were found in the NVSS catalogue. This difference arises because the sensitivity of the CGPS is slightly better than the NVSS. From these two catalogues 3837 sources were matched – with 19 of these being variable. This is a 0.5% rate of variability. An additional three variables were found in examining the unmatched sources. This low percentage could be a result of neglecting the close doubles and extended sources. Also, past variable surveys have not been as sensitive as the CGPS. The percentage of variability was found to be higher for stronger sources. A table of the percentage of variability as a function of flux density was given in chapter 5. The Westerbork variable search (327 MHz) found less than 1% variability with the weakest source being 6mJy. Radio Patrol (5 GHz) found 2.5% with the weakest sources being 16mJy. Although these variable studies are performed at different frequencies they do indicate an increase in the percentage of variables found with an increase in minimum flux density.

Another aspect of this thesis was the testing and improving of the programs FINDSRC and FLUXFIT, written at the DRAO. The pilot project found four problems with these programs. Testing of the software using GAUSSMAP found an additional three problems, as well as some misinterpreted parameters. Major changes to the program FLUXFIT regarding the underestimate of angular size, close dou-

ble sources and the overestimate of small sources were made. The underestimate of angular size resulted from a bug that was previously undetected, causing single sources to be badly fit. Also there was the problem with base-levels, in that large bright sources were not being fit completely and large residuals were left. After the base-level determination was reduced from 3% to 2% this problem was resolved. Close double sources were found to leave a distinct pattern after they had been subtracted. Knowing the existence of these sources allowed them to be removed manually before any further fitting was done. The overestimate of small sources was a result of nearby bright sources. The bright objects would also have to be removed manually first, thereby allowing for automatic removal of the small sources. A full discussion of these tests and changes is given in chapter 3. Although the changes to FINDSRC and FLUXFIT did improve the automated nature of compact source detection; this process is still not fully automated. Care must be taken in fitting and removing sources, and many sources still need to be removed manually. Other enhancements were made to the FLUXFIT program, including galactic coordinates and signal-to-noise ratio.

6.2 Future Study:

The production of the 1420 MHz variable list for the MVW mosaics is the first step in the analysis of these compact variable sources. Follow-up observations of the sources could allow for classification of their nature based on still unknown properties. As most of the previously unknown variables are weak radio emitters, a high sensitivity and high resolution follow-up study should be performed. Simultaneous observations

of multiple frequencies would allow for true spectral indices to be calculated. These spectral indices could be used for a classification of the sources' spectral properties, giving a better indication of their nature. A high resolution study could also give information about the individual source's morphology, provided that the source could be resolved. Time series studies of these variables could also be performed, this would give insight into the variability timescale and help to determine if any of these variables show short term as well as long term variability.

This thesis only considered the MVW mosaics of the CGPS. If the entire CGPS were examined for variability an estimated 45 000 compact sources would be found and about 225 of these would be variable, based on a 0.5% variability rate.

Another area for future study might be looking at the matched double sources or slightly extended sources that appeared as possible variables. These objects were not considered in this thesis as they can not be analysed by the same methods. It is important however, to determine whether or not these objects are variable, and to derive a method for determining their variability that can be used for the rest of the survey.

Bibliography

- Backer, D. C. 1988, in *Galactic and Extragalactic Radio Astronomy*, 2nd edn., ed. G. L. Verschuur & K. I. Kellermann (Springer-Verlag), 480
- Briggs, D. S., Schwab, F. R., & Sramek, R. A. 1999, in *Conference Series*, Vol. 180, *Synthesis Imaging in Radio Astronomy II*, ed. G. B. Taylor, C. L. Carilli, & R. A. Perley, Astronomical Society of the Pacific, 127
- Butenhoff, C. 1997, Master's thesis, University of Calgary, Calgary AB Canada
- Carroll, B. W. & Ostlie, D. A. 1996, *An Introduction to Modern Astrophysics*, 1st edn. (Addison and Wesley)
- Condon, J. J. & et al. 1998, *The Astronomical Journal*, 115, 1693
- Cornwell, T., Braun, R., & Briggs, D. S. 1999, in *Conference Series*, Vol. 180, *Synthesis Imaging in Radio Astronomy II*, ed. G. B. Taylor, C. L. Carilli, & R. A. Perley, Astronomical Society of the Pacific, 151
- Cornwell, T. & Fomalont, E. B. 1999, in *Conference Series*, Vol. 180, *Synthesis Imaging in Radio Astronomy II*, ed. G. B. Taylor, C. L. Carilli, & R. A. Perley, Astronomical Society of the Pacific, 187
- Coupinot, G., Hecquet, J., Auriere, M., & Futaully, R. 1992, *Astronomy and Astrophysics*, 259, 701
- Erickson, W. C. & Mahoney, M. J. 1985, *Astrophysical Letters*, 299, 29
- Gordon, M. A. 1988, in *Galactic and Extragalactic Radio Astronomy*, 2nd edn., ed. G. L. Verschuur & K. I. Kellermann (Springer-Verlag), 37
- Gregorini, L., Ficarra, A., & Padrielli, L. 1986, *Astronomy and Astrophysics*, 168, 25
- Gregory, P. C. & Taylor, A. R. 1986, *The Astronomical Journal*, 92, 371
- Habing, H. J. & Israel, F. P. 1979, *Ann. Rev. Astron. Astrophysics*, 17, 345
- Haslam, C. G. T. 1983, *The Observatory*, 103, 133
- Higgs, L. 1994, Man pages of CLEAN, DRAO
- . 1999a, Man pages of Findsrc, DRAO

- . 1999b, Man pages of Fluxfit, DRAO
- . 1999c, Man pages of Gaussmap, DRAO
- . 1999d, Private correspondance, DRAO
- Hjellming, R. M. 1988, in *Galactic and Extragalactic Radio Astronomy*, 2nd edn., ed. G. L. Verschuur & K. I. Kellermann (Springer-Verlag), 381
- Izvekova, V. A., Kuzmin, A. D., Shitov, V. M., & Yu, P. 1981, *Astrophysics and Space Science*, 78, 45
- Johnston, S. & Bailes, M. 1991, *Monthly Notices of the Royal Astronomical Society*, 252, 277
- Kellermann, K. I. & Owen, F. N. 1988, in *Galactic and Extragalactic Radio Astronomy*, 2nd edn., ed. G. L. Verschuur & K. I. Kellermann (Springer-Verlag), 563
- Kraus, J. D. 1986, *Radio Astronomy*, 2nd edn. (Cygnus Quasar Books), 1
- Osterbrock, D. E. 1989, *Astrophysics of Gaseous Nebulae and Active Galactic Nuclei* (University Science Books)
- Reich, P., Reich, W., & Frust, E. 1997, *Astronomy and Astrophysics Supplemental Series*, 126, 413
- Rengelink, R. B., Tang, Y., de Bruyn, A. G., Miley, G. K., Bremer, M. N., Rottgering, H. J. A., & Bremer, M. A. R. 1997, *Astronomy and Astrophysics Supplemental Series*, 124, 259
- Reynolds, S. P. 1988, in *Galactic and Extragalactic Radio Astronomy*, 2nd edn., ed. G. L. Verschuur & K. I. Kellermann (Springer-Verlag), 439
- Reynolds, S. P. & Chevalier, R. A. 1984, *Astrophysical Journal Letters*, 281, 33
- Riley, J. M. & Green, D. A. 1998, *Mon. Not. R. Astron. Soc.*, 301, 203
- Rys, S. & Machalski, J. 1990a, *Astronomy and Astrophysics*, 236, 15
- . 1990b, *Astronomy and Astrophysics*, 236, 15
- Salter, C. J. & Brown, R. L. 1988, in *Galactic and Extragalactic Radio Astronomy*, 2nd edn., ed. G. Verschuur & K. Kellermann (Springer-Verlag), 8

- Scott, W. K. 1996, PhD thesis, University of British Columbia, Vancouver B.C. Canada
- Seaquest, E. R. & Taylor, A. R. 1990, *The Astrophysical Journal*, 349, 313
- Shu, F. H. 1991, *The Physics of Astrophysics Radiation*, Vol. one (Mill Valley Ca: University Science Books), 181
- Sieber, W. 1973, *Astronomy and Astrophysics*, 28, 237
- Taylor, A. R. 1999, in *Conference Series*, Vol. 168, *New Perspectives on the Interstellar Medium*, ed. A. R. Taylor, T. L. Landecker, & G. Joncas, *Astronomical Society of the Pacific*, 3
- Taylor, A. R., Goss, W. M., Coleman, P. H., van Leeuwen, J., & Wallace, B. J. 1996, *The Astrophysical Journal Supplemental Series*, 107, 239
- Thompson, A. R. 1999, in *Conference Series*, Vol. 180, *Synthesis Imaging in Radio Astronomy II*, ed. G. B. Taylor, C. L. Carilli, & R. A. Perley, *Astronomical Society of the Pacific*, 11
- Vessey, S. J. & Green, D. A. 1998, *Monthly Notices of the Royal Astronomical Society*, 294, 607
- Whiteoak, J. B. 1993, PhD thesis, University of Sydney, Sydney Australia
- Zeilik, M., Gregory, S. A., & Smith, E. V. 1992, *Introductory Astronomy and Astrophysics*, 3rd edn. (Saunders College Publishing)